Diagnosing Topological Quantum Matter via Entanglement Patterns

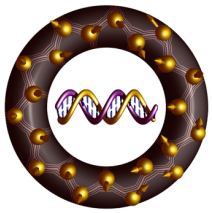

Konstantinos Meichanetzidis

School of Mathematics
School of Physics & Astronomy

UNIVERSITY OF LEEDS

Submitted in accordance with the requirements for the degree of

Doctor of Philosophy

August 2017

The work in Chapters 4,6 of the thesis has appeared in preprint as follows:
Free-fermion descriptions of parafermion chains and string-net models
Konstantinos Meichanetzidis, Christopher J. Turner, Ashk Farjami,
Zlatko Papić, Jiannis K. Pachos
arXiv:1705.09983
– I was responsible for numerically confirmation of analytical results and conjectures and arguments regarding Kitaev's model, as well as development of theory. Author Farjami was responsible for numerics of string-nets. Turner was responsible for analytics of parafermions and collaborated with Farjami on numerics off the fixed point. Farjami and Turner carried out the boundary sampling of string-nets. Papić and Pachos directed the work.

The work in Chapters 3,6 of the thesis has appeared in publication as follows:
Optimal free descriptions of many-body theories
Christopher J. Turner, Konstantinos Meichanetzidis,
Zlatko Papić, Jiannis K. Pachos
Nature Communications 8, 14926 (2017)
– I was responsible for numerics on matching to the free line and development of theory. Turner for implementation of optimisation and plotting the phase diagram, as well as development of theory. Papić and Pachos directed the work.

The work in Chapters 4,5 of the thesis has appeared in publication as follows:
Anatomy of Fermionic Entanglement and Criticality in Kitaev Spin Liquids
Konstantinos Meichanetzidis, Mauro Cirio, Jiannis K. Pachos, Ville Lahtinen
Phys. Rev. B 94, 115158 (2016)
– I was responsible for numerics and analytics on the entropy of chains and construction of effective models. Cirio was responsible for theoretical development and numerics of entropy of chains and study of critical chains. Lahtinen was responsible for identifying universality classes of the model's criticalities. Pachos and Lahtinen oversaw the project.

The work in Chapters 3,4,5 of the thesis has appeared in publication as follows:
Diagnosing Topological Edge States via Entanglement Monogamy
Konstantinos Meichanetzidis, Jens Eisert, Mauro Cirio,
Ville Lahtinen, Jiannis K. Pachos
Phys. Rev. Lett. 116, 130501 (2016)
– I was responsible for numerics and interpretation of the SSHH results. Eisert was responsible for monogamy relations. Lahtinen was responsible for development of theory. Pachos was responsible for theory and conduction of the work.

The work in Chapter 5 of the thesis has appeared in publication as follows:
Two-dimensional Chern semimetals on the Lieb lattice
Giandomenico Palumbo, Konstantinos Meichanetzidis
Phys. Rev. B 92, 235106 (2015)
– I was responsible for numerics and analytics regarding phase transitions. Palumbo was responsible for theoretical development.

For the indifferent Monad.

"Okay, well, sometimes science is more art than science, Morty.
A lot of people don't get that."
- Rick Sanchez

Acknowledgements

I begin by thanking Alex for his contagious excitement about maths, liberation of metaphorical slavery, and mainly, Yorkshire. It would be a sin to not acknowledge Giandomenico, with his monstrous knowledge of physics and handwaving-accompanied ideas, and for our collaboration. I also thank Ville, the honeycomb master, for being a mentor through our projects on Kitaev's model and not murdering me when I asked silly questions. It was a privilege to join forces with Mauro, bravely hammering through the pain of calculations under 80s-90s metal. I thank Ben, that's right, for radiating long-range workaholions during the day, and party-waves during the night. Speaking of speaking, I thank Stefanos for going a long way to support me on a range of aspects, from oogly to boogly, and for a healthy amount of scolding. For the most inventive bad jokes ever and for being a source of facts about cold-blooded creatures of the Mesozoic era, I thank Tim, Rob, and Adam. And football. And maybe quantum mechanics is wrong. I thank Paul for his sykness on personal and academic matters, the parties he did not organise, his interest in crazy ideas, and most importantly for giving me a cool nickname. It is crucial to also acknowledge Ashk Furtak and KP's contribution on redefining the sea-level for chill by keeping the complex phase at integer multiples of π and for keeping the wavelengths on the longer side. Very importantly, I would like to thank Chris for our collaboration on our freedom papers. His razor sharp mind and extensive knowledge is an inspiration and a pleasure to argue with. I also would like to acknowledge Markus for being authentic and enthusiastic about attacking difficult problems, such as protecting qubits from noise, hitting a ball with a

stick while riding a bike, and getting robots that are smarter than us to do what we tell them. I would like to thank Wootton for a one-line word of wisdom, and Sofyan for interesting and unconventional conversations. Furthermore, I am grateful to German for inspiring ideas regarding primes. Regarding, office life the Fourier weights that James can produce with his vocal box, always were interesting. Discussing topological phases was fun, wait what is a fermion, I dunno man. My acknowledgements extend as well to Felix and Ruben for their enthusiasm about deep but practically unimportant concepts. Finally, I am thankful for the hospitality of the research groups that I visited. I want to deeply thank Chris for being a great colleague, and an understanding and close friend. Our dialogues on almost the totality of everything are invaluable.

My regards to my PhD co-supervisor, Paul Martin, who had trust in me and distrust in the nature of reality, and provided non-trivial feedback. My appreciation extends to Zlatko Papic, who during our collaborations took the time to advise me academically, always with an indispensable drop of lemon. Furthermore, it was an honour to work with Jens Eisert, who always has a fresh take on things, on the monogamy project.

It goes without saying that I am grateful to Jiannis Pachos, my PhD supervisor. His intuition helped navigate the research landscape and his anarchic research method always lead to fruitful results. His further enthusiastic support regarding my academic career is highly appreciated. “When in doubt, be an expert”.

I would like to thank Akis, Lampros, Lne, Vicky, Alexis for being great friends, my brothers Alex and Filimon for picking on me, and my parents who encouraged me to pursue my interests. Finally, I am greatful for Leeds’ music scene, the galleries of London, the Aegean sea, and the existence of good ice cream in the universe.

Abstract

Quantum matter involves the study of entanglement patterns in the ground states of many-body systems. Of significant interest have recently been topological states of matter, which exhibit characteristics only described globally. As such they are robust to local deformations. In this thesis, we study inter-correlations of many-body states through the entanglement spectrum, obtained by a bipartition of both topological and non-topological systems.

In particular, we introduce two novel diagnostics which operate on entanglement spectra. For topological phases supporting edge states on open boundaries we take a quantum-information inspired approach by invoking the monogamy relations obeyed by multi-partite systems. Within a strictly single-particle framework, we establish a correspondence between highly entangled mode and the existence of edge states. In the many-body context, we introduce the interaction distance of a mixed state. Exclusively via the entanglement spectrum it determines how close a free-fermion state lies and what the emergent free quasiparticles are.

We apply these two measures to diagnose the properties of a variety of free and interacting fermionic topological systems and reinterpret their properties from a fresh point of view. Our case studies revolve around Kitaev's honeycomb model, which supports both short-range and long-range topological order, constituting it thus relevant to both the monogamy qualifier and the interaction distance. The possibility to diagnose whether a model has zero interacting distance or if it supports maximally entangled states provides central and compact information about the behaviour of complex quantum systems.

Contents

Chapter 1

Introduction

1.1 In Search of Structure

A most challenging aspect of theoretical physics is the understanding of emergence. One can argue that all interesting phenomena are emergent. Even when a simple description of a macroscopic system is possible, it is in terms of effective objects whose complexity we completely disregard. On the other hand, when a microscopic system allows for a low-complexity description, its properties become trivial. There is however a sweet-spot where objects are regarded as elementary but are allowed to interact and thus non-trivial collective behaviour arises.

A natural setting to study emergent phenomena is condensed matter physics, where materials exhibiting various phases emerge out of interactions between quantum particles. Modern condensed matter physics entails the study of the structure of entanglement in many-body systems. Entanglement properties allow classification as well as possess powerful diagnostic value. In general, zero temperature phases and transitions between them are characterised by qualitative differences of local correlation patterns.

In this thesis, we focus on topological states of matter. In the simplest manner they can be described as states which cannot be identified by any local quantity, and global order parameters instead need to be defined to map out their phase diagrams. As they are realised by microscopic interacting particles, but nevertheless can only be characterised non-locally, they are a profound example of emergence. Their properties are imprinted in their entanglement patterns. Throughout the

thesis we construct diagnostic tools, such as the *monogamy qualifier* and the *interaction distance*. Their purpose is to extract signatures of topological properties from the study of the correlation structure of many-body quantum states.

1.2 Structure of Thesis

In Chapter 2 we establish the theory behind correlations in fermionic many-body systems. From these correlations we define the topological invariants that characterise topological states of matter. Chapter 3 contains novel diagnostics of quantum correlations that were established during this PhD, namely the monogamy qualifier and the interaction distance.

In Chapter 4 we study Kitaev's honeycomb model and fully study its entanglements properties. This model has been thoroughly studied in the literature. We use this model as our exemplar on which we apply the tools we have introduced in Chapters 2 and 3 and show consistency with existing understanding. Since this model is exactly solvable in its symmetry sectors, we can obtain analytical results in certain cases. Using the monogamy qualifier, we also connect properties of certain symmetry sectors to those of Kitaev's wire. Insight attained from Kitaev's model is usually transferable to other models.

Branching out from the Kitaev model we delve into other models that are connected to it in some way and study their entanglement properties. The connections to other models are shown in Fig.1.1. In Chapter 5 we study free fermion models using the diagnostic of monogamy as it manifests in their covariance matrices. In particular we study Haldane's Chern insulator and the Su-Schrieffer-Heeger model. We find that properties of the latter are reflected in the former. We also introduce a new free fermion model, the Duffin-Kemmer-Petiau Chern semimetal, inspired by Haldane's Chern insulator.

In Chapter 6 we analyse interacting fermionic models. We extract the monogamy signature corresponding to edge states in the Su-Schrieffer-Heeger model using the monogamy qualifier. We then use the interaction distance on the transverse field Ising model with longitudinal field, parafermion chains, as well as string-nets, and in the process we obtain surprising results.

Throughout the thesis, we introduce only concepts necessary for our purposes.

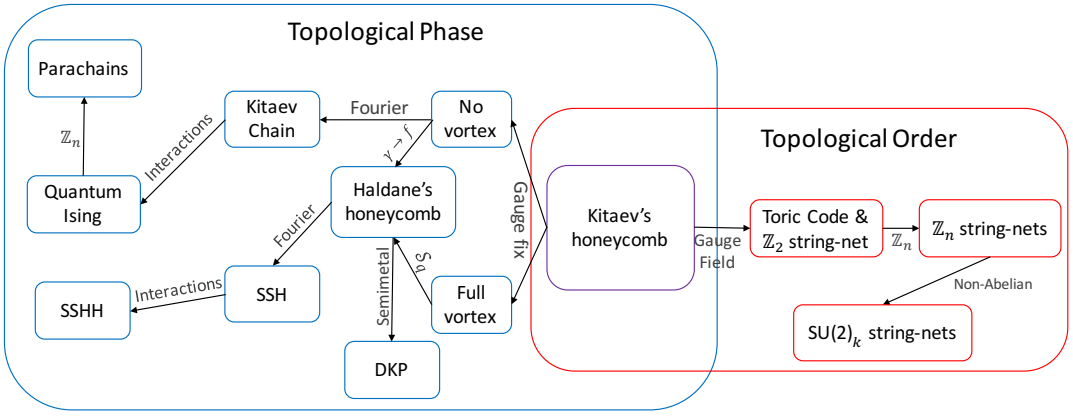

Figure 1.1: Relations between models studied in this thesis with Kitaev's model as common ground. The blue box contains short-range entangled topological phases and the red box long-range. Kitaev's honeycomb in the purple box hosts both short- and long-range topological order. Throughout the thesis we make explicit the relations we establish between these models. The labels on the arrows representing the relations become apparent in the context of each Chapter.

Chapter 2

Correlations and Topological Quantum Matter

2.1 Introduction

As this thesis is mainly concerned with correlations in ground states of topological quantum matter, it is useful to clarify our language. For the purposes of this work, we use Kitaev's definition of *topological order* [1] and reserve the term *topological phase* to define a state characterised by a non-vanishing topological invariant which is robust under adiabatic deformations of the Hamiltonian. According to this convention, a system with no boundaries is topologically ordered when its ground state degeneracy depends on the genus of the surface it is defined on. Topological phases, on the other hand, have a unique ground state on any closed surface.

2.2 Topological Phases

For a major part of this thesis we are concerned with topological phases that can be realised by *free* fermionic lattice models. The ground state of such systems is unique for periodic boundary conditions. We call a free-fermion Hamiltonian, H, on a lattice or more generally graph Λ, one that is quadratic in fermion operators

$$\{f_i, f_j\} = 0, \text{ with } \{f_i^\dagger, f_j\} = \delta_{ij}, \text{ for } i, j \in \Lambda_\mathrm{v}, \tag{2.1}$$

where Λ_v is the set of vertices or sites of the lattice. The fermions are allowed to tunnel between sites, reflected by the quadratic "hopping" terms $h_{ij} f_i^\dagger f_j + \text{h.c.}$ in H, as well as to feel a background potential landscape modelled as an on-site energy cost, or "chemical potential", $h_{ii} f_i^\dagger f_i$. The hoppings can be thought of as decorations of the links of the graph $(i, j) \in \Lambda_l$, and the chemical potentials can be viewed as weights on the vertices. Finally, if the hoppings are complex, then the graph becomes a directed graph where the direction of the link flips when the time reversal operator acts. In general we represent such Hamiltonians as

$$H = f^\dagger h f, \tag{2.2}$$

where f is a column vector containing the fermionic operators and the $|\Lambda_v| \times |\Lambda_v|$ matrix h contains the hoppings and chemical potentials. Note that the number of fermions in the system, F, is a good quantum number since hoppings and chemical potentials commute with the population operator $F = \sum_i n_i$ with $n_i = f_i^\dagger f_i$.

The model is solved when h is diagonalised,

$$h = V^\dagger E V, \tag{2.3}$$

where now E is diagonal with the energies ε_i of the normal modes, $c = fV$, whose amplitudes occupy the columns of matrix V. The energy of the ground state is $E_\mathrm{gs} = \sum_{i=1}^{F} \varepsilon_i$ and is realised by occupying the F smallest energy states, $c_1^\dagger \dots c_F^\dagger |0\rangle$, where we have ordered the energies as $\varepsilon_i \leq \varepsilon_j$ for $i < j$. Any other many-body state then is represented by different occupation patterns $\{n_i\}$ of the normal modes as $\otimes_{i=1}^{F} c_i^{\dagger n_i} |0\rangle$. The wave function in real space is simply the Slater determinant of the populated eigenmodes.

In case the Hamiltonian also contains pairing terms $f_i f_j + \text{h.c.}$, we can write it in the Majorana basis by splitting the fermions into their real and imaginary parts as

$$f_i = \frac{1}{2}(\gamma_{2i-1} + i\gamma_{2i}), \text{ with } \gamma_i^\dagger = \gamma_i \text{ and } \{\gamma_i, \gamma_j\} = 2\delta_{ij} \tag{2.4}$$

This can also be done when there are no pairings, but it is redundant. Now the Hamiltonian is written as

$$H = \gamma h \gamma, \text{ where } h = iA, \tag{2.5}$$

with A real and anti-symmetric so that the $2|\Lambda_v|$-dimensional matrix h is hermitian. Diagonalising the hopping-pairing (or Majorana hopping) matrix h we have

$$h = U^\dagger D U, \tag{2.6}$$

where the diagonal matrix D contains pairs of energies $\pm\varepsilon_i$ with their corresponding eigenvectors being conjugate pairs of each other and occupying columns of U. This means we can think of the system as decoupled two-level systems, and the ground state is obtained when *all* of them are de-excited and has energy $E_{\text{gs}} = -\sum_{i=1}^{|\Lambda_v|} \varepsilon_i$. We can arbitrarily call this state the vacuum $|0\rangle$ and excited states are realised by exciting these two-level systems in particular patterns.

Since h grows polynomially with $|\Lambda_v|$, then it is efficient to perform the diagonalisation in (2.3) and (2.6). In this sense, free fermions (or free Majoranas) are said to be efficiently simulatable on a classical computer, as diagonalisation cost of a $N \times N$ matrix scales as $\mathcal{O}(N^3)$ in the worst case. Throughout this thesis, all free-fermion systems are solved in real-space by numerically diagonalising their h-matrices. Note, that even though this procedure is exact, we shall restrain from referring to it as 'exact diagonalisation', since this name is reserved for the method of building and diagonalising the Hamiltonian matrix in the full Hilbert space of the problem, for example in the $2^{|\Lambda_v|}$-big Fock Space for fermions or the $d^{|\Lambda_v|}$ for d-level spins. We would resort to exact diagonalisation in the case of a generic fermionic Hamiltonian which includes non-quadratic terms in the fermionic operators. A common physical example of this would be density-density interaction terms of the form $\sum_{i<j} U_{ij} n_i n_j$.

Translation Symmetry

In case Λ is a d-dimensional lattice decomposable into unit-cells which contain an N number of sites, it preserves translation invariance along the lattice directions

and thus momentum is conserved. As would be the case for any other symmetry, the hopping matrix can be block-diagonalised into sectors labelled by the symmetry's eigenvalues, which in this case are the lattice momenta along the d directions, $h = \oplus_p h(p)$. We can then Fourier transform the operators $a = f, \gamma$ as $a_r = \sum_p e^{-ipr} a_p$, with r being d-dimensional vector labelling the unit-cells and $p \in [0, 2\pi)^{\times d}$ the lattice momentum in the d-dimensional Brillouin zone. Then the Hamiltonian can be written as

$$H = \sum_p H(p) \ , \quad H(p) = a^\dagger h(p) a, \tag{2.7}$$

where $a^\dagger = (a_1^\dagger \ a_2^\dagger \ \dots \ a_N^\dagger)$. The band structure of the model can then be extracted from $h(p)$, whose N-many eigenvalues $E_n(p)$ are functions of momentum and play the role of the energy bands with Bloch vectors $|n(p)\rangle$.

2.2.1 Topological Invariants

Now we define the topological invariants that are used in this thesis, namely the winding number w for 1D systems composed of 2-site unit cells and the Chern number ν for 2D lattices [2, 3].

These quantities characterise ground states which are separated from the excited states by an energy gap, G. For free fermion Hamiltonians, G can be obtained from the eigenvalues ε_i of the matrix h. As stated above, if the ground state energy is $E_{\text{gs}} = \sum_{i=1}^{F} \varepsilon_i$, then the energy of the first excited state would be $E_{\text{1st}} = \varepsilon_{F+1} + \sum_{i=1}^{F-1} \varepsilon_i$. Thus, the gap in this case is $G = E_{\text{1st}} - E_{\text{gs}} = \varepsilon_{F+1} - \varepsilon_F$. In the case where the Hamiltonian is written in terms of free Majoranas, the gap corresponds to exciting the two-level normal-mode with the smallest energy, $G = 2 \min_{i \in \{1,\dots,|\Lambda_v|\}} \varepsilon_i$.

The invariants are extracted from the hopping matrix in momentum space $h(p)$ and are robust under continuous deformations of the Hamiltonian. In particular, let λ be a collection of external parameters that adiabatically deform the hopping matrix, $h(\lambda, p)$. Then the topological numbers of h remain unchanged as long as $G(\lambda) \neq 0, \ \forall \lambda$. In other words, they define the parameter range of a topological phase and they can only change at quantum critical points where $G = 0$ (singular points).

Winding Number

Since we will be interested in chains with 2 sites in the unit-cell we present the winding number for the case of 2-dimensional matrices $h(p)$ where $p \in [0, 2\pi)$. Any such matrix is decomposable on the basis of the 2×2 Pauli matrices, $\mathbb{I}, X, Y, Z$. Defining the Pauli vector $\sigma = (X\ Y\ Z)^T$ and discarding any terms proportional to $\mathbb{I}$ from the Hamiltonian, there exists a vector Σ for which

$$h(p) = \Sigma(p)\,\sigma. \tag{2.8}$$

Normalising the 3D vector $\Sigma(p)$ we can study the path it inscribes on the surface of the unit sphere as we vary the momentum p along the 1D Brillouin zone. In the presence of time-reversal symmetry the winding number is defined as

$$w = \int dp\ \left(\Sigma(p) \times \partial_p \Sigma(p)\right)_z . \tag{2.9}$$

If we call the initial point of $\Sigma(0)$ the north pole of the sphere, the integral 2.9 counts how many times the Σ passes through the south pole $\Sigma(\pi)$ before returning to the north pole again at $\Sigma(2\pi)$. In some examples studied in this thesis we will explicitly plot Σ's path in order to draw conclusions.

Chern Number

For 2D systems, the Chern number of the band with Bloch vector $|n(q,p)\rangle$ is defined as

$$\nu_n = \frac{-i}{2\pi} \int dq dp\ \left(\partial_q A_p - \partial_p A_q\right)\ ,\quad A_p = \langle n(q,p)|\, \partial p\, |n(q,p)\rangle\, , \tag{2.10}$$

where A is the Berry connection and (2.10) is the surface integral of the Berry curvature in the 2D Brillouin zone. This integral counts how many times the path of $\Sigma(q,p)$ covers the whole surface of the unit sphere. For our numerics, we use the discretised version of (2.10) derived in Ref. [4], which has the advantage to be independent of the Brillouin zone's density, or equivalently of the system's size. The idea is to compute the overlaps dictated by the Berry connection for all $dq \times dp$ squares that make up the discrete Brillouin zone and then take their product. This is equivalent to calculating the Berry phase accumulated by

a particle travelling on the boundary on the Brillouin zone as can be seen by applying Stoke's theorem on (2.10). Remarkably, such adiabatic manipulations of single particle states in momentum space can be realised in cold-atoms systems in order to measure topological invariants [5, 6].

Edge States

The topological invariants can be considered a property of the bulk of the system, as we have defined them in momentum space, and momentum space is defined for periodic boundary conditions for a system of finite size, or for an infinite system. However, when we impose open boundary conditions on such topological phases, the non-triviality of the invariants w, ν manifests as exponentially localised states on the edges of the system [3]. The energies corresponding to these edge modes appear mid-gap, and their appearance can be understood in terms of quantum phase transitions in real space. The edge of the system can be thought as an interface between the topologically non-trivial bulk and the trivial vacuum. As both these bulks are gapped, and the gap closes when an topological number changes, we realise that edge states necessarily form with mid-gap energies. One of the goals of the thesis is to establish diagnostic measures for their existence in a given free Hamiltonian.

2.2.2 Single-Body Correlations

In order to study the correlations in the ground state of topological free-fermion systems we employ the correlation matrix C, which contains all two-point correlations of the state, $C_{ij} = \langle f_i^\dagger f_j \rangle$. It is then quite simple to confirm that its elements are given by

$$C_{ij} = \sum_{k=1}^{F} V_{ik}^\star V_{jk}, \tag{2.11}$$

and its eigenvalues are such that $\lambda \in [0, 1]$.

For free Majoranas we can collect the two-point correlations in the correlation matrix $C_{ij} = \langle \gamma_i \gamma_j \rangle$, which we can easily construct by replacing $\pm\epsilon_i \to 0, 1$ respectively in the diagonal of D and conjugating with U. Creating single excitations is straight-forward as we just need to excite one of the two-level systems and so

for that pair of energies we would substitute $\pm\varepsilon \to 1, 0$. We recall that any free fermion system can be written in terms of Majoranas, and this is why we denote with C the covariance matrix of both free fermions and free Majoranas.

From the Majorana-Majorana correlation matrix we can construct the covariance matrix Γ. This is done in accord with the language of Gaussian quantum information. The matrix Γ, containing all the second moments, is defined via the Majorana correlation matrix as [7, 8, 9, 10, 11],

$$\Gamma = i(C - C^T). \tag{2.12}$$

It is a real anti-symmetric matrix, that is $\Gamma^T = -\Gamma$, with eigenvalues coming in imaginary pairs $\pm i\mu_j$ with $\mu_j \in [-1, 1]$. It satisfies $\Gamma^T\Gamma \leq \mathbb{I}$, with equality holding for pure states. The matrix inequality is understood by the definition of a positive semidefinite matrix, $X \geq 0$, being such that all its eigenvalues are non-negative. A free state ρ is called Gaussian because its second moments determine all higher moments. That is, all expectation values of monomials of an even number of Majorana operators can be calculated through Wick's theorem as [12]

$$\langle \gamma_{j_1}\gamma_{j_2}\dots\gamma_{j_{2l}}\rangle = \sum_{\pi} \operatorname{sgn}(\pi) \prod_{k=1}^{l} \Gamma_{j_{\pi(2k-1)}j_{\pi(2k)}}, \tag{2.13}$$

where the j-indices are pairwise different, the sum runs over pairings π of the j-indices and $\operatorname{sgn}(\pi)$ is the parity of the pairing. Any odd Majorana monomial has vanishing expectation value.

2.2.3 Chern Number from Correlation Matrix

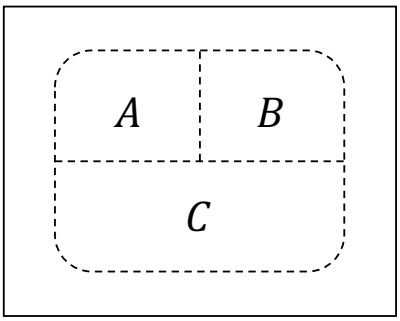

Figure 2.1: Tripartition for computation of Chern number or the topological entanglement entropy.

Having defined the correlation matrix, C, we introduce a useful expression of the Chern number which is formulated in real space in terms of the elements C_{ij}, which we will use when translation invariance is broken due to disorder. We create three non-overlapping partitions $A, B, C \subset \Lambda_v$ with common boundaries that form a triple point as shown in Fig.2.1. The Chern number is defined as [13, 14, 15, 16, 17],

$$\nu = 12\pi i \sum_{j\in A}\sum_{k\in B}\sum_{l\in C}\left(C_{jk}C_{kl}C_{lj} - C_{jl}C_{lk}C_{kj}\right), \tag{2.14}$$

and the prefactor ensures that $\nu \in \mathbb{Z}$. As Kitaev defines it, intuitively this is understood as a chiral sum of "correlation currents".

Note that Hastings [18] has proved that when the ground state is gapped, the correlations decay exponentially, $C_{jk} \sim e^{-\frac{|j-k|}{\xi}}$, where the correlation length is related to the gap as $\xi \sim \frac{1}{G}$ and in particular for frustration free Hamiltonians [19] as $\xi \sim \frac{1}{\sqrt{G}}$. Therefore, the partitions need to be chosen so that their linear size is larger than ξ. Indeed, numerically it is observed that ν as computed from (2.14) converges to its integer value as the system size is increased [20, 21].

2.2.4 Single-Body Entanglement Spectrum

One of the fundamental objects studied in this thesis is the entanglement spectrum. We first need to bi-partition the graph into $A, B \subset \Lambda_v$. Then the single-particle entanglement spectrum is obtained by the sub-matrix $C_{ij\in A}$ and is simply its spectrum, $\lambda = \text{spec}(C_A)$. What is important about λ is that it resembles the edge energy spectrum because partitioning the system simulates an open boundary. A topological phase characterised by a winding or Chern number exhibits "virtual" edge states appearing mid-gap in λ. Indeed, Fidkowski [7] has proved that the entanglement spectrum of a partition is adiabatically connected, or topologically equivalent, to the energy spectrum of the Hamiltonian restricted to that region. Specifically, λ is the band-flattened version of $\text{spec}(h_{ij\in A})$. The important fact that makes Fidkowski's proof work is that C_A and h_A have the same eigenvectors. As we will see in later Chapters, the single-body entanglement spectrum will be used to detect edge states in ground states of topological phases, supplemented with a theorem from quantum information.

Spectral Asymmetry

Here we make some comments on the structure of λ depending on the symmetries that H respects [22]. First, note that, for a Hamiltonian with no pairings where particle numbers are conserved, we have that $\text{spec}(C_A) = 1 - \text{spec}(C_B)$. This inspires an interpretation of λ as probabilities of particles being in A, consistent with assigning the same probabilities of holes to be in B, where we view $\lambda_j > \frac{1}{2}$ as corresponding to particles and $\lambda_j < \frac{1}{2}$ to holes. From this we suspect and confirm that states corresponding to $\lambda_j \approx \frac{1}{2}$ are localised on the virtual boundary, as other studies have shown as well [23]. Therefore, $\lambda \in [0, 1]$ can have a "virtual particle hole symmetry" around $\frac{1}{2}$, when a spatial symmetry, like inversion through the partition boundary or translation invariance, is present and so particles or holes have no bias towards a particular partition. However, one can lift such symmetry by introducing disorder or a chemical potential with a gradient. Now let H respect particle-hole symmetry, in which case, even if the system is disordered and no spatial symmetry is present, we still have a virtual particle hole symmetry because we can both exchange particles with holes and regions A with B, thus leaving λ invariant. Another way to see this is that when pairings are included the natural way to express H is through Majoranas so then λ is symmetric around $\frac{1}{2}$ by construction.

A simple way to capture the asymmetry in λ is to compute its *skewness*. For a discrete distribution $X = x_1, \ldots, x_L$ it is defined as [24]

$$\alpha_3(X) = \frac{m_3(X)}{m_2(X)^{3/2}}, \tag{2.15}$$

where $m_r(X) = \frac{1}{L}\sum_{i=1}^{L}(x_i - \langle X\rangle)^r$ is the rth central moment and $\langle X\rangle = \frac{1}{L}\sum_{i=1}^{L} x_i$ is the arithmetic mean. We will use skewness as a measure of the asymmetry of a given spectrum. We also normalise (2.15) by the maximal possible value it can acquire, $\alpha_3^{\max} = \frac{L-2}{\sqrt{L-1}}$. Finally, note that in general, the number of $\lambda_j > \frac{1}{2}$ is different than that of $\lambda_j < \frac{1}{2}$. For example this is the case when $|A| \neq |B|$, or when the particle number is smaller than the sizes of either A or B. In such cases the skewness would be artificially finite. It is easy to fix this by discarding the λ_js outside of a symmetric window centred around $\frac{1}{2}$.

2.2.5 Entropy from Correlation Matrix

The entanglement entropy of the reduced state of the partition A, can then be expressed in terms of the correlation matrix eigenvalues as [25]

$$S = -\sum_k (1-\lambda_k)\log(1-\lambda_k) + \lambda_k \log \lambda_k. \tag{2.16}$$

If the correlation matrix is in terms of Majoranas, then (2.16) inherits a $\frac{1}{2}$ factor to take care of double-counting degrees of freedom due to the Majorana reality condition. For more details see Appendix A.1.

In terms of the covariance matrix, Γ, the entanglement entropy can similarly be obtained from the eigenvalues μ_j^A of the sub-matrix Γ_A as [26]

$$S = -\frac{1}{2}\sum_j \frac{1+\mu_j^A}{2}\log\frac{1+\mu_j^A}{2}. \tag{2.17}$$

As stated above, edge states in the entanglement spectrum have energies $\lambda \approx \frac{1}{2}$ or $\mu^A \approx 0$. From (2.16) and (2.17) we see that they contribute *maximal* entropic contributions. In the context where we interpret the entanglement spectrum of free fermions with particle conserving Hamiltonian as probabilities of particles and holes being in region A, the maximal entropy is understood as maximal uncertainty about a particle or equivalently the corresponding hole to be in either A or B. It is thus supported on the boundary, ∂A. Supplemented with the finite correlation length induced by the spectral gap, then the mode is exponentially localised at the boundary. This is consistent with Klich's [27] work showing that the reduced state of a particle-conserving Hamiltonian can be written in a Bardeen-Cooper-Schrieffer form which describes superconducting states. A superconducting Hamiltonian does not respect particle populations and the analogy holds due to the fact that the particle number in region A or B is not conserved, but only their sum is. For Majoranas, the maximal entropy contributed is understood as uncertainty about the parity of Majorana modes shared between A and B (or equivalently living on ∂A).

We remind here that the entropy of independent states is additive. A case where this is used is in the presence of a symmetry in the system, such as

translation invariance, when the single particle Hamiltonian matrix can be block-diagonalised $h = \oplus_p h(p)$. Then the entropy of, say, the ground state, is additive in the symmetry sectors, $S = \sum S(p)$.

2.3 Topological Order

We are interested in studying correlations in topologically ordered states, that is, ground states whose degeneracy depends on the topology of the lattice on which the Hamiltonian is defined, and for our purposes we focus on two-dimensional cases only. The low energy physics of such systems is described by topological quantum field theories [28] and the excitations have exotic exchange statistics. These quasiparticles, called *anyons* define a Hilbert space from their fusion rules [2] and together with braiding operations they define a platform for topological quantum computation [29, 30, 31]. Their study is immensely rich and interesting and extends to higher dimensions. However, we will keep the discussion minimal by focusing on aspects of topological orders that are relevant to our diagnostics.

For a general anyon model in 2D with point-like anyons, $\mathcal{J}, \mathcal{J}', \ldots$, the fusion rules are written as $\mathcal{J} \times \mathcal{J}' = \sum_{\mathcal{J}''} N_{\mathcal{J}\mathcal{J}'}^{\mathcal{J}''} \mathcal{J}''$, where $N_{\mathcal{J}\mathcal{J}'}^{\mathcal{J}''}$ is the multiplicity of the fusion channel $\mathcal{J} \times \mathcal{J}' \to \mathcal{J}''$. All anyons have an anti-particle which they fuse to the anyonic vaccum, denoted as 1. When for each pair $\mathcal{J}, \mathcal{J}'$ there exists a single $\mathcal{J}''$ such that $N_{\mathcal{J}\mathcal{J}'}^{\mathcal{J}''} = 1$ and $N_{\mathcal{J}\mathcal{J}'}^{\mathcal{J}'''} = 0$ for any other $\mathcal{J}'''$, the anyons are called *Abelian*. In the *non-Abelian* case the multiplicity makes the fusion outcome non-deterministic. Topological orders with such fusion rules are called *bosonic*. One can generalise to *fermionic topological order* by introducing a $\mathbb{Z}_2$ grading to the fusion rules accommodating the enrichment of the Hilbert space with a fermionic Fock space [32]. In this thesis we study bosonic cases.

Each anyon has a quantum dimension, $d_{\mathcal{J}}$, defined such that $d_{\mathcal{J}} \times d_{\mathcal{J}'} = \sum_{\mathcal{J}''} N_{\mathcal{J}\mathcal{J}'}^{\mathcal{J}''} d_{\mathcal{J}''}$. The quantum dimension is understood as the local Hilbert space dimension associated with that anyon. For a number M of anyons of the same species, $\mathcal{J}$, the dimension of their fusion space asymptotically grows as $d_{\mathcal{J}}^{M-2}$, hence the name [33]. For Abelian anyons we have $d_{\mathcal{J}} = 1, \ \forall \mathcal{J}$ and on an infinite

plane the ground space is one-dimensional. On the other hand, for non-Abelian anyons there exists at least one $\mathcal{J}$ for which $1 < d_{\mathcal{J}} \in \mathbb{R}$.

The fact that the quantum dimension can be non-integer for non-Abelian anyons signifies the non-locality of their growing fusion space. This is the reason that they are regarded promising for storing quantum information as it should be inaccessible to local noise. Of course, when one can store information, one wonders how to manipulate it. Given a certain anyonic state, adiabatically exchanging the positions of anyons, or *braiding* them, corresponds in general to performing a unitary operation to the state. The term braiding is understood by picturing the worldlines of the anyons as they are slowly moved in the 2D plane. The aforementioned unitary is interpreted as the computation whose input is a state of anyons created pairwise from the anyonic vacuum and output the fusion outcomes when the anyons are fused pair-wise after the braiding. The computation can be universal in certain cases, as it is for the Fibonacci anyons realised when $\mathcal{J}$ are irreducible representations of the quantum group $\mathrm{SU}(2)_3$. We remind that universality means that braiding of Fibonacci anyons corresponds to unitary operations that densely cover $U(N)$ to arbitrary accuracy [34]. This formalism for quantum computation is connected to knot invariants, since a braid together with the state preparation and the readout forms a knot, providing another setup where a topological quantum computer would be useful [35].

2.3.1 Many-Body Correlations

Topological order as it is described above emerges in interacting many-body systems, i.e. Hamiltonians with non-quadratic terms in the fermion or Majorana operators. In contrast, topological phases characterised by an invariant and discussed in 2.2.1 can also arise in free systems.

In terms of correlations, the free topological phases are attributed to short range entanglement. These phases are protected by a local symmetry and so they are also called *symmetry protected* phases and their symmetries are employed in order to classify them [36]. In other words, any local unitary transformation that respects the symmetry, cannot induce a phase transition. However, if the unitary is allowed to break the symmetry, then the invariant can change without the gap

vanishing [37]. The language of local unitary circuits is useful as their job is to alter the entanglement locally and thus change the entanglement pattern of a state.

Topological order is understood via global constraints on the many-body correlations due to long-range entanglement and does not arise in free systems. The ground state is massively entangled as a superposition of all states that respect the global conditions dictated by the Hamiltonian. Similarly to the quantum phase transitions for free systems, however, a topological order arising in an interacting model cannot change to another topological order, i.e. one with different anyonic content, without a quantum phase transition. The topological invariants in this case are the genus-dependent ground state degeneracy and exchange statistics of the anyons, as they are stable to local perturbations [38]. That is, a unitary transformation needs to close the gap in order to change the topological order [39, 40], and equivalent topological orders are those connected by unitaries. Symmetries of the Hamiltonian make their classification a rich endeavour by defining equivalence classes of states connected by symmetry respecting unitaries [41]. In general, a state can possess both a non-trivial topological invariant like a winding or Chern number and topological order with anyonic quasiparticles, such as quantum Hall states [42] and the relevant example to this thesis is Kitaev's honeycomb model [13]. These short- and long-range features are distinguished by identifying the entanglement patterns in the state.

2.3.2 Many-Body Entanglement Spectrum and Entropy

We can identify entanglement patterns that characterise a many-body state from the entanglement spectrum. As we mentioned, topological orders appear in interacting systems, and thus we need to work with many-body wave functions. We then cannot only use the correlation matrix to obtain the entanglement spectrum. Rather, in principle, one needs to compute all exponentially-many higher order correlation functions in order to fully determine the wave-function. For a ground state $|\Psi\rangle$ the entanglement spectrum is defined as [43]

$$E_{\mathrm{e}} = \mathrm{spec}(H_{\mathrm{e}}) \ , \ \text{where } H_{\mathrm{e}} = -\log \rho \ , \ \text{and } \rho = \mathrm{tr}_B \, |\Psi\rangle\langle\Psi| \tag{2.18}$$

with ρ being the reduced to A density matrix, and H_e is the *entanglement Hamiltonian*. The entanglement spectrum captures universal properties of H which are reflected in H_e [43, 44, 45, 46]. The eigenvalues $p_j \in [0,1]$ of ρ are $2^{\min|A|,|B|}$ in number, and their logarithms define the entanglement energies $E_\mathrm{e} \in [0,\infty)$. Details on performing the partial trace in (2.18) as well as obtaining the state's *entanglement matrix* can be found in Appendix A.2.

The intuition around the partial trace over B is that assuming that we have access only to A, then we need to integrate over all possible configurations of B. This loss of information is then reflected in the ρ being in general a mixed state. The amount of entanglement between A and B is quantified by the von Neumann entropy of ρ as

$$S = -\sum_j p_j \log p_j. \tag{2.19}$$

2.4 Area Law and Topological Entropy

Finally, since the states that we examine in this thesis are gapped, and for the free systems that we study the Fermi surface is at most zero-dimensional, this implies that the entropy follows the area law [47], in contrast with cases where power-law correlation decay in 1D or a finite dimensional Fermi surface in higher dimensions leading to logarithmic corrections [48, 49]. Area laws for entanglement entropies were established in the context of attempting to derive the Hawking-Bekenstein entropy of a black hole which scales as the area of its event horizon [50]. Since then, an extensive amount of work followed spreading eventually to condensed matter physics [10].

In particular, the entropy S of a partition A whose linear size is sufficiently larger than the correlation length ξ follows

$$S = (\alpha + S_\mathrm{topo})|\partial A| - S_\mathrm{topo} + O(|\partial A|^{-\beta}), \tag{2.20}$$

where $\beta > 0$ and the area law pre-factor $\alpha > 0$ is generally considered to be non-universal. In Ref. [51] it is argued that α can be arbitrarily tuned by varying the microscopic parameters of a free model. In Section 3.2, however, we point to a universal part of it due to the existence of edge states which holds for non-free systems as well.

The constant shift by $S_{\text{topo}} > 0$ signifies the presence of topological order, where S_{topo} is the *topological entanglement entropy*. This reduction in entropy is interpreted as global information that cannot be lost by tracing out a partition and is a manifestation of the global constraints that the Hamiltonian imposes on the topologically ordered state. It is universal as it depends only on the anyonic content of the topological order which is unchanged under microscopic deformations of the system.

In order to identify whether a given gapped state is topologically ordered, one can perform a scaling of region A and identify S_{topo} as the off-set at $|\partial A| \to 0$. Importantly, Kitaev and Preskill introduced a method to compute S_{topo} for 2D systems involving a linear combination of entropies of a tripartition A, B, C with a triple point [52]. Such a tripartition is depicted in Fig. 2.1. The topological entanglement entropy of a 2D system is defined as

$$S_{\text{topo}} = S_A + S_B + S_C - S_{AB} - S_{AC} - S_{BC} + S_{ABC}. \tag{2.21}$$

The idea is that the terms proportional to the boundaries of the partitions cancel out, leaving only the constant term. Levin and Wen in an independent study proposed a different partition with the same principle in mind [53]. The anyons, $\mathcal{J}$, emerging in the topological order, manifest in the topological entanglement entropy as $S_{\text{topo}} = \log \mathcal{D}$, where $\mathcal{D} = \sqrt{\sum_{\mathcal{J}} d_{\mathcal{J}}^2}$ is the *total quantum dimension*.

2.5 Summary

We have introduced the entanglement spectrum in the single- and many-body contexts, obtained from a bipartition of a many-body fermionic state. The former is relevant for topological phases realised by quadratic Hamiltonians, while for topological orders one needs to study the latter, since topological order only arises in interacting systems. The entanglement spectrum's usefulness stems from the fact that it reflects universal properties of the Hamiltonian through the bulk-boundary correspondence. Its von Neumann entropy measures the amount of entanglement across the cut, and its behaviour with respect to the cut can provide information about the short- and long-range topological order in the state.

Chapter 3

Entanglement Diagnostics

3.1 Introduction

In this chapter we introduce two novel diagnostic measures capturing interesting properties of topological ground states. These measures take as input only correlations of the state. First, we invoke the *monogamy of entanglement* in order to capture the existence of edge states in a given fermionic state from their signature in the state's covariance matrix. Second, we define the *interaction distance*, a measure of the non-Gaussianity of the state, as captured by the structure in the entanglement spectrum.

3.2 Entanglement Monogamy and Edge States

For an arbitrary bi-partition of the system in regions A and B the covariance matrix can be written as

$$\Gamma = \begin{bmatrix} \Gamma_A & \Gamma_{AB} \\ -\Gamma_{AB}^T & \Gamma_B \end{bmatrix}, \tag{3.1}$$

with Γ_A containing the second moments of the reduced state ρ and Γ_{AB} capturing correlations between A and B.

If Γ corresponds to a pure Gaussian state, which implies $\Gamma^T\Gamma = \mathbb{I}$, then the singular values ξ^{AB} of Γ_{AB} and the eigenvalues μ^A of Γ_A satisfy

$$(\mu_j^A)^2 + (\xi_j^{AB})^2 = 1. \tag{3.2}$$

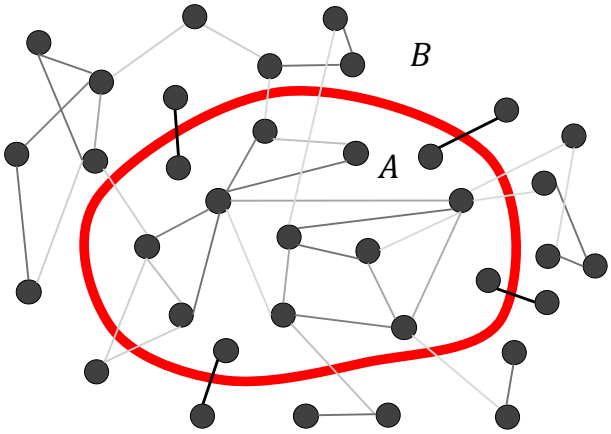

Figure 3.1: Illustration of monogamy among modes (dots) supported in A or B. Entanglements are represented by lines (grey scale). Maximally entangled (black lines) modes localised on either side of ∂A contribute $\xi^{AB} = 1$ and maximal entropy $\frac{1}{2}\log 2$. The thickness of ∂A represents the correlation length ξ. Weaker entanglements (grey lines) crossing ∂A contribute $\xi^{AB} < 1$.

This relation can be easily checked for the simplest case of the pure state of two modes, given below in Eq. (3.3) (in that particular case one has $\Xi^T\Xi = \mathbb{I}$ leading to where one finds $a^2 + b^2 = 1$). The modes in region A with $\mu_j^A = 0$, which always come in pairs, are uncorrelated with the rest of the modes supported in A. Consequently, they are maximally entangled with modes in B as captured by their corresponding $\xi_j^{AB} = 1$. As stated in Section 2.2, they manifest as virtual edge states identified in the entanglement spectrum of topological free fermion systems, and contribute a maximal entropy of $\frac{1}{2}\log(2)$ per mode [7]. Note that this contribution is none other than what the quantum dimension $d_\gamma = \sqrt{2}$ that a Majorana dictates.

3.2.1 Entanglement Monogamy

Monogamy of entanglement states that two maximally entangled modes in a many-body state cannot be entangled with any other mode. For our bipartitioned system this means that no mode in A which is maximally entangled with a mode in B can be entangled with any other mode in A or B [54, 55]. In general, maximally entangled modes across ∂A are witnessed by singular values $\xi_j^{AB} = 1$ of Γ_{AB}. These then imply corresponding eigenvalues $\mu_j^A = 0$. However, the converse is not true in general, save for free systems. Monogamy relations can also be quantified with entanglement measures and so the same statements are

made for highly entangled modes being minimally entangled with the rest. In Fig. 3.1 we illustrate the monogamy relations.

Now we can employ the monogamy relations between modes of a multi-mode system to argue about the existence of edge states in gapped phases. For a physical edge, one in principle can construct operators with exponentially decaying support in the bulk that create edge states in many-body systems [56]. Via the bulk-boundary correspondence, we argue that the same the same pattern is followed by the virtual edge states on ∂A. These operators commute with the Hamitlonian to exponential precision. They, however, anticommute with a symmetry of the Hamiltonian and thus induce a ground state degeneracy for open boundaries which is exponentially precise as a function of the system size. The fact that these operators commute with H means that the states they create are decoupled from the rest of the modes, and thus uncorrelated with them. Invoking the monogamy signature witnessed by the Γ_{AB} block of the covariance matrix we conclude that its $\xi^{AB} \approx 1$ singular values correspond to the existence of virtual edge states localised at ∂A.

To exemplify this behaviour we focus on the generic covariance matrix Ξ of the state σ of two fermionic modes. In its normal form it reads

$$\Xi = \begin{bmatrix} \Xi_A & \Xi_{AB} \\ -\Xi_{AB}^T & \Xi_B \end{bmatrix}, \; \Xi_A = \begin{bmatrix} 0 & a \\ -a & 0 \end{bmatrix}, \Xi_B = \begin{bmatrix} 0 & d \\ -d & 0 \end{bmatrix}, \Xi_{AB} = \begin{bmatrix} 0 & b \\ c & 0 \end{bmatrix}, \tag{3.3}$$

to which it is possible to rotate by conjugating with $O_A \oplus O_B$. The rotations $O_{A,B} \in \mathrm{SO}(2)$ act independently on each partition and thus do not change the entanglement across ∂A. This covariance matrix corresponds to a *pure maximally entangled* state when $\Xi^T \Xi = \mathbb{I}$, which occurs for $|b| = |c| = 1$, and as a consequence $a = d = 0$. Now let the $\min(|b|, |c|) > 1 - \varepsilon$ be the smallest singular value of Ξ_{AB}. Performing a Jordan-Wigner transformation on the state of the A and B fermions with covariance matrix given by (3.3) we see that the state σ can be written as $\sigma = (1 - \varepsilon)\omega + \varepsilon\eta$, where ω is a maximally entangled state of minimal rank and η an orthogonal residual state. In particular, for $\min(|b|, |c|) > 1 - \varepsilon$, we can estimate that

$$D(\sigma, \omega) \leq \varepsilon, \tag{3.4}$$

where

$$D(\alpha,\beta)=\frac{1}{2}\mathrm{tr}|\alpha-\beta| \tag{3.5}$$

is the *trace distance* for α,β Hermitian matrices. Hence, by considering the singular values ξ^{AB} of Ξ_{AB} we can deduce how close σ is to a maximally entangled state ω. The argument generalises to a multi-mode setting. If there exist many singular values such that $\xi_j^{AB}\geq 1-\varepsilon,\ j=1,\ldots,2k$ then one can identify a subspace of the Hilbert space containing k pairs of fermionic modes that are highly entangled. In other words, their trace distance is ε-close to a product state of k-many maximally entangled pairs.

Furthermore, the monogamy relations in the many-body setting dictate that these almost maximally entangled modes are largely disentangled from the rest of the fermionic modes [54, 55]. This can be quantified by entanglement measures which we define below. Let us first focus on the reduced state supported on modes F_1 and F_2 of the multi-mode state. Suppose they are close to a maximally entangled state in the sense that their state is written as $\sigma=(1-\varepsilon)\omega+\varepsilon\eta$, as above. Then the mode F_1 will be little entangled with any F_j mode of the system, and F_1 and F_2 as a pair are disentangled from the rest of the modes.

These properties can be captured by the *entanglement of formation* which for a specific bipartition is defined as [57]

$$E_F(\zeta)=\min_{\{p_i,|\psi_i\rangle\}}\sum_i p_i S_i, \tag{3.6}$$

where the minimum is taken over the ensemble of pure states $|\psi_i\rangle$ that realises the mixed state $\zeta=\sum_i p_i\,|\psi_i\rangle\langle\psi_i|$, with $\sum_i p_i=1$. Here, S_i is the von Neumann entropy of each pure state for that bipartition.

For mode F_1 we have that the sum of all entanglements of formation $E_F(1:j)$ between S_1 and any other mode F_j, except F_2, is upper bounded [58, 54, 55],

$$\sum_{j=3}^{N}E_F(1:j)^2\leq\left(1-(1-\varepsilon)^2\right)\log^2 2, \tag{3.7}$$

and is hence small if ε is close to zero. The notation $E_F(1:j)$ means that the bipartition is between modes F_1 and F_j and the rest of the modes $F_{k\neq 1,j}$ have been

traced out. This bound is derived considering the *tangle*, a measure of mixedness similarly defined to the entanglement of formation. The tangle is defined as

$$\tau(\zeta) = \min_{\{p_i, |\psi_i\rangle\}} \sum_i p_i S_{Li}, \tag{3.8}$$

where S_{Li} is the linear entropy of each reduced $|\psi_i\rangle\langle\psi_i|$ for the bipartition in question. The linear entropy is simply the opposite of the purity and for a density matrix α it is defined as $S_L(\alpha) = 1 - \mathrm{tr}(\alpha^2)$, where $\mathrm{tr}(\alpha^2) \leq 1$ is the purity achieving equality when α is pure. The two entanglement monotones are related as [54, 55] $E_F \geq \tau \log 2$ and $E_F^2 \leq \tau \log^2 2$. This implies that $E_F(1:2) \geq (1-\varepsilon)\log 2$, with the convention that $E_F(\omega) = \log 2$. Then to derive the bound (3.7) we invoke the multi-partite monogamy relation derived by Osborne and Verstraete in Ref.[55],

$$\tau(1:2) + \tau(1:3) + \cdots + \tau(1:n) \leq 1. \tag{3.9}$$

The situation is equivalent for F_2 and its entanglement with the other F_j modes. We point to Appendix B.2 for the proof of this bound. For the pair F_1 and F_2 we can see that it is minimally entangled with all other modes as a whole, in the sense that

$$E_F(1, 2 : 3, \ldots, N) \leq \varepsilon 2 \log 2. \tag{3.10}$$

This bound is derived by using the fact that τ, and consequently E_F, is a convex function over the set of density matrices [57], and using that a maximally entangled fermion pair contributes $\log 2$ entanglement. Again, we can straightforwardly generalise to the case where we have $\xi_j^{AB} \geq 1 - \varepsilon,\ j = 1, \ldots, 2k$. Then there exist k-many modes that are at most $2k\varepsilon \log 2$ entangled with the modes forming the complement of the system.

This result is general and applies to both free and interacting fermionic systems alike, where only the covariance matrix has been considered. It states that, due to their maximal correlations across ∂A, virtual edge modes appear as largely disentangled from the rest of the system. In 1D systems this decoupling dictates that the edge states appear as zero modes in the entanglement spectrum. In 2D systems they appear as mid-gap states in general. Thus, simply by investigating the singular values of Γ_{AB} we can diagnose the existence of edge states in a many-body system.

3.2.2 Entropic Lower Bound

Going further, the existence of edge states in topological systems implies a lower bound for the entanglement entropy. The existence of virtual edge states implies a lower bound for the entanglement entropy. In terms of the covariance matrix we have (see Appendix B.3 for proof)

$$S(\rho_A) \geq \frac{1}{2}\|\Gamma_{AB}\|_2^2 \log 2, \tag{3.11}$$

where the 2-norm for a Hermitian matrix X is defined as $\|X\|_2^2 = \mathrm{tr}(X^2)$ and corresponds to the sum of the squared singular values. For its interpretation note that the entropic contributions from the bulk states can be adiabatically removed. However, virtual edge states are topologically protected in the sense that they are robust under adiabatic deformations of the corresponding physical Hamiltonian [59, 60].

This has a consequence regarding the area law coefficient α in (2.20). In general α depends on microscopic parameters of a given model describing a many-body system. However, since topological phases are characterised by $\|\Gamma_{AB}\|_2^2 \neq 0$ and the lower bound (3.11) for them is non-trivial, then the area law coefficient α can never be made zero. On the other hand, for a topologically trivial system, one can always tune $\alpha \to 0$ by increasing the energy gap so that the correlation length shrinks.

3.2.3 Entanglement Qualifier

Using monogamy of entanglement we have concluded that almost maximally entangled modes of a many-body system are witnessed by singular values $\xi_j^{AB} \approx 1$ of Γ_{AB}. In analogy with the entanglement gap [61], they are separated by a *covariance gap* from the lower ξ_j^{AB} corresponding to non-universal bulk states. This allows the definition of a diagnostic tool that extracts the signature of the maximally entangled pairs, thus probing the topological character of the system. To count the number of such modes in a way robust to imperfections and finite system sizes, we define the entanglement qualifier $\mathcal{S}_q$ as

$$\mathcal{S}_q = \mathrm{tr}(\Gamma_{AB}^\dagger \Gamma_{AB})^q, \quad \text{with } 0 < q \in \mathbb{N}. \tag{3.12}$$

In the limit $q \to \infty$ this quantity converges to the number of maximally entangled modes across ∂A in units of Majoranas. A Dirac mode counts as two Majoranas. This qualifier, therefore, detects the existence of physical edge states at open boundaries only by considering correlations in the ground state for closed boundaries.

3.2.4 Open Questions

Now we pose open questions regarding monogamous edge states in systems composed of particles more exotic than fermions, such as parafermions [62] or other fractionalised quasiparticles with exotic exchange statistics [42]. Such systems also host edge states whose dimensionality cannot be counted in units of Majoranas as we have done for fermionic systems. Moreover, monogamy relations can be violated [63] for higher dimensional local Hilbert spaces [64]. Another direction regarding fermions is that of Floquet topological systems. They are trivial states which under periodic driving acquire a topological invariant [65] and edge states in the time domain. The question is whether monogamy relations [66] can be formulated for such cases.

3.3 Entanglement Freedom

As stated in subsection 2.2.2, the computation of expectation values of free systems only involves polynomials of covariance matrix elements. Furthermore, time evolution is executed by conjugating operators with the time evolution operator which is Gaussian since the Hamiltonian is quadratic. Thus we know that free fermion systems are efficiently simulatable on a classical computer. In contrast, interacting systems pose the hardest problems in theoretical physics, as their complexity is in general exponential. This is due to the fact that a many-body state needs an exponentially large number of parameters to be specified.

Traditionally one uses mean-field, density functional, or perturbation theory to expand around points in the parameter space where the solution is known because this instance of the model is non-interacting. These approaches can be employed when correlations are weak, or interactions induce small corrections

to the state of the solvable point. The idea commonly is to smoothly connect the physics back to a local free theory. There is also the special case of *integrable systems* [67], which have an extensive number of integrals of motion. They accept complete analytical solutions but they are not robust to perturbations of the Hamiltonian. Importantly, their correlations, even though they may be structured, they are not all contained in the covariance matrix as is the case for free-systems.

Commonly interesting many-body phenomena are emergent, and so they cannot be treated perturbatively. Examples from condensed matter physics are high-T_c superconductivity or the fractional quantum Hall effect. Huge leaps in understanding of such systems have been obtained using variational ansätze [68, 69, 70, 71]. However, these results were based on highly non-trivial physical intuition on the physicist's part about the nature of the emerging free quasiparticles. Modern methods in condensed matter physics such as tensor networks [72, 73, 74] or neural networks [75, 76, 77] aim to compress the description of a many-body state in order to efficiently compute observables and simulate time evolutions. Again, these methods are variational in nature.

In this section we introduce our contribution towards this endeavour. We define the *interaction distance*, a measure of the effect that interactions have on the correlations of a quantum many-body state, i.e. the entanglement spectrum. Simultaneously, the interaction distance determines the emergent quasiparticles in which the state can be regarded as Gaussian. In order to achieve this, we have generalised the meaning of "freedom" and allowed the emergent modes on which the state is free to be non-local. The computation of the interaction distance is shown to be efficient and so we envision that it can be combined with existing variational ansätze for many-body states or that it will aid numerical simulations of interacting systems so that they scale favourably with the system size.

3.3.1 Free-Fermion Many-Body Entanglement Spectrum

For a bipartition A, B, the eigenvalues λ of the reduced correlation matrix C_A, which we defined as the single-body entanglement spectrum in 2.2.4, are "$1-1$" related with the *single-body entanglement energies* ϵ, as proved by Peschel [25].

That is, for *free-fermion* Hamiltonian, the reduced ground state of partition A can be written as a *Gaussian*

$$\rho = \frac{e^{-H_A^\flat}}{Z}, \tag{3.13}$$

where $Z = \mathrm{tr} e^{-H_A^\flat}$, and $H_A^\flat = \sum_{ij\in A} h_{ij}^\flat f_i^\dagger f_j$ is the bland-flattened *free-fermion* Hamiltonian restricted to region A, as mentioned in 2.2.4. See Appendix A.1 for more details. The set ϵ is the eigenvalue set of the matrix $h_{ij\in A}^\flat$, and naturally there exist corresponding normal modes c with support on partition A. The modes c are a polynomially large subset (single particle sector) of the exponentially large set of the Fock basis of A (left Schmidt vectors). This is seen when the Gaussian state is written in the diagonal basis as $\rho = \frac{1}{Z} e^{-\sum_{i=1}^{|A|} \epsilon_i c_i^\dagger c_i}$.

The set ϵ constructs the *free many-body entanglement spectrum* comprising the entanglement energies E_e in Eq.(2.18), as a consequence of Wick's theorem and Fermi-Dirac statistics. For N single-particle entanglement energies ϵ_i, we have the 2^N energies [8]

$$E_\mathrm{e}^\mathrm{f}(\epsilon) = E_{\mathrm{e}0} + \oplus_{i=1}^N \{0, \epsilon_i\}, \tag{3.14}$$

where $E_{\mathrm{e}0} = -\sum_i \log Z_i$ is the normalising background energy with $Z_i = 1 + e^{-\epsilon_i}$ being the normalisation of each entanglement mode ϵ_i. Note that this is also the structure of the energy spectrum of a free fermion system at zero temperature. Equivalently, in terms of the eigenvalues p of the free reduced density matrix ρ^f, we have

$$p^\mathrm{f} = \otimes_{i=1}^N \frac{1}{Z_i}(1, e^{-\epsilon_i}), \tag{3.15}$$

reflecting the fact that each mode can have occupation $n_i = 0, 1$ according to Fermi-Dirac statistics with Boltzmann-like probabilities weighted by their energies. Our convention is to order the energies as ascending $\epsilon_i \leq \epsilon_j,\ i \leq j$, and so $E_{\mathrm{e}i} \leq E_{\mathrm{e}j},\ i \leq j$. The corresponding probability spectrum is then ordered in descending order $p_i \geq p_j,\ i \geq j$.

3.3.2 Many-Body Spectral Asymmetry

Now let E_e be a generic entanglement spectrum. We would like to *measure its Gaussianity*, i.e. to what extent it obeys the structure of (3.14) which is dictated

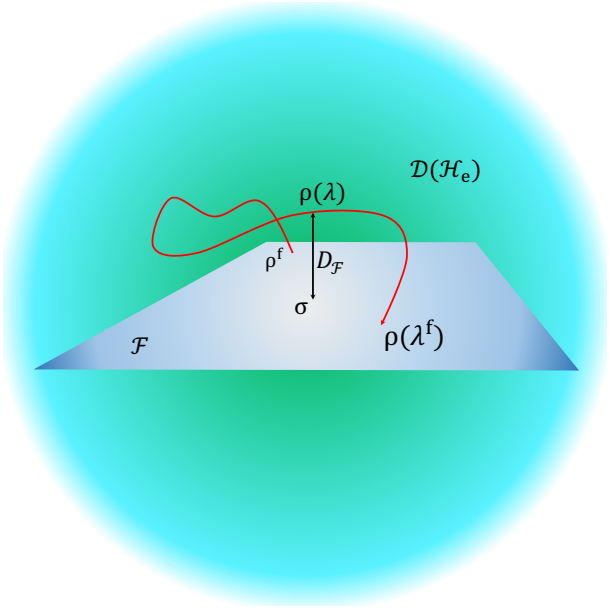

Figure 3.2: Illustration of emergent freedom. Gaussian ground state $\rho^f \in \mathcal{F}$ in the free manifold $\mathcal{F}$ gains finite interaction distance $D_{\mathcal{F}}(\rho(\lambda)) > 0$ from a Gaussian $\sigma \in \mathcal{F}$ when interactions tuned by parameters λ are introduced to the Hamiltonian. It is possible that there exist λ^f such that $\rho(\lambda^f) \in \mathcal{F}$, which is embedded in the space of density matrices of the entanglement Hilbert space, $\mathcal{D}(\mathcal{H}_e)$.

by Wick's theorem. Observe that any free spectrum is symmetric around its mean $\langle E_e \rangle$. Explicitly, this means that $\forall E_j \leq \langle E_e \rangle$, there exists a $E_k \geq \langle E_e \rangle$ with $j \leq k$ such that $|E_{ej} - \langle E_e \rangle| = |E_{ek} - \langle E_e \rangle|$. Then the addition of non-quadratic terms in the Hamiltonian does not allow for a description of the state through only its second moments and so the asymmetry of the entanglement spectrum quantifies how invalid Wick's theorem becomes.

Interestingly, it is not disallowed that the state has an *effective free description* even in the presence of interactions. Then the symmetry in the entanglement spectrum will re-emerge, and obey the free structure (3.14). These cases are of particular interest as they would be truly emergent phenomena.

A naive simple measure of the asymmetry is the third moment, or the skewness $\alpha_3(E_e)$, which is defined in (2.15). Of course, $\alpha_3(E_e) = 0$ when the spectrum is symmetric level-wise as described above, but the converse is not true. This is reasonable as only the third moments do not fully characterise a distribution. However, we can use it as a first easily applicable diagnostic.

3.3.3 Interaction Distance

The *interaction distance*, $D_{\mathcal{F}}(\rho)$, of a state $\rho \in \mathcal{D}(\mathcal{H}_{\mathrm{e}})$ in the entanglement Hilbert space, is defined as the trace distance to the closest Gaussian state σ

$$D_{\mathcal{F}}(\rho) = \min_{\sigma \in \mathcal{F}} D(\rho, \sigma), \tag{3.16}$$

where $D(\cdot, \cdot)$ is the trace distance defined in (3.5) and $\mathcal{F}$ is the manifold of all Gaussian states. In other words, σ is any state of the form of (3.13). We have chosen this distance measure as it has an operational interpretation in terms of distinguishability between ρ and σ when measuring observables [78]. In particular,

$$D(\rho, \sigma) = \max_{P} \mathrm{tr}(P\rho - P\sigma), \tag{3.17}$$

where $0 \leq P \leq \mathbb{I}$ is a positive semidefinite matrix representing a measurement. Thus $D(\cdot, \cdot)$ is the maximal probability of distinguishing between two states by measuring in the optimal basis of observables. In case $D_{\mathcal{F}}(\rho) = 0$ exactly, there exists a Gaussian σ with the same spectrum. Finally, since the trace distance is upper bounded by unity, we know that $D_{\mathcal{F}}$ shares the same upper bound. A geometric interpretation of $D_{\mathcal{F}}$ is illustrated in Fig.3.2 and for further comments on this figure see Appendix B.6.

Efficient Representation of the Optimisation Problem

In order to compute $\mathcal{D}_{\mathcal{F}}$, we need to perform the minimisation in Eq. (3.16). Consider the trace distance between two density matrices $D(\alpha, \beta)$. In general, $\alpha, \beta \in \mathcal{F}$ need not be diagonal in the same basis. Let us rotate to the basis of one of them, say α. The matrix β is relatively rotated by some unitary W with respect to α. Now we invoke the result of Ref [79] which states that $D(\alpha, W^{\dagger}\beta W)$ is minimised when $W = \mathbb{I}$, and so the two density matrices are simultaneously diagonal. Furthermore, their spectra need to be sorted in the same order, as any other relative shuffling increases the trace distance. This is because for diagonal matrices the trace distance (or Kolmogorov distance) is just the sum of the absolute values of the pairwise differences of their eigenvalues.

We can gain intuition by considering the trivial case where α and β each represent a single mixed qubit. In such a set-up $D(\alpha, \beta)$ is proportional to the

Euclidean distance of their corresponding Bloch vectors $\Sigma_{\alpha,\beta}$. Suppose that we work in the computational basis of α so that Σ_α lies on the positive z-axis. In general, Σ_β is at an angle θ relative to the z-axis. Then varying the length of Σ_β we can find how mixed it has to be so that $D(\alpha,\beta)$ is minimised. However, this minimum is as low as possible when $\theta = 0$. In this particular case $D(\alpha,\beta) = 0$ is always achievable.

Using this result, we consider that ρ is diagonal so its entanglement spectrum E_e is accessible, and also the basis is permuted so that it is rank-ordered. Then we need to vary *only the spectrum* of σ. Having to minimise only with respect to the spectrum of σ is a significant reduction in complexity of minimising $D_\mathcal{F}$. Another consequence is that the eigenstates of the optimal model σ are the same as the eigenstates of ρ. Now recall that σ's entanglement spectrum is constructed by ϵs as (3.14). Thus the interaction distance can be cast as

$$D_\mathcal{F}(\rho) = \min_\epsilon \frac{1}{2}\sum_k |e^{-E_k} - e^{-E_k^\mathrm{f}(\epsilon)}|. \tag{3.18}$$

Note that even if the search-space of the problem is exponentially large, this problem is classified as *efficient* as the set of variational parameters ϵ is polynomially-large. For more details see Appendix B.5. We provide details on how this optimisation is performed numerically in Appendix B.4.

Properties of the Interaction Distance

Now that we are equipped with an efficient way to compute $D_\mathcal{F}$ numerically for any given entanglement spectrum, we can ask what its distribution is over generic states. In Appendix B.6 we present a numerical study on random states sampled from $\mathcal{D}(\mathcal{H}_\mathrm{e})$. We find that $D_\mathcal{F}$ follows accurately a log-normal distribution over the sample. Furthermore, we confirm that the maximal value attainable is $D_\mathcal{F}^\mathrm{max} = 3 - 2\sqrt{2}$, which is significantly lower than the naive upper bound at unity concluded by the upper bound of the trace distance. Note that the most common value of $D_\mathcal{F}$, as observed numerically from sampling random states, is approximately $\frac{1}{5}D_\mathcal{F}^\mathrm{max}$. Furthermore, our numerical results confirm our conjecture, $D_\mathcal{F}(\rho) = D_\mathcal{F}\left(\frac{1}{2}(\rho \oplus \rho)\right)$, stating that a doubly degenerate spectrum has the same interaction distance as its non-degenerate version. This we interpret as

the existence of a zero-mode $\epsilon = 0$ in the entanglement spectrum. We can now use the monogamy relations discussed in Section 3.2 to argue that such a mode would be decoupled from the rest and so would not participate in correlations induced by interactions.

Note that besides $D_{\mathcal{F}}$ being a well defined quantity with an operational interpretation, a practical reason to use it instead of simpler measures, such as moments of E_{e}, is that it is quite common that the orders of magnitude spanned by E_{e} are not accommodated by machine precision. The interaction distance on the other hand, does not need all of the entanglement spectrum to faithfully diagnose the entanglement freedom of the state since it exponentially favours the low-lying entanglement levels which are the most physically relevant ones as they correspond to highest Schmidt weights. In addition, by the operational interpretation of the trace distance, we can understand $D_{\mathcal{F}}$ as a measure of the error one makes in computing expectation values using the optimal free state σ instead of the original state ρ.

Alternative state-distance measures may equally well be employed, such as the relative entropy [80]. Throughout this thesis, however, the convention is that $D_{\mathcal{F}}$ is measured with $D(\cdot,\cdot)$. We have found that the numerical investigations presented in Chapter 6 and in Appendix B.6, are qualitatively unaffected by the choice of the relative entropy.

The Role of the Partition

Recalling that ρ depends on the bipartition, we expect that $D_{\mathcal{F}}(\rho)$ depends on it as well. Depending on the dimensionality and the correlation length in the system, $D_{\mathcal{F}}(\rho)$ behaves accordingly. To be more precise, we define a system as free if $D_{\mathcal{F}} = 0$ for all partitions. Note, that the partitions need to be large enough compared to the correlation length of the interacting system.

We can precisely comment, on extreme and trivial cases. Let the biparition be such that A contains one site and B all the other sites. According to the Schmidt decomposition, $\mathcal{H}_{\mathrm{e}}$ is 2-dimensional, and so the entanglement spectrum has 2 eigenvalues. Then a single ϵ can be found to recreate this spectrum. Next, consider the case of the trivial cut, i.e. either A or B contain no sites. Let the

empty partition be A. We can tensor a third system C which is disentangled with B. Now the cut is between B and C and the reduced state of either is pure with spectrum of one non-trivial eigenvalue at 1 and the rest are zeros. Then this spectrum is trivially constructed by setting $\epsilon_j \to \infty$, $\forall j$, and so $D_{\mathcal{F}} = 0$. In this way the interaction distance treats the whole of B as a mode which is occupied with probability 1. In other words the interaction distance measures how interacting a partition is with its complement.

From a quantum information point of view, the partial trace for a particular bipartition can be seen as a quantum channel which maps the pure ground state to the reduced mixed state. Here, by quantum channel is meant a trace-preserving map which keeps the eigenvalues non-negative. Furthermore, a channel is called Gaussian if it preserves the Gaussianity of a state [81], and we remind that a pure state is considered Gaussian. Thus, by matching the spectrum of ρ with a Gaussian spectrum we are searching for modes c defined on the partition so that the partial trace is a Gaussian map, the extent of which is measured by $D_{\mathcal{F}}$.

On the Nature of the Optimal Free Modes

We now refer to previous works defining correlation measures of mixed states [82, 83, 84, 85, 86, 87]. What is novel in our approach is that $\mathcal{F}$ over which we are optimising contains all Gaussian states. That is, we allow them to be defined on any set of fermionic quasiparticle operators c.

We can gain insight about the modes c of σ by following the argument which reduced (3.16) to (3.18), and is a generalisation of our two-qubit example. The free state manifold $\mathcal{F}$ is decomposed in equivalence classes of unitarily equivalent Gaussian states. Within each class, the trace distance is minimised by a certain representative σ which commutes with ρ [79]. Then, $D_{\mathcal{F}}$ is obtained by taking the minimum over representatives of each class. Since the trace distance is minimised when σ and ρ are simultaneously diagonal, the free modes c are the Schmidt vectors corresponding to the single-particle entanglement levels ϵ we have optimised for. Importantly, these unitarily transformed modes are, in general, a *non-linear* combination of the modes of the microscopic model. That is, for the cost of freedom, we have abandoned simplicity of the quasiparticles' internal structure.

In addition, we consider that the entanglement spectrum generically separates into a long-wavelength part (low entanglement energies), carrying universal information about the system, and a short-distance part which is non-universal. These different physical regimes can be probed by varying the linear size of the partition A relative to the size of quasiparticles. Assuming A is much larger than that, the long-wavelength information in the entanglement spectrum comes from correlated quasiparticle excitations across the cut. For small partitions the structure of the quasiparticles becomes apparent and $D_{\mathcal{F}}$ in general is finite since the quasiparticles emerge out of interactions.

3.3.4 Generalised Freedom and Generalised $D_{\mathcal{F}}$

According to (3.18) the interaction distance vanishes when the entanglement spectrum of ρ satisfies the free fermion structure given in (3.14) for certain single-particle energies, ϵ. This generalises the concept of "freedom" in fermionic models. In general no ϵ's exist that satisfy all the constraints imposed by the free-fermion entanglement structure, as their number grows exponentially with the system size, while the number of ϵ's grows only linearly. With this in mind we can interpret the interaction distance as a measure of the complexity of a state. Naturally, this point of view defines free states as those of lowest complexity. Note also that the notion of freedom is tied to the statistics of the free modes c we are optimising over. Changing the entanglement structure that we consider free corresponds to changing the free manifold $\mathcal{F}$ from which the interaction distance is measured. In general, the corresponding "free" structure might imply that single-body levels themselves are occupation-dependent.

Now a concern arises regarding the incompatibility of the size of reduced density matrices of degrees of freedom with unequally large local Hilbert spaces. Considering that these reduced states live on $\mathcal{H}_{\mathrm{e}}$ obtained after a Schmidt decomposition of the state, it is possible to tensor ancillary modes to either partition, which are orthogonal to all other modes, that contribute no entanglement across the cut. This amounts to padding the spectrum of ρ or σ with zeros, which changes their dimension but not their rank which is of physical importance. If the dimension of $\mathcal{H}_{\mathrm{E}}$ is made to exceed the Hilbert space dimension of either

subsystem, then upon Schmidt recomposition non-physical states with highest entanglement energies are projected out.

3.3.5 Comments on the Efficiency of Computing $D_{\mathcal{F}}$

Our motivation to use the entanglement spectrum to diagnose the effect of interactions is that H_{e} inherits universal properties of H for a generic many-body system. Importantly, the calculation of $D_{\mathcal{F}}$ requires only the knowledge of the ground state, thus it is more efficient than examining freedom in the energy spectrum which is more expensive to compute in general.

In Appendix B.5 we elaborate on the efficiency of the optimisation that computes $D_{\mathcal{F}}$. The efficiency of determining the ground state in the first place depends on the dimension of the system. For critical 1D systems, logarithmic corrections to the area law are possible, which leads to the polynomial complexity in determining ρ. For critical 1D states, a multi-scale renormalisation ansatz [74] can be implemented in order to obtain the entanglement spectrum. For higher-dimensional systems, our method is reliant on the efficiency of the current methods in the literature for computing the entanglement spectrum of the ground state. For 2D systems, one can use iterative methods such as the Lanczos algorithm in order to access only the ground state in the exact diagonalisation framework. Furthermore, Monte-Carlo algorithms [88] and 2D tensor networks [73, 72] can be used in a variety of systems to variationally approximate the ground state in a framework where the entanglement spectrum is naturally obtained.

3.3.6 Open Questions

A central open question remains. Is there a procedure to determine the free effective physical Hamiltonian acting as parent of the reduced state σ? Recall that c and σ change depending where we cut. So the free parent Hamiltonian needs to have a ground state which is compatible with all cuts larger than ξ. This procedure need not be unique, as a ground state can have many parents. An approach utilising two-point correlations is presented in Refs. [7, 89].

We have observed that $D_{\mathcal{F}}$ is sensitive to the renormalisation flow of given models. It is an open question whether this can be formulated concretely. Now, a property of the trace distance is that it decreases under a lossy quantum channel. In other words, two states become more indistinguishable when we lose information about them. Interestingly, renormalisation can be viewed as a lossy quantum channel. Hence, this formalism may pave the way to understanding $D_{\mathcal{F}}$'s behaviour under the renormalisation.

Finally, we mention another measure relying on reduced states to which $D_{\mathcal{F}}$ can be connected. First, there has been considerable research on generalised Pauli constraints [90]. There, a one-particle density matrix is obtained by tracing out all other Fock states. Then its spectrum is used to define coordinates in a hypercube, one of the corners of which is the Hartree Fock point containing all free states. It is an interesting question how $D_{\mathcal{F}}$ is related to the distance of that vector from the free corner. Note that in our formalism the manifold $\mathcal{F}$ in general extends throughout $\mathcal{D}(\mathcal{H}_{\mathrm{e}})$ since we cut in real space where the particles are delocalised, in contrast with the Hartree Fock corner which is localised due to single particle states being a subset of the Fock basis.

3.4 Summary

In this chapter we introduced two novel entanglement diagnostics; the monogamy qualifier that diagnoses edge states and the interaction distance which measures the non-Gaussianity of a state. Their common trait is that they accept as exclusive input correlations of the state and search for particular patterns in them. For the monogamous edge states, the pattern one looks for is the high singular values of the correlation block of the covariance matrix, which are separated with a covariance gap from the rest. The interaction distance measures how accurately the free-fermion entanglement structure is satisfied by a given many-body entanglement spectrum. Since both the covariance matrix and the entanglement spectrum can be obtained for any state, these measures are straightforwardly applicable in a generic setting.

Chapter 4

Kitaev's Honeycomb Model

4.1 Introduction

Kitaev's honeycomb model is an interacting spin model, solvable through fermionisation [91, 92, 93, 94]. Its gapless phases are important in the context of quantum spin liquids [95]. In its gapped phases it supports topological order and one of them also supports a topological phase with non-trivial Chern number. This richness of behaviour renders it suitable for demonstrating the entanglement diagnostics we introduced in Chapter 3. We also analyse in detail its fermionic entanglement in gapped and gapless phases by reducing the problem to the study of 1D systems. Furthermore, we build effective models capturing the universal signatures. Our results supplement the conclusions we draw regarding monogamous edge states and the ground state's entanglement freedom.

4.2 The Model

Kitaev's honeycomb model [13] describes spin-1/2 degrees of freedom residing on the vertices $\Lambda_v^{\hexagon}$ of a hexagonal lattice $\Lambda^{\hexagon}$ subject to the Hamiltonian

$$H = \sum_{r=x,y,z} \sum_{\langle i,j \rangle} J_r \sigma_i^r \sigma_j^r + K \sum_{\langle\langle i,j,k \rangle\rangle} \sigma_i^x \sigma_j^y \sigma_k^z, \tag{4.1}$$

where $J_r > 0$ are nearest neighbour spin exchange couplings dependent on the link's orientation, r, and K is the magnitude of a three spin term which explicitly

breaks time reversal symmetry, as illustrated in Fig. 4.1.

Every hexagon hosts a $\mathbb{Z}_2$ valued six spin operator $W_{\hexagon} = \sigma^x\sigma^y\sigma^z\sigma^x\sigma^y\sigma^z$, with the σ^r ordered in a clockwise or anti-clockwise fashion around the hexagon, and is a symmetry of the Hamiltonian, $[H, W_{\hexagon}] = 0$. Thus the Hilbert space of the spin model thus breaks into sectors, which we refer to as *vortex sectors*, labeled by the $\mathbb{Z}_2$-eigenvalue patterns, $\{W_{\hexagon} = \pm\}$. The convention is that $W_{\hexagon} = -$ is a π-flux vortex in the hexagon. The ground state, $|\Psi\rangle$ lies in the no-vortex sector, $\{W_{\hexagon} = +\}$, as dictated by Lieb's theorem [96].

4.2.1 Exact Solution with Free Majoranas

In order to exactly solve the model, Kitaev then embeds the two-dimentional Hilbert space of each vertex to the four-dimensional Fock-space of two fermions. Each fermion is then broken down to two Majoranas and the dimensional redundancy is taken care of by projecting to the one parity-sector.

This is realised by substituting $\sigma_i^r = ib_i^r\gamma_i$, where b, γ are Majoranas, in the Hamiltonian, which as illustrated in Fig. 4.1 becomes

$$H = \frac{i}{2}\sum_{\langle ij\rangle} J_{ij}u_{ij}\gamma_i\gamma_j + \frac{i}{2}K\sum_{\langle\langle ij\rangle\rangle} u_{ik}u_{kj}\gamma_i\gamma_j, \tag{4.2}$$

where k is the connecting site between sites i and j and $J_{ij} = J_r$ depending on the orientation r of (i, j)-link. The operators $u_{ij} = ib_i^r b_j^r$ are interpreted as $\mathbb{Z}_2$-valued gauge fields living on the links, and are static in that they satisfy $[H, u_{ij}] = 0$.

The projection to the physical subspace of the model dictates that $D_i = ib_i^x b_i^y b_i^z c_i = 1$, where $[H, D_i] = 0$. It, however, anti-commutes with the three gauge fields sharing a vertex, thus acting as a local gauge transformation. The integrals of motion, $W_{\hexagon}$, are gauge-invariant and are written as

$$W_{\hexagon} = \prod_{(ij)\in\hexagon} u_{ij}. \tag{4.3}$$

Since both $W_{\hexagon}$ and u_{ij} are symmetries, by fixing a gauge in terms of a pattern $\{u = \pm\}$, a vortex sector $\{W_{\hexagon}\}$ is determined. There are exponentially many gauges corresponding to a vortex sector. Gauge-fixing turns (4.2) into a free Majorana Hamiltonian, in which case it models a p-wave superconductor. Each

vortex sector can then be in a gapless phase or a topological phase characterised by a Chern number [97, 98, 99]. We can reinterpret the gauge field by absorbing it into the J_{ij} hoppings thus allowing them to be negative. One can work with (4.2) and tune between vortex sectors by flipping signs of the J_{ij}s.

The state of a vortex sector $\{W_{\hexagon}\}$ is the gauge-symmetrisation

$$|\Psi\rangle_{\{W_{\hexagon}\}} \propto \sum_{\{u\}|\{W_{\hexagon}\}} |u\rangle \otimes |\gamma_u\rangle\,, \tag{4.4}$$

where γ_u is the gauge-invariant fermionic ground state for that sector and is found by diagonalising (4.2) for any $\{u\}$ that respects the chosen $\{W_{\hexagon}\}$. Kitaev also, independently from Lieb, numerically found that the ground state is $|\Psi\rangle_{\{+\}}$, to which there correspond $2^{|\Lambda_v^{\hexagon}|+1}$-many gauges.

4.3 Topological Phases and Topological Order

As is already established, each vortex sector is a free-Majorana system with some supporting a topological phase characterised by a Chern number $\nu \neq 0$.[20]. In the later sections we will analyse the entropic properties of Kitaev's model by building upon the work of Yao and Qi [100]. They found that the partial trace respects the tensor product structure of eigenstates of the form (4.7). Therefore the entanglement entropy is composed of two independent contributions

$$S = S_\gamma + S_u, \tag{4.5}$$

allowing us to study the entanglement of the topological phases supported in some vortex sectors separately from the entanglement of the gauge field which is responsible only for the topological order.

The fermionic contribution, S_γ, is due to only short-range entanglement and satisfies an area law. The free Majoranas are exclusively responsible a vortex sector's Chern number, given that that vortex sectors supports it a topological phase [20]. Their contribution is non-universal as the edge velocities can be tuned by the microscopic parameters J_{ij} and K [51]. However, S_γ is lower bounded by the topologically protected edge states that cannot be adiabatically removed without a phase transition. We capture this by our monogamy qualifier.

After the gauge symmetrisation (4.7) the gauge fields u_{ij} become fluctuating and give rise to an entanglement entropy S_u. It was shown that S_u contains both an area law and an constant reduction signalling the presence of topological order. The area law part is understood as the entanglement generated by sequential Hadamard gates on the b_i and b_j Majoranas which compose the u_{ij} lying on the links cut by the partition boundary, which are needed to rotate to another Majorana basis which is factorised across the cut [2, 100]. The topological entanglement entropy [52] takes the value $S_{\text{topo}} = \log 2$. It can be understood as a bit of information on the partition boundary storing knowledge about the boundary's parity.

In the following we will examine some important topological phases that arise in this model, and to this end, unless explicitly stated, we will be concerned with the fermionic part, S_γ, of the entanglement entropy, and we will drop the subscript. In any case, S_u is unaffected by the phase in which the Majoranas are.

4.4 Chain Decomposition and Phase Diagram

For convenience we deform the honeycomb into a brick-wall by setting the lattice vectors to $\mathbf{v}_x = (1, 0)$ and $\mathbf{v}_y = (0, 1)$, which only deforms the energy spectrum leaving the topological aspects invariant. We will study the no-vortex sector, which hosts a Chern number $|\nu| = 1$, and the full-vortex sector, $\{W_{\hexagon} = -\}$, characterised by $|\nu| = 2$. As argued in Ref. [20, 98], the $\nu = 2$ phase nucleates from the $\nu = 1$ phase due to anyon-anyon interactions, where the role of anyons is played by Majoranas trapped in the center of vortices. We set $|J_z| = 1$ and $|J_x| = |J_y| = J$ and by tuning $|J| \in (0, 1]$ we can induce a quantum phase transition to trivial phases with $\nu = 0$.

The gauge chosen for no-vortex is $\{u_{ij} = +\}$ and corresponds to the hoppings J_{ij}, K being positive along the arrows in Fig. 4.1. Full-vortex is realised by setting $u_{ij} = -$ on every other y-link along rows of the honeycomb, equivalent to flipping the sign of the J_y and overlapping K hoppings [101, 102] denoted by red in Fig. 4.1. Both sectors gap out upon letting $|K| > 0$. To implement the interpolation we multiply $\Theta_j = (1-\theta)+\theta(-1)^j$, where j enumerates z-links along

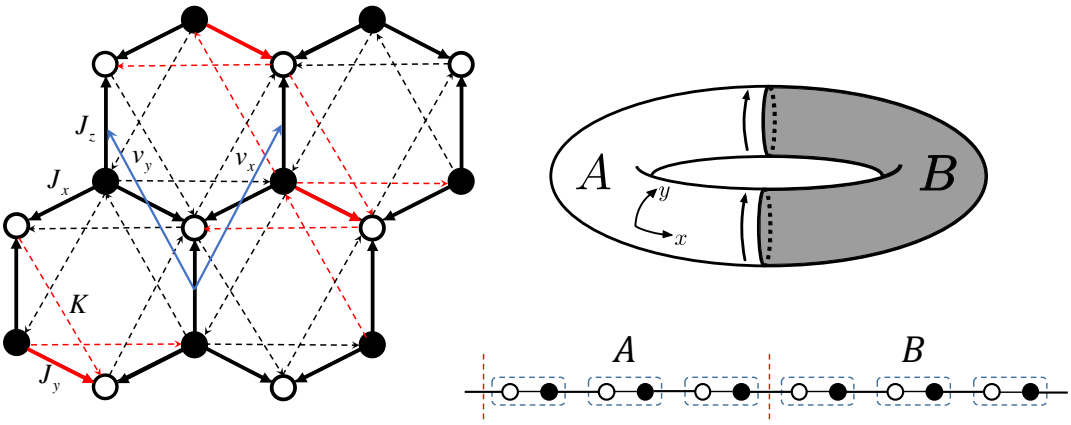

Figure 4.1: (Left) Anisotropic nearest neighbour couplings $J_{x,y,z}$ (solid) and chiral next nearest neighbour couplings K (dashed) with lattice vectors $\mathbf{v}_{x,y}$ (blue). Black and white discriminates between sublattices. The Majorana hoppings are chosen to be positive along the arrows. In red we denote the hoppings whose value is dictated by θ, enabling the interpolation between no-vortex and full-vortex. (Right)(Top) The partition boundary, ∂A, along which virtual edge states propagate (arrows), respects translation invariance along $\mathbf{v}_y$ and (Bottom) the partition boundary (red dashed) cuts between a p-chain's unit-cells (blue dashed).

$\mathbf{v_x}$. The parameter $\theta \in [0, 1]$ continuously flips the signs and allows interpolating between no-vortex for $\theta = 0$ and full-vortex for $\theta = 1$.

Lahtinen and Pachos [97, 99, 20, 98] mapped out the phase diagram over the no-vortex and full-vortex sectors and found that vortices bind localised Majorana modes and behave as anyons under braiding, which is realised by interpolating between vortex sectors and is implemented by adiabatic tuning of the couplings, J_{ij} [13, 102, 101].

The no-vortex sector ($\theta = 0$) hosts an achiral topologically trivial phase with $\nu = 0$ for $J < 1/2$. However it exhibits Abelian topological order as Kitaev showed that in this limit the model reproduces the toric code [29]. This is visualised by the honeycomb being deformed into a square lattice of strongly coupled dimers on each z-link behaving effectively as spins. For $J > 1/2$ the system is in a gapless spin-liquid phase for $K = 0$ and attains a gap for $|K| > 0$ realising a chiral topological phase with $\nu = \mathrm{sgn}(K)$. The topological order is non-Abelian and

the vortices behave as Ising anyons [13, 91]. In the full-vortex sector ($\theta = 1$), the toric code Abelian phase occurs for $J < \sqrt{\frac{1-K^2}{2}}$, while for $J > \sqrt{\frac{1-K^2}{2}}$ the system is in a chiral Abelian phase with $\nu = \mathrm{sgn}(K)2$ [20]. Note that in full-vortex the phase boundaries are K-dependent, contrary to no-vortex. Both chiral phases of no-vortex and full-vortex with $\nu \neq 0$ exist only for $K \neq 0$. For $K = 0$ time-symmetric gapless semi-metallic phases occur which can be interpreted as critical points between where the chirality flips manifesting as sign flipping of ν. Finally, for $J = 1$, where one can visualise the hexagons as being canonical, tuning between $|\nu| = 1$ no-vortex to the $\nu = |2|$ full-vortex by tuning θ we find that the quantum phase transition occurs at $\theta_c = \frac{3+K^2}{4}$ [99]. In Fig. 4.2 we show the bulk energy gap G vanishing at all of these critical points ($\nu_1 \leftrightarrow \nu_2$) between phases with Chern numbers $\nu_{1,2}$. The gap G is defined as explained in 2.2.1 for free Majoranas and is readily obtained from the eigenvalues of the hopping-pairing matrix corresponding to a vortex-sector for an instance of parameters J and K of the Hamiltonian (4.2). The phase transitions are also witnessed by the divergence of the fermionic entanglement entropy, S, which is given by (2.16).

Under the gauge choice imposed by Θ and parametrisation of the J_{ij}s, the Hamiltonian (4.2) can be written as

$$\begin{aligned} H = \ & \tfrac{i}{2}\textstyle\sum_{j,k} \quad J\left(\gamma^{\mathrm{b}}_{j,k}\gamma^{\mathrm{w}}_{j-1,k} + \Theta_j\gamma^{\mathrm{b}}_{j,k}\gamma^{\mathrm{w}}_{j,k-1}\right) + \gamma^{\mathrm{b}}_{j,k}\gamma^{\mathrm{w}}_{j,k} \\ & \quad +K\left(\Theta_j\gamma^{\mathrm{b}}_{j,k}\gamma^{\mathrm{b}}_{j+1,k-1} + \Theta_j\gamma^{\mathrm{b}}_{j,k}\gamma^{\mathrm{b}}_{j,k+1} + \gamma^{\mathrm{b}}_{j,k}\gamma^{\mathrm{b}}_{j-1,k}\right) \\ & \quad +K\left(\Theta_j\gamma^{\mathrm{w}}_{j,k}\gamma^{\mathrm{w}}_{j-1,k+1} + \Theta_j\gamma^{\mathrm{w}}_{j,k}\gamma^{\mathrm{w}}_{j,k-1} + \gamma^{\mathrm{w}}_{j,k}\gamma^{\mathrm{w}}_{j+1,k}\right) \\ & +\mathrm{h.c.}, \end{aligned} \tag{4.6}$$

where $\gamma^{\mathrm{b,w}}_{j,k}$ live on the black or white sublattice on the z-link with coordinates $(1 < j < L_x, 1 < k < L_y)$ in the $\mathbf{v}_{x,y}$ basis as illustrated in Figure 4.1. The parametrisation Θ_j respects translational invariance along $\mathbf{v}_y$ and a Fourier transform of the Majorana operators, $\gamma^{\mathrm{b,w}}_{j,k} = \sum_p e^{-ipk}\gamma^{\mathrm{b,w}}_{j,p}$, with $p \in [0, 2\pi)$ leads to

$$\begin{aligned} H(p) = \ & \tfrac{i}{2}\textstyle\sum_{j} \quad J\left(\gamma^{\mathrm{b}\dagger}_{\ j}\gamma^{\mathrm{w}}{}_{j-1} + \Theta_j e^{-ip}\gamma^{\mathrm{b}\dagger}_{\ j}\gamma^{\mathrm{w}}{}_{j}\right) + \gamma^{\mathrm{b}\dagger}_{\ j}\gamma^{\mathrm{w}}{}_{j} \\ & \quad +K\left(\Theta_j e^{-ip}\gamma^{\mathrm{b}\dagger}_{\ j}\gamma^{\mathrm{b}}{}_{j+1} + \Theta_j e^{ip}\gamma^{\mathrm{b}\dagger}_{\ j}\gamma^{\mathrm{b}}{}_{j} + \gamma^{\mathrm{b}\dagger}_{\ j}\gamma^{\mathrm{b}}{}_{j-1}\right) \\ & \quad +K\left(\Theta_j e^{ip}\gamma^{\mathrm{w}\dagger}_{\ j}\gamma^{\mathrm{w}}{}_{j-1} + \Theta_j e^{-ip}\gamma^{\mathrm{w}\dagger}_{\ j}\gamma^{\mathrm{w}}{}_{j} + \gamma^{\mathrm{w}\dagger}_{\ j}\gamma^{\mathrm{w}}{}_{j+1}\right) \\ & +\mathrm{h.c.}. \end{aligned} \tag{4.7}$$

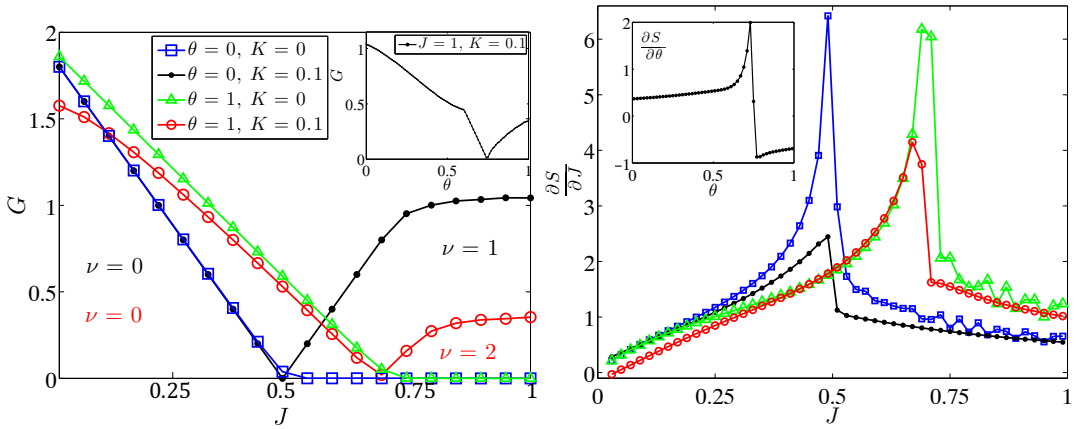

Figure 4.2: (Left) Energy gap G (defined in 2.2.1) in the no- ($\theta = 0$) and full-vortex ($\theta = 1$) sectors. For no-vortex the ($0 \leftrightarrow 1$) phase transition occurs at $J_c = 1/2$, while in full-vortex the ($0 \leftrightarrow 2$) transition takes place at $J_c = \sqrt{\frac{1-K^2}{2}}$. (Inset) ($1 \leftrightarrow 2$) occurs for staggered couplings corresponding to $\theta_c = \frac{3+K^2}{4}$. (Right) Divergence of the rate of change of S (given by (2.16)) correlates with the phase transitions. Here $L_x = L_y = 144$ in the main figures and $L_x = L_y = 100$ in the insets.

where the momentum index, p, of the fermionic operators $\gamma^{\mathrm{b,w}}_{j,p}$ is suppressed. An easy way to implement the Fourier transform such of quadratic Majorana Hamiltonians is to just give a momentum-phase to terms which describe hoppings outside the unit-cell, with the angle of the phase being the neighbouring degree of the hop, as can be see by comparing (4.6) and (4.7).

Note that apart from the time-symmetric momenta $p = 0, \pi$, each p-chain for $p \in (0, \pi) \cup (\pi, 2\pi)$ describes complex fermions. Furthermore, the condition $\gamma^\dagger_p = \gamma_{-p}$ implies that the truly independent chains are those for $p \in [0, \pi]$ as it is easy to confirm that $H(p) = H(-p)$. For independent systems the entropy, given by (2.16), is additive. The total fermionic entanglement entropy is $S = S(0) + S(\pi) + \sum_{p\in(0,\pi)} S(p)$ where the the first two terms are computed with a factor of $1/2$ reflecting the Majorana composition of the $0, \pi$-chains. This is equivalent to computing $S = \sum_{p\in[0,2\pi)} S(p)$ where all terms contain a $1/2$-factor.

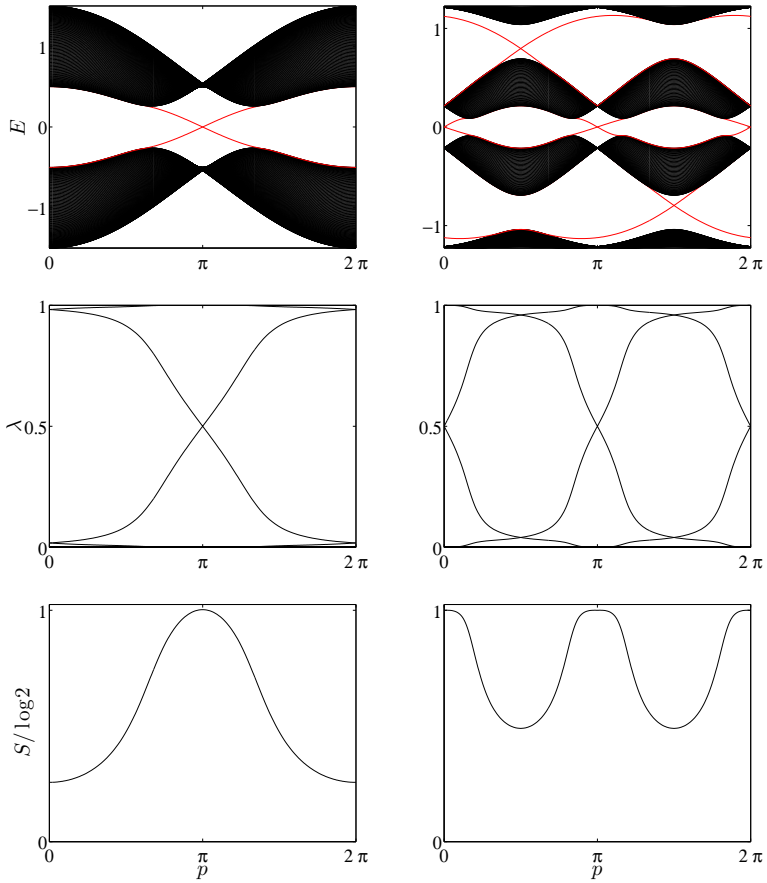

Figure 4.3: Energy spectrum $E(p)$, obtained as the spectrum of the hopping-pairing matrix of (4.7), on a cylinder and the corresponding the entanglement spectrum $\lambda(p)$, consisting of eigenvalues of the correlation matrix defined in 2.2.2, and the entanglement dispersion $S(p)$, given by (2.16), for the $\nu = 1$ (Left) and $\nu = 2$ (Right) phases. The real space edge states are indicated in red. Here $J = 1$ and $K = 0.1$. The bulk energy gap, $G = 2 \min_p |E(p)|$ is the minimal distance between the two bands (black), as a special case of its definition in 2.2.1.

4.5 Gapped Entanglement

In this section we dissect the entanglement in the gapped $|\nu| = 1$ and $|\nu| = 2$ topological phases of the honeycomb model, for the bipartition in Fig. 4.1. We make the approximation to decompose the fermionic entropy into S_{edge} due to edge states and to S_{bulk} due to bulk contributions

$$S \approx S_{\text{edge}} + S_{\text{bulk}}. \tag{4.8}$$

We focus on S_{edge} to study how it encodes the dominant part of the entanglement and relate it to universal signatures of the topological phases. We obtain an approximate expression for the S_{edge} that shows how it depends on the edge states' velocity, reproducing the results regarding the entropic lower bound in topological phases [7, 27]. We elaborate on the origin of this lower bound by showing that it arises from 1D subsystems of the full 2D model having completely decoupled Majorana modes which are topologically protected. Moreover, we construct a simple effective model that accurately approximates the total fermionic entropy. We then reinterpret the result via our monogamy qualifier.

4.5.1 Edge Velocity and Entropy

To study how the edge states contribute the dominant part of the fermionic entropy we first focus on the no-vortex sector at the $|\nu| = 1$ topological phase with a single Majorana edge state per edge. To connect these edge states to the entanglement entropy, we analytically evaluate their energy dispersion along the edge [103, 104, 105]. Here we sketch the calculation and refer to Appendix C.5 for details.

In the no-vortex sector, the p-chains in (4.7) can be written as

$$H(p) = \sum_j \chi_j^\dagger \mathcal{G}_1 \chi_j + \chi_j^\dagger \mathcal{G}_2 \chi_{j-1} + \chi_j^\dagger \mathcal{G}_2^\dagger \chi_{j+1}, \tag{4.9}$$

where $\chi_j^\dagger = \begin{bmatrix} \gamma_j^{\text{b}\dagger} & \gamma_j^{\text{w}\dagger} \end{bmatrix}$, $\mathcal{G}_1 = \begin{bmatrix} g_1 & g_2 \\ {g_2}^* & -g_1 \end{bmatrix}$, and $\mathcal{G}_2 = \begin{bmatrix} g_3 & g_4 \\ 0 & -g_3 \end{bmatrix}$, with $g_1 = -K \sin p$, $g_2 = \frac{i}{2}(Je^{-ip} + 1)$, $g_3 = \frac{i}{2}K(1 - e^{ip})$, and $g_4 = \frac{i}{2}J$. We express the edge state as $\Psi = \sum_{j=1}^{\infty} \chi_j^\dagger \Psi_j \left|0\right\rangle$ with $\Psi_j = \begin{bmatrix} \Psi_j^1 & \Psi_j^2 \end{bmatrix}^T$.

Placing the system on a semi-infinite cylinder with circumference along $\mathbf{v}_y$, the Schrödinger equation $H(p)\Psi = E\Psi$ leads to the following recursive equation

$$\mathcal{G}_2\Psi_{j-1} + (\mathcal{G}_1 - E)\Psi_j + \mathcal{G}_2^\dagger\Psi_{j+1} = 0, \tag{4.10}$$

and imposing semi-infinite boundary conditions such that the cylinder is open at $j = 1$ and extends to $j \to +\infty$ we have $(\mathcal{G}_1 - E)\Psi_1 + \mathcal{G}_2^\dagger\Psi_2 = 0$. Multiplying (4.10) by $z^j \in \mathbb{C}$, summing over j, definining the generating function $G(z) = \sum_{j=1}^{\infty} z^{j-1}\Psi_j$, we obtain

$$G(z) = \left(z^2\mathcal{G}_2 + z(\mathcal{G}_1 - E) + \mathcal{G}_2^\dagger\right)^{-1}\mathcal{G}_2^\dagger\Psi_1. \tag{4.11}$$

The energy dispersion $E(p)$ can be obtained from an analysis of the poles of $G(z)$. In general an edge mode exists at the ends of a p-chain if the all the poles lie outside of the unit circle [103]. Imposing this condition leads to a system of constraints allowing us to solve for the energy dispersion $E_\pm(p)$ as a function of the microscopic parameters J, K, with the $\pm$ subscript indicating the right- and left-moving edge mode that can be localised on that edge. If the system is placed on a finite cylinder, one boundary hosts an edge mode with E_+ and the other with E_-. Linearising its expression around the momentum where the zero energy occurs, $p^\star = \pi$ as shown in Fig. 4.3, we get

$$E_\pm = \pm v_E(p - \pi) + \dots \quad , \qquad v_E = (2J + 1)\cos\tan^{-1}\left(\frac{J}{4K}\right) \tag{4.12}$$

This analytic expression for the velocity is valid in the momentum range Δp where the pole conditions for the edge states' existence are satisfied (see App and App of Ref. [106]). The range Δp is determined numerically by tracking the behaviour of the poles of $G(z)$ as J, K are varied. We find that Δp coincides accurately with the distance between the Fermi momenta, between which the edge states exist.

After obtaining this expression for the velocity of the edge states, v_E we want to relate it to the velocity of the virtual edge states, v_λ, appearing in the entanglement spectrum. We recall that the energy spectrum with open boundaries and the entanglement spectrum for periodic boundaries are adiabatically connected [7], i.e. the latter is a band-flattened version of the former. Furthermore,

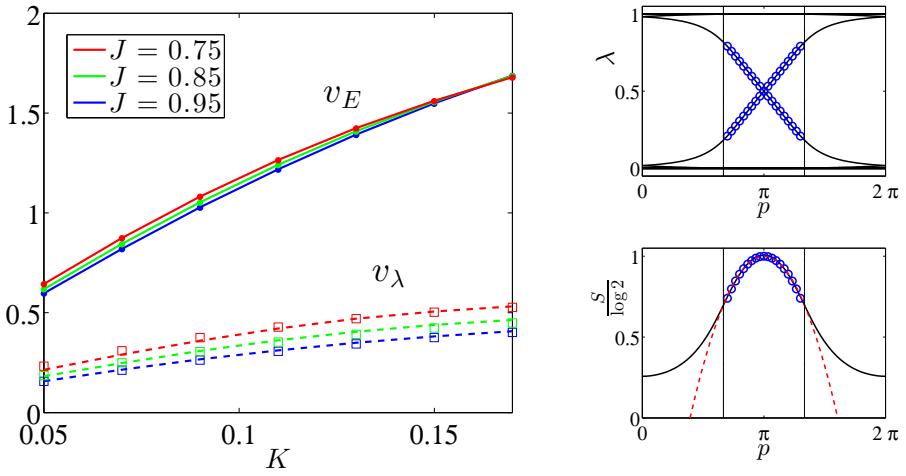

Figure 4.4: (Left) The correspondence between the physical velocities v_E and the virtual velocities v_λ. The analytic expression (solid line) given by (4.12) for the physical velocities agrees with the numerical values (dots). Via the ansatz (4.13) (dashed line) it reproduces the numerically obtained virtual velocities (squares).Numerically the velocities are obtained by a linear fit at $p = \pi$. Entanglement spectrum (Top) and entropy (Bottom) in the momentum interval Δp (between vertical lines) in the no-vortex ($\theta = 0$) sector with $J = 1$ and $K = 0.12$. A linear approximation $\lambda^{\pm}$ with velocity v_λ obtained form (4.13) contributes almost all of the entropy inside Δp (blue circles). The analytic expression (4.15) (red dashed) as a quadratic approximation to $S_{\text{edge}}(p)$ reproduces the entropy within accuracy of 0.1% inside Δp.

since both velocities are the slopes of the edge state as it crosses the $p^\star$ momentum it is reasonable to relate them with a proportionality constant,

$$v_\lambda \approx \kappa v_E. \tag{4.13}$$

To obtain an ansatz for κ, we first assume that the energy spectrum is flattened around its half-bandwidth energy at $p^\star$ and the energy of this band is rescaled to unity. Subsequently, we center the entanglement spectrum around zero and rescale it as $\lambda \to 2(\lambda - \frac{1}{2})$ such that every entanglement level takes values between ± 1. This leads to the ansatz $\kappa = (2G(p^\star) + W(p^\star))^{-1}$, where $G(p^\star)$ and $W(p^\star)$ are

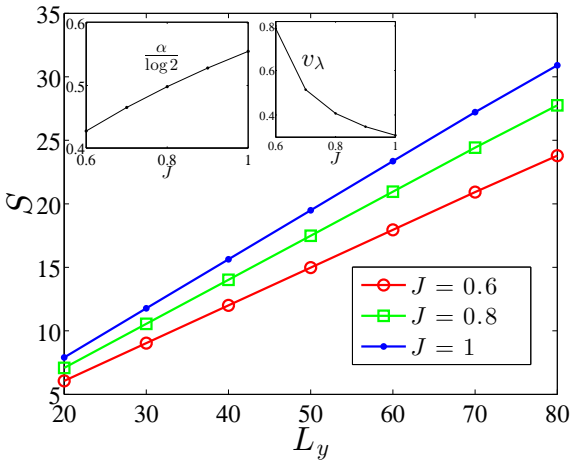

Figure 4.5: Area law $S = \alpha L_y$ obeyed by total entropy (see (2.16)) for cut-lengths L_y large enough so that there are no finite size effects. The area law coefficient, α, which is obtained by just dividing S by L_y and is upper bounded by $\log 2$, increases as the virtual velocity v_λ (see (4.13)) decreases as a function of J (Insets). Here $K = 0.12$.

the energy gap and the bandwidth at $p^\star$, respectively. In Fig. 4.4 we demonstrate that this phenomenological ansatz provides a good approximation of v_λ for a wide range of couplings J and K.

The entanglement spectrum can then be approximated by the linearized expression around $p^\star$

$$\lambda_\pm(p) = \pm v_\lambda p + \frac{1}{2}, \quad p \in \Delta p. \tag{4.14}$$

Inserting this into (2.16) and expanding around $p^\star$, the dominant entropy contributions can then be approximated by

$$S_{\text{edge}}(p) \approx \log 2 - 2v_\lambda^2 p^2 + \mathcal{O}(p^4). \tag{4.15}$$

In Fig. 4.4 we show that this expression provides an excellent approximation of the entropy within the momentum interval Δp where the virtual velocity is accurately obtained from the physical velocity of the edge states via the phenomenological ansatz.

Our analysis, although simple, it demonstrates general properties of the entanglement, quantified by the entropy, for systems that host topologically protected edge states. The inability to remove the edge states without a phase transition implies the existence of at least one $p^\star$ momentum. As the velocity of the edge traversing the gap at $p^\star$ can be made arbitrarily large, $v_\lambda \to \infty$, by tuning the microscopics of the model without inducing a phase transition [51], the total entropy has a theoretical lower bound of $\log 2$, consistent with earlier studies [7, 27].

Furthermore, the contribution by each momentum p is upper bounded by $\log 2$ for these gapped phases, as the bulk can be adiabatically made to contribute no entropy and the maximal contribution from a pair of Majorana edge modes is $\log 2$ with the contribution decreasing with increasing velocity v_λ. As the perimeter of the cut ∂A is directly proportional to the momentum range Δp, this means that the area law contribution $S \sim \alpha|\partial A|$ should be smaller when the velocity increases. Indeed, Fig. 4.5 shows that as the microscopic parameters are tuned to give smaller velocities, the entanglement entropy grows faster with increasing of the cut length $|\partial A|$, i.e. the area law coefficient α increases.

4.5.2 Reinterpretations of the Entropic Lower Bound

As the entanglement entropy in the gapped phases is lower bound by irremovable $\log 2$-contributions of the edge states at momenta $p^\star$, we proceed to investigate its origin in the no-vortex sector for which $p^\star = \pi$. Focusing on the $p^\star$-chain we examine the zero-dimensional edge states it hosts. Finally, we construct a four-Majorana toy model for the edge entanglement of the 2D model and reinterpret the result in terms of our entanglement monogamy qualifier.

Lower Bound from Kitaev's Chain

To this end we focus first on the 1D wire corresponding to the only crossing point of the edge states at $p^\star = \pi$ in the vortex free sector, as shown in Fig. 4.3. For $\theta = 0$ the general Hamiltonian (4.7) takes the simple form

$$H(\pi) = i\sum_j \left((1-J)\gamma_j^{\mathrm{b}}\gamma_j^{\mathrm{w}} + J\gamma_j^{\mathrm{b}}\gamma_{j-1}^{\mathrm{w}} + \mathrm{h.c.}\right) + K(\gamma_j^{\mathrm{b}}\gamma_{j-1}^{\mathrm{b}} - \gamma_j^{\mathrm{w}}\gamma_{j-1}^{\mathrm{w}}), \quad (4.16)$$

where $\gamma^{\mathrm{b,w}}$ are Majoranas due to $p^\star$ being a time-symmetric momentum point.

We suspect and confirm that $H(p^\star)$ is mappable to Kitaev's superconducting wire whose Hamiltonian is

$$H = -\frac{1}{2}\sum_j \mu n_j + (t f_j^\dagger f_{j+1} + \Delta e^{i\phi} f_j f_{j+1} + \mathrm{h.c}), \quad (4.17)$$

where $n_j = f_j^\dagger f_j$ the on-site occupation of the fermions. The phase is quite simple. For $|t| < |\mu|$ it is a trivial insulator with $w = 0$ winding number and

for $|t| > |\mu|$ it obtains a winding number $|w| = 1$ which manifests as a strong zero-mode [56] for open boundary conditions. These unpaired Majoranas at the edges of the chain lead to a doubly-degenerate energy spectrum, with degeneracy exponentially decreasing as a function of the chain's length.

Upon decomposition $f_j = \frac{1}{2}(\gamma_j^{\mathrm{b}} + i\gamma_j^{\mathrm{w}})$ of the complex fermions into Majoranas

$$\begin{aligned} H = \; i\sum_j \; & \left(\frac{\mu}{2}\gamma_j^{\mathrm{b}}\gamma_j^{\mathrm{w}} + \frac{t+\mathrm{Re}(\Delta)}{4}\gamma_j^{\mathrm{b}}\gamma_{j-1}^{\mathrm{w}} + \frac{t-\mathrm{Re}(\Delta)}{4}\gamma_j^{\mathrm{b}}\gamma_{j+1}^{\mathrm{w}} + \mathrm{h.c.} \right) \\ & + \frac{\mathrm{Im}(\Delta)}{4}\left(-\gamma_j^{\mathrm{b}}\gamma_{j-1}^{\mathrm{b}} + \gamma_j^{\mathrm{w}}\gamma_{j-1}^{\mathrm{w}}\right), \end{aligned} \tag{4.18}$$

where $\mathrm{Re}(\Delta) = \Delta\cos\phi$ and $\mathrm{Im}(\Delta) = \Delta\sin\phi$. Setting $t = \mathrm{Re}(\Delta)$ to kill the third term we can read off the corresponding couplings $\mu = 2\,(1-J)$, $\mathrm{Re}(\Delta) = 2J$ and $\mathrm{Im}(\Delta) = -4K$. The topological phase of Kitaev's chain occurs for $|t| > |\mu|$ corresponding exactly to the parameter range of the no-vortex sector of the honeycomb model, $J > 1/2$.

Then the entropic lower bound of the gapped no-vortex sector is understood as follows. Let's take the $J = 1$ case where the hopping in the black-white unit-cell vanishes and the majoranas at the end of the chain completely decouple. When the wire with periodic boundary conditions is partitioned into A and B, we are cutting through two $\gamma_j^{\mathrm{w}} - \gamma_j^{\mathrm{b}}$ Majorana dimers, one per ∂A-component. Each dimer can be fused to a complex fermionic mode which can be occupied or not. Tracing out one of the Majoranas of each dimer makes the parity of the combined occupations of the fermionic modes uncertain since each fermion needs both of its Majoranas in order to know its occupation. Thus we lose one bit of information corresponding to even versus odd parity giving rise to a $\log 2$ entropy, which can be viewed as $2\log\sqrt{2}$ where $\sqrt{2}$ is the quantum dimension of a Majorana, leading to $S \geq 2\log\sqrt{2}$. Following then the same argument for the full-vortex sector, we interpret the origin of its entropic lower bound, $S \geq 4\log\sqrt{2}$ as the $2\log\sqrt{2}$ from each of its $p^\star$-chains that host zero modes at their ends.

Toy Model for Edge Entanglement

We now construct an effective model, for the entropy of the no-vortex sector, comprising four Majoranas representing the virtual edge states on either side of

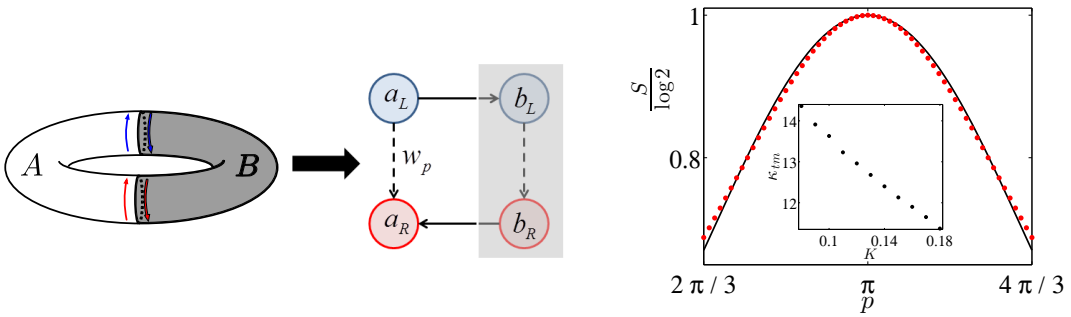

Figure 4.6: (Left) Toy model for the entropy S. Partitioning the system on a torus into A, B gives rise to virtual edge states on either side of the cut which we treat as 0D Majorana modes a_L and a_R living on the edges of A and b_L and b_R living on the edges of B. They hybridize according to the effective Hamiltonian (4.19), where the solid arrows correspond to strong hopping set to unity and weak to w_p. (Right) Entropy $S_{\rm tm}$ (red dots) between the Fermi points obtained from the effective model reproduces accurately the entropy S (black line) of the $\nu = 1$ phase of the honeycomb model. Here $L_x = 24, L_y = 60$, $K = 0.125$. (Inset) The value of the optimized proportionality constant $\kappa_{\rm tm}$ as the function of K.

the entanglement cut on a torus. The two virtual Majorana edge modes a_L and a_R that appear at the boundary of the cylindrical region A are entangled with their counterparts b_L and b_R in B as shown in Fig. 4.6. The motivating question is how much of the total entropy can be attributed to the edge states alone. The toy model Hamiltonian is

$$H = i(a_L b_L - a_R b_R) + i w_p (a_L a_R + b_L b_R), \tag{4.19}$$

where the signs are chosen such that a π-flux threads the chain, the inter-partition hopping is set to unity and the intra-partition hopping to w_p.

Since the we have fixed the hopping across the cut arbitrarily, we define $w_p = \kappa_{\rm tm}|E_\pm(p)|$, where $\kappa_{\rm tm}$ is a proportionality constant to be determined. The connection with the no-vortex sector is made by the use of its edge dispersion relation $E_\pm(p)$. The intuitive justification for the use of $E_\pm(p)$ is as follows. We know that at $p^\star$ the edge states of that $p^\star$-chain for open boundaries are completely decoupled from the bulk so that $E_\pm(p^\star) = 0$ and as we move away from

that momentum the edge states of that p-chain start penetrating into the bulk obtaining a finite energy $E_{\pm}(p^{\star}) > 0$ due to their hybridisation. We interpret their overlap through the bulk as an effective hopping between them, and after adopting the same intuition for the virtual edge states by viewing each partition as an effectively open chain, we arrive at the proposed form of w_p. Of course, at $p^{\star}$ we have $w_p = 0$ and the model is reduced to two Majorana dimers which are cut in half by ∂A and we recover the entropic lower bound.

The entanglement entropy $S_{\text{tm}}(w_p)$ of such a small system can be obtained analytically (see Appendix C.6) by computing by tracing out the Majoranas b_L and b_R in B, as shown in Fig. 4.6, and is given by

$$S_{\text{tm}}(w_p) = \frac{1}{1+s^2}(-2s^2 \log s + (1+s^2)\log(1+s^2)), \tag{4.20}$$

where $s = -\frac{w_p - \sqrt{w_p^2+4}}{2}$. To compare this expression with S obtained from the no-vortex sector, we optimise the proportionality constant κ_{tm} such that $\frac{|S - S_{\text{tm}}|}{S} < 1\%$ in the momentum interval Δp. In Fig. 4.6 we show that S_{tm} accurately approximates S_{edge} demonstrating that the behaviour of the entropy of the edge states dominates that of the total entropy of the model.

Monogamy and its Robustness

We can reinterpret the entropic behaviour of the virtual edge states in terms of entanglement monogamy. For the no-vortex and full-vortex sectors placed on a torus where regions A, B are cylindrical, since there is maximal entanglement across the cut from the $p^{\star}$-chains, which also gives rise to the lower bound of the total fermionic entropy, the virtual edge states have to be decoupled from their corresponding A, B-bulks and contribute maximal singular values to the off-diagonal block of the covariance matrix, Γ_{AB}. We capture the signatures of these highly entangled monogamous Majorana pairs with our qualifier $\mathcal{S}_q$. The convergence of the qualifier to the number, $\mathcal{S}_{\infty}$, of such pairs is shown in Fig. 4.7 and is consistent with the dimensionality of the edge states.

Moreover, we know that the entropy is lower bounded as $S \geq \text{tr}\Gamma_{AB}^2 \log\sqrt{2}$, where $\text{tr}\Gamma_{AB}^2$ is the sum of the squared singular values. Furthermore, the only singular values that cannot be adiabatically removed are those $\xi^{AB} = 1$ due to

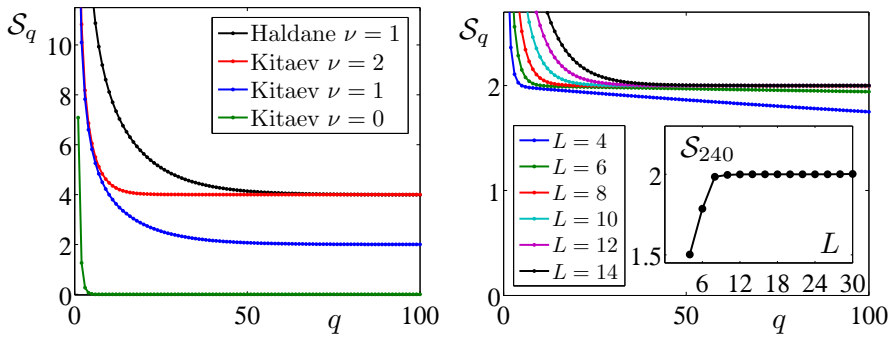

Figure 4.7: (Left) Convergence of qualifier $\mathcal{S}_q$ (given in (3.12)) for the Kitaev and Haldane models. For Kitaev's model we find $\mathcal{S}_{q\to\infty} \to 2\nu$ consistent with each phase and for Haldane's model we have $\mathcal{S}_{q\to\infty} \to 4\nu$ as a Dirac mode corresponds to two Majorana modes. Here $J = 1$ for the topological and $J = 0.35$ for the trivial phases respectively for the Kitaev model, with $K = 0.15$ and $L_x = L_y = 16$. For Haldane $t_1 = 1$, $t_2 = 1/3$, $\phi = \pi/3$, and $L_x = L_y = 12$. (Right) System size $L = L_x = L_y$ dependence of $\mathcal{S}_q$ for no-vortex Kitaev with $\nu = 1$, in the presence of disorder of amplitude $\Delta = 0.5$. Here $J = 0.8$, $K = 0.15$. The data is averaged over 50 disorder realisations.

the topologically protected edge states and their number is equal to $\mathcal{S}_\infty$. Thus the entropic lower bound is $S \geq 2 \log \sqrt{2}$.

Topological phases are robust against local disorder in the form of randomness in the hoppings $J_{i,j}, K$. Disorder is introduced as $J^{\alpha}_{\mathrm{d}\,i,j} = J^{\alpha}{}_{i,j}(1 + \delta J_{i,j})$, where $\delta J_{i,j}$ is drawn uniformly from $|\delta J_{i,j}| \leq \Delta$. The couplings K are randomised similarly as $K_{\mathrm{d}i,j} = K(1 + \delta K_{i,j})$, where $\delta K_{i,j}$ with $|\delta K_{i,j}| \leq \Delta^2$. As long as the disorder amplitude is low compared to the energy gap G, the phase is stable and no quantum phase transition occurs. Thus we expect that as long as $\langle G \rangle_\Delta > 0$ then $\langle \mathcal{S}_{q\gg 1} \rangle_\Delta$ is almost quantised and equal to the number $\mathcal{S}_\infty$ of maximally entangled Majorana pairs. The average is taken over disorder realisations of amplitude Δ. We demonstrate the robustness in Fig. 4.8 (Right). Disorder causes the the maximal singular values of Γ_{AB} to decrease slightly from the exact values 1, an effect which can be compensated against by growing the system size, and so it suffices to tune q to a finite value so that the phase diagram can be identified. The existence of the topological phases for the gapped cases shown in

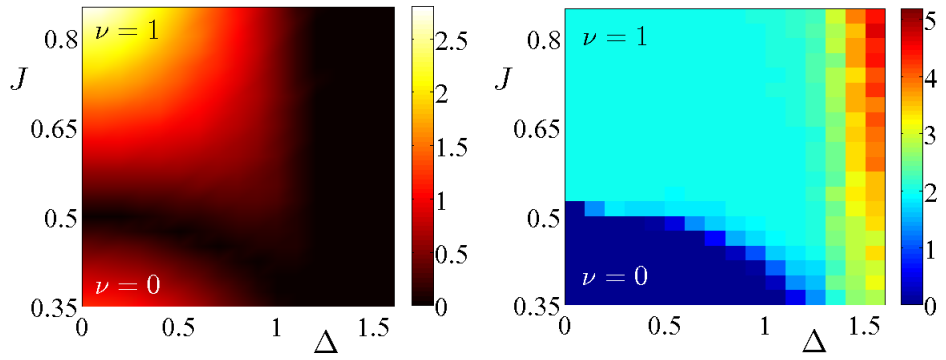

Figure 4.8: (Left) Energy gap for the disordered no-vortex sector of Kitaev's model as a function of the coupling J and the disorder Δ. The topological phases with $\nu = 0$ and $\nu = 1$ are separated by a phase transition at $J_c = 0.5$ for $\Delta = 0$. The data is for $L_x = L_y = 30$ averaged over 50 disorder realisations of J and K. (Right) The same phase diagram diagnosed by $\mathcal{S}_q$ showing extended regions where $\mathcal{S}_{240} = 2|\nu|$ identifies the topological phases even for strong disorder. The non-quantized behaviour for $\Delta > 1$ identifies the thermal metal phase

Fig. 4.8 (Left) can be also verified by computing the Chern number ν in real-space from the Majorana-Majorana correlation matrix C_{ij} as defined in (2.14), which is also averaged over disorder realisations and converges to a quantised value as the system size as well as the partitions A, B, C used to compute it incerease [20].

In Appendix C.7 we provide details regarding finite size effects in the presence of disorder. We also make a connection between the effect of disorder and of finite temperature, $T > 0$, in the no-vortex sector, since they both drive the system into a thermal metal when either the Δ or T are comparable to the energy gap. [107, 108]. The thermal metal occurs when disorder or temperature create spurious vortices which after arriving at a critical density close the energy gap turning the system into a metal. In Appendix C.8 we describe how the the covariance matrix is obtained at $T > 0$ with the insertion of Boltzmann weights in the occupations of the two-level systems that make up the model as is performed by Self in Ref. [109], and we present numerical results supporting this connection.

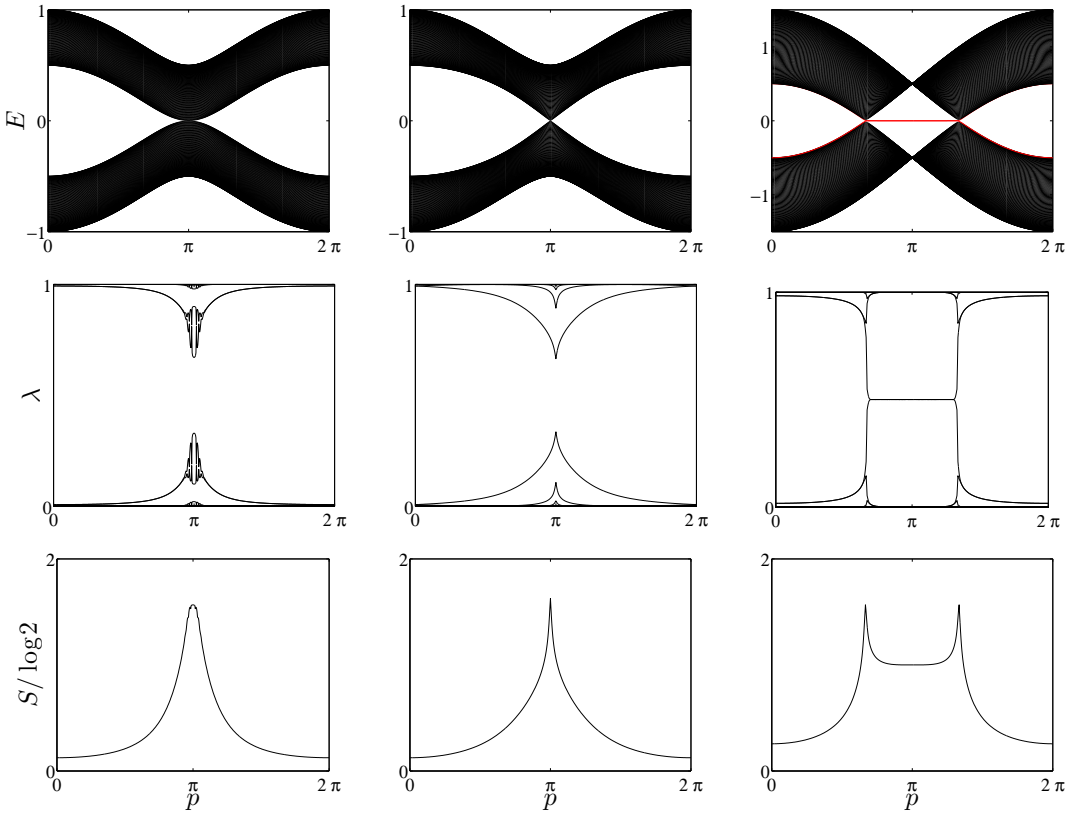

Figure 4.9: Energy, entanglement spectrum and entropy for gapless phases and criticalities of no-vortex ($\theta = 0$). (Left) Tricriticality ($\nu = 0 \leftrightarrow \pm 1$ at $J = \frac{1}{2}$, $K = 0$ which becomes (Middle) a $(0 \leftrightarrow 1)$ criticality for $K = 0.1$. (Right) Gapless phase, or $(-1 \leftrightarrow 1)$ criticality, at $J = 1$, $K = 0$.

4.6 Gapless and Critical Entanglement

We now study the entanglement, again for the bipartition of Fig. 4.1, in the gapless (semimetallic) phases and criticalities related to the no-vortex and full-vortex sectors again from the viewpoint of the p-chain decomposition. For a quantum critical point between two topological phases with Chern numbers $\nu_{1,2}$ we denote the criticality $(\nu_1 \leftrightarrow \nu_2)$. Representative band structures as well as entanglement spectra and entropies are shown in Fig. 4.9, Fig. 4.10, and Fig. 4.11.

For a vanishing energy gap $G(p_c) = 0$ the correlation length along chains located at critical momenta, p_c, diverges. In 1D quantum systems second-order

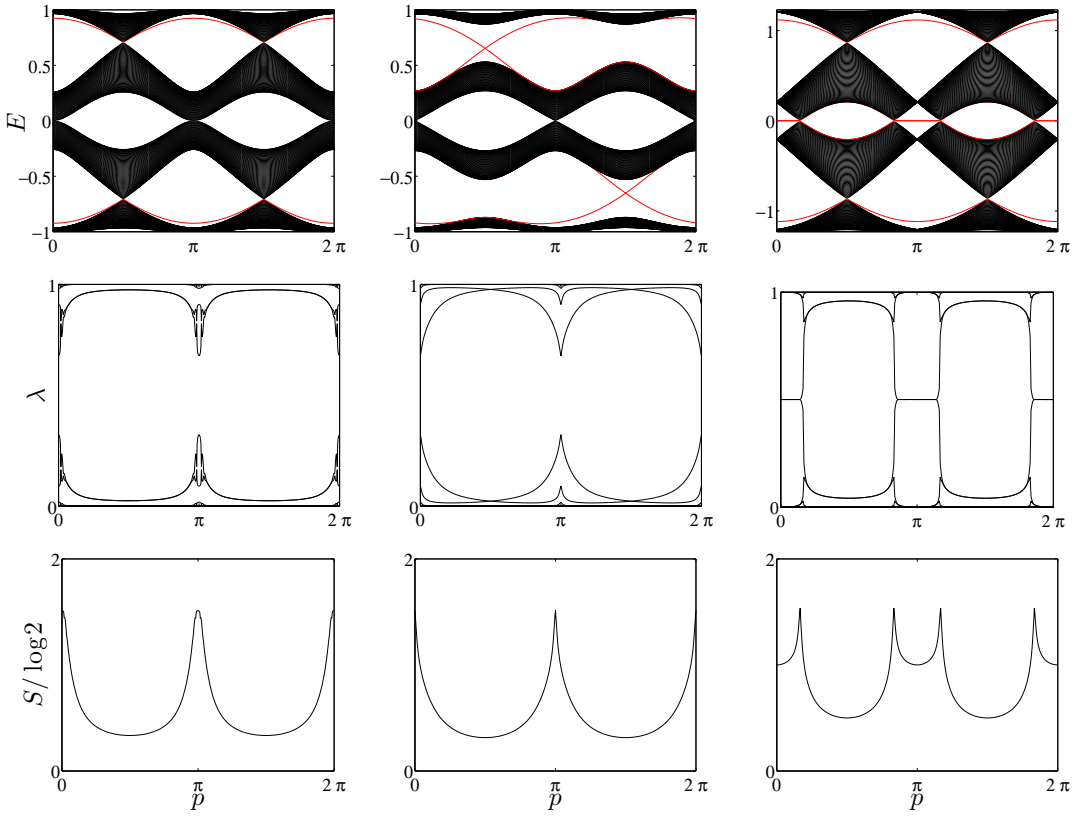

Figure 4.10: Energy, entanglement spectrum and entropy for gapless phases and criticalities of full-vortex ($\theta = 1$). (Left) Tricriticality ($\nu = 0 \leftrightarrow \pm 2$) at $J = \frac{1}{\sqrt{2}}$, $K = 0$ which becomes (Middle) a $(0 \leftrightarrow 2)$ criticality $K = 0.1$ with K dependent boundary at $J = \sqrt{\frac{1-4K^2}{2}}$. (Right) Gapless phase, or $(-2 \leftrightarrow 2)$ criticality, at $J = 1$, $K = 0$.

phase transitions with linearly dispersing gapless excitations are described by conformal field theory (CFT) capturing the universal behaviour of all correlations functions [110]. In this context, the entropy, S_c, of a line segment of length x violates the area law and follows the Cardy-Calabrese scaling [111]. Moreover, the chains around the Fermi points for momenta such that $|p - p_c| \ll \pi$, are gapped, with however the gap being so small so that they deserve to be called "quasicritical". It is known that their entropy, S_c, obeys the area law [111, 10].

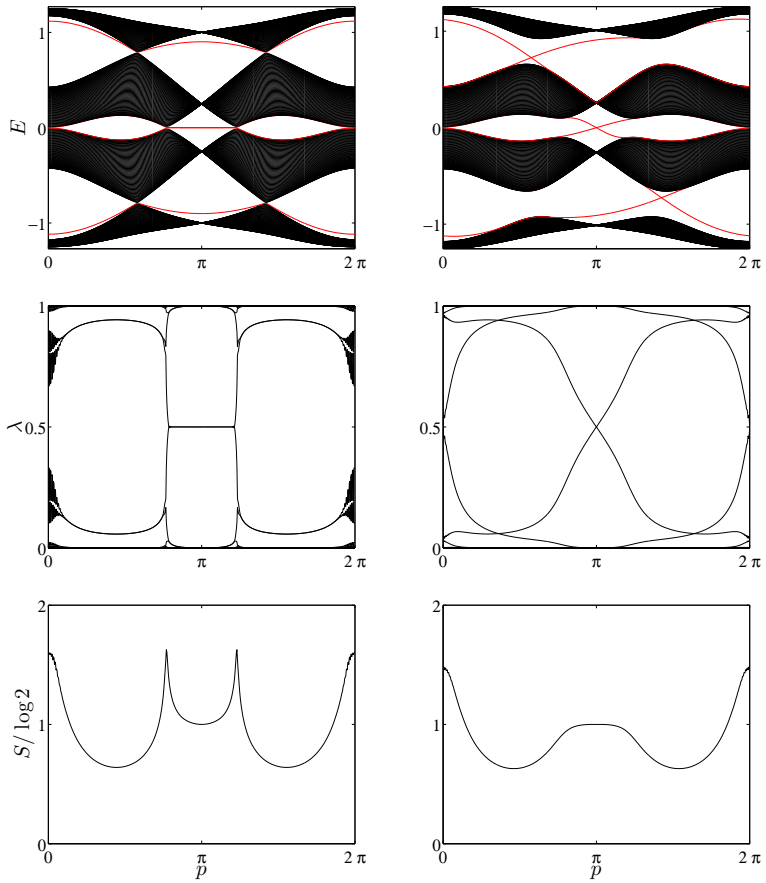

Figure 4.11: Energy, entanglement spectrum and entropy for criticality between no-vortex and full-vortex occuring at $\theta = \frac{3+4K^2}{4}$ for $K = 0$ (Left) and $K = 0.1$ (Right). Here $J = 1$.

These two cases are given by

$$S_{\mathrm{c}} = \frac{c}{3}\log\left(\frac{L_x}{\pi}\sin\frac{x\pi}{L_x}\right) + \text{const.}, \quad S_{\mathrm{qc}} = \frac{c}{3}\log\xi + \text{const.}, \tag{4.21}$$

where c is the central charge of the conformal field theory that describes the criticality, L_x is the chain's length, and $\xi(p) \approx 1/G(p)$ is the correlation length. Finally, for the p-chains between Fermi points, exact zero modes occur. We treat those chains as in the previous section 4.5 as the zero modes contribute a $\log 2$ to the entropy and their bulk's contribution can be considered negligible, in accord with (4.15). They compose non-dispersing edge states connecting the

Fermi points which are located at the tips of local cones formed the nodal points of the band structure as displayed in Fig. 4.9 and Fig. 4.10. We thus write the total fermionic entanglement entropy as

$$S \approx S_{\mathrm{c}} + S_{\mathrm{qc}} + S_{\mathrm{edge}}, \tag{4.22}$$

where S_{c} is the contribution from critical chains at the Fermi points, S_{qc} contains the quasi-critical contributions with long correlation lengths and S_{edge} symbolises the contribution of the chains hosting zero-modes.

4.6.1 Entropic Lower Bound

As we interpreted the entropic lower bound for the gapped topological phases to be stemming from Majorana zero modes localised at the ends of the $p^\star$-chains, the same analysis holds for the gapless phases ($K = 0$).

Let's take the the isotropic case with $J = 1$. For the no-vortex sector, notice that the phase diagram of the π-chain given by (4.18) is K-independent since the gauge freedom in ϕ allows us to remove Δ_I. Thus this wire exhibits also a topological phase with Majorana edge states for $K = 0$, consistent with Fig. 4.9 showing a flat band of edge states between the Fermi points. The cones however move towards each other by deforming the honeycomb [99] by taking $J < 1$ and thus the collection of zero-modes between the Fermi points can shrink. On the other hand, the π-chain's edge states are topologically protected by its winding number and hence can not be adiabatically removed,[112]. Therefore, the total entropy of the gapless phase of the no-vortex sector satisfies $S \geq 2 \log \sqrt{2}$.

Similarly, for the full-vortex sector,at $p^\star = 0$ the Hamiltonian is K-independent leading to one decoupled Majorana at each edge of the chain exactly as in the no-vortex case. For $p = \pi$ the Hamiltonian has three decoupled Majoranas at its edges, one of the completely decoupled and the other two coupled together. The two coupled Majoranas form a gapped fermion consistent with the finite energy edge state observed in Fig. 4.10. Following then the same argument as for no-vortex, the the lower bound to the entropy of the full-vortex sector is $S \geq 4 \log \sqrt{2}$.

4.6.2 Central Charge of Critical Chains

The critical momenta p_c at which the bulk gap closes, $G(p) = 0$, for the gapless phases and critical points examined here can be obtained exactly from the analytic form of the energy gap along both momentum directions $G(q, p)$ which is presented in Appendix C.2.

In the previous section we saw that in the gapped topological phases edge states give rise to gapless entanglement spectra. At critical points, however, the entanglement spectra are gapped and exhibit nesting of entanglement levels in the vicinity of the critical momenta p_c (see Fig. 4.9 (Left,Middle), Fig. 4.10 (Left,Middle), and (see Fig. 4.11 (momentum $p_c = 0$)). Correlations in critical chains obey a power law decay and this is responsible for the critical entanglement scaling. Since power law correlations imply the lack of a characteristic length scale, the correlations inherit a self-similar structure. Note, this is not the case for the gapless phases, which are the $K \to 0$ limit of topological phases (see Fig. 4.9 (Right), Fig. 4.10 (Right)).

By growing a linear partition on the p_c-chains we extract their central charge which appears as the proportionality factor in scaling of the entropy with the partition's chord length as in (4.21). We present our linear fits in Fig. 4.13 and we find that all scale with $c = 1/2$ consistent with linearly dispersing fermions [110]. Based on Refs [113, 114, 115], Lahtinen argues in Ref [106] that we can understand the value of the central charge in terms of the CFT that characterises the critical chains of gapless and critical points of the honeycomb model. This in turn characterises the 2D model's universality class.

More specifically, the gapless phase ($K = 0$) in the vortex free sector the single independent critical chain corresponding to the critical momenta p_c is given by

$$H(p_c) = \frac{i}{2} \sum_j J {\gamma^{\mathrm{b}\dagger}}_j {\gamma^{\mathrm{w}}}_{j-1} + \left(1 + Je^{-ip_c}\right) {\gamma^{\mathrm{b}\dagger}}_j {\gamma^{\mathrm{w}}}_j + \text{h.c.}, \tag{4.23}$$

describing free fermions on a staggered chain. At the honeycomb's critical point, $J = \frac{1}{2}$, where it transitions to the gapped $\nu = 0$ phase, there critical momentum is $p_c = \pi$ where the chain describes Majoranas on a staggered chain which is simply Kitaev's wire [116]. It and has a phase transition at $J = \frac{1}{2}$ where the winding number changes from $|\nu| = 1$ ($J > \frac{1}{2}$) to $\nu = 0$. The low energy theory

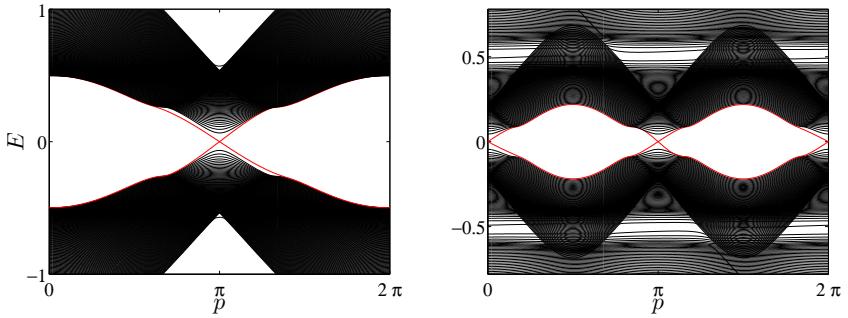

Figure 4.12: Real space phase transition induced by a varying $J = \sin(\frac{\pi x}{2L_x})$, where x is the $\mathbf{v}_x$ coordinate. Edge states (red) appear at the x for which $J = \frac{1}{2}$ for no-vortex and $J = \sqrt{\frac{1-4K^2}{2}}$ for full-vortex. Here $K = 0.1$.

of the critical point is of a linearly dispersing gapless fermion and since the Kitaev chain is dual via the Jordan-Wigner transformation to the quantum Ising chain, is known that this criticality has $c = \frac{1}{2}$. For $J > 1/2$ there are two momenta p_c where linearly dispersing chiral fermions appear, but only one is independent due to the Majorana condition. Then, at one of the critical momenta $\frac{3\pi}{2} \leq p_c < \pi$ the chain describes complex fermions with staggered complex hopping. The low energy theory is again of a dispersing fermion, with $E = \pm|\sin(\frac{q-2\pi/3}{2})|$ for $J = 1$ at $p_c = \frac{2\pi}{3}$, as the function of the momentum $q \in [0, 2\pi]$ along the chain, again consistent with $c = \frac{1}{2}$.

For $K \neq 0$ the criticality again occurs for $J = 1/2$ at $p_c = \pi$, as seen from 4.9, and the gapped topological phase for $J > \frac{1}{2}$ has $|\nu| = 1$ with chirality depending on $\mathrm{sgn}(K)$. We can think of the criticality as an interface between the trivial phase, playing the role of the vacuum, and the topological phase. As we see from Fig. 4.12, where we vary the J-hopping along the p-chains as $J = \sin\frac{\pi j}{2L_x}$, so that one part of the torus is in the trivial and another in the topological phase, there are chiral gapless dispersing Majoranas appearing on the interface. They are described by a $c = \frac{1}{2}$ CFT [13] and they are viewed as an achiral fermion, again consistent with $c = \frac{1}{2}$, same as for $K = 0$.

In the full-vortex sector the gapless phase ($K = 0$) has four Fermi points. At

$J = 1$ the two at $p_c = \frac{\pi}{6}, \frac{5\pi}{6}$ are independent and look like

$$H(p_c) = \frac{i}{2}\sum_j \gamma^{b\dagger}{}_j \gamma^w{}_{j-1} + ((-1)^j e^{-ip_c} + 1)\gamma^{b\dagger}{}_j \gamma^w{}_j + \text{h.c.}, \tag{4.24}$$

with dispersion $E = \pm\sqrt{3 \pm \sqrt{6 + 2\cos(2p_c) + \cos(2p_c - 2q) - \cos 2q}}$ which is linear around $p_c = \frac{\pi}{6}, \frac{5\pi}{6}$ at $q = \frac{\pi}{3}, \frac{2\pi}{3}$, respectively. These two fermions contribute total $c = 1$. The transition between the $\nu = 0$ phase and the gapless phase occurs at $J = 1/\sqrt{2}$. Now the critical chains at $p_c = 0, \pi$ are staggered Majorana chains with dispersion $E = \pm\sqrt{2 \pm \sqrt{(7 - \cos q)/2}}$ and so they both describe independent linearly dispersing fermions contributing $c = 1$.

When $K \neq 0$, the transition may occur at a different point, $J = \sqrt{\frac{1-K^2}{2}}$, but as there are still two independent Fermi points, the understanding of $c = 1$ for the $(0 \leftrightarrow \pm 2)$ transition is the similar. The edge spectra of the $\nu = \pm 2$ phases for $K \neq 0$ are again described by the same CFT and coexist at the critical point $J = \sqrt{\frac{1-4K^2}{2}}$ (see Fig. 4.12).

Finally, the spectrum at the no-vortex to full-vortex $(\pm \leftrightarrow \pm 2)$ transition is shown in Fig. 4.11. For $J = 1$ and $K \neq 0$ it occurs at $\theta = \frac{3+4K^2}{4}$, and the gap closes at $p_c = 0$. This critical point as well is described by a $c = 1/2$ CFT. For $K = 0$ the critical point is $(0 \leftrightarrow \pm 1 \leftrightarrow \pm 2)$ and is described by a $c = 1$.

4.6.3 Anatomy of Critical Entanglement

We now turn to dissect the entanglement (4.22) of the gapless phase ($J > \frac{1}{2}$, $K = 0$) in the no-vortex sector ($\theta = 0$). This is a semimetallic case of Majorana fermions with two Fermi points which are furthest away from each other at $p_c = \pm\frac{2\pi}{3}$ for $J = 1$ and their distance shrinks as $J \to \frac{1}{2}$. As we see in Fig. 4.9, the phase exhibits flat edge states between the Fermi points.

We then approximate the entropy per momentum p as arising from three components

$$S_{\text{comp}}(p) = \begin{cases} S_{\text{edge}} = \log 2 & p \in \Delta p, \\ S_c & p = p_c, \\ S_{qc} & p \notin \{\Delta p \cup p_c\}. \end{cases} \tag{4.25}$$

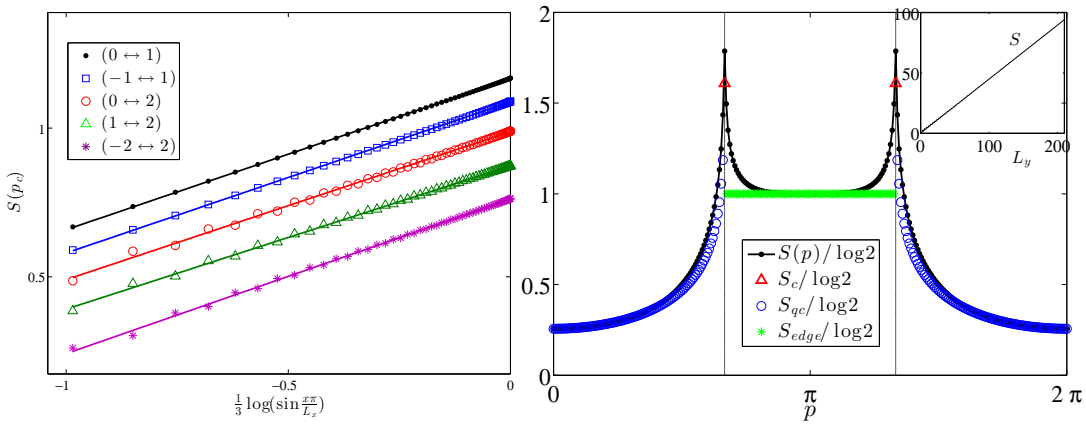

Figure 4.13: (Left) Entropy scaling of p_c-chains as a function of the chord length dictated by (4.21) for the criticalities studied and characterised by the Chern number on either side of the transition, $(\nu_1 \leftrightarrow \nu_2)$. For each critical chain, linear fit (solid lines) implies central charge $c = 1/2$. (Right) Composite entropy, S_{comp}, in the gapless no-vortex phases $K = 0$, $J = 1$. The flat band contributes S_{edge} between the Fermi points $p_c = \pm\frac{2\pi}{3}$, exactly where the critical contributions S_c arise, and quasi-critical chains contribute S_{qc} outside of p_c. The non-universal constant in (4.21) is chosen such that $S_{\text{qc}}(0) = S(0)$. Here $L_x = L_y = 300$. (Inset) Even if the system is gapless, for a fixed partition size x the system still obeys the area law. Here $x = 105$.

The range Δp for the edge state contributions, which due to the edge velocity vanishing coincides with $\frac{2\pi}{3} \leq p \leq \frac{4\pi}{3}$, can be obtained analytically for $K = 0$ (see Appendix C.5).

For the correlation length of a quasi-critical p-chain we write $\xi(p) \approx 1/G(p)$. The energy gap of each chain is known analytically and we refer to the Appendix C.2 for its form. Neglecting the quasi-critical contributions between the Fermi points and assuming that the edge states are the only contribution, we find that the approximation is satisfactory, $\frac{|S-S_{\text{comp}}|}{S} \approx 6\%$ as we shown in Fig. 4.13. The presence of edge states implies that also the gapless phase exhibits a lower bound of entanglement, that is now given by $S \geq \frac{L_y}{2\pi}\Delta p \log 2$. We also find that even if the system is critical, for a fixed partition length x the entanglement entropy

still obeys the area law.

Such decomposition of the entropy is straight-forwardly generalisable to the full-vortex case. For the gapless phase $\frac{1}{\sqrt{2}} < J < 1$ and $K = 0$ we can decompose the entropy into three analogous contributions. Furthermore, the other criticalities presented above adhere to the same decomposition, with the absence of the S_{edge} contribution.

4.6.4 Lower Bound for Effective Central Charge

Recalling that the independent p-chains are those for $p \in [0, \pi]$, implying that $H(p_c) = H(-p_c)$, we conclude that the total entropy at a critical point containing N_c critical p-chains with $p \in [0, \pi]$ scales with an effective central charge

$$\tilde{c} \geq cN_c. \tag{4.26}$$

The lower bound becomes apparent for an appropriate aspect-ratio of the system as well as that of the partition. As shown in Fig. 4.14, the lower bound is saturated in the thin-torus limit $L_y \ll L_x$ when L_y is commensurate with the critical momenta p_c. As $L_y \to L_x$ and the p-momentum density increases, the effective central charge is always $\tilde{c} > cN_c$ as quasi-critical chains appear around p_c and add to the scaling for small compared to their correlation length partition lengths x. Thus in the thermodynamic limit, the lower bound of the effective central charge can only be reliably obtained in the large partition limit $x \to L_x/2$, i.e. as the partition size approaches half the system size [62] and the system has its best chance to appear quasi-1D.

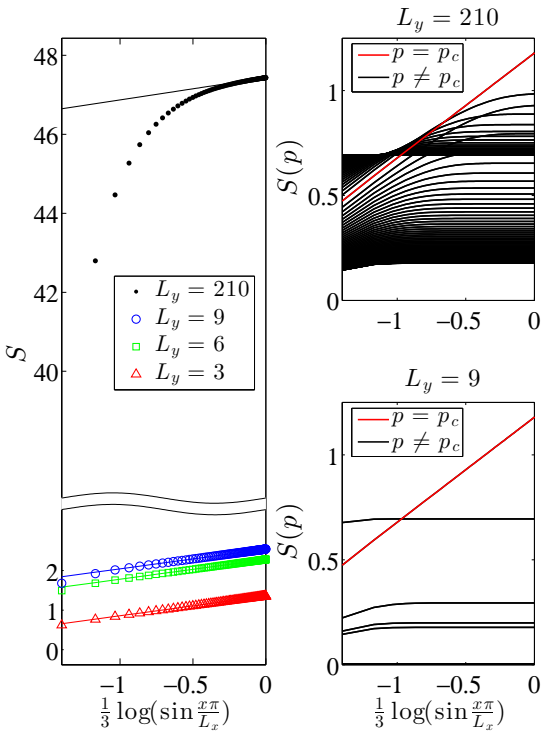

Figure 4.14: Scaling of the total entropy S in the gapless no-vortex phase ($\theta = 0$, $J = 1$, $K = 0$) as a function of the partition-length x for cut-lengths L_y commensurate with $p_c = \frac{2\pi}{3}$. (Left) For a thin torus, $L_y \ll L_x$, the quasi-1D system exhibits effective central charge $\tilde{c} = 1/2$. For a fat torus, $L_y \approx L_x$, the lower bound of $\tilde{c}$ is approached as $x \to \frac{L_x}{2}$. (Right) For $L_y \ll L_x$ (Bottom) the p_c-chain dominates the scaling. For $L_y \approx L_x$ (Top) Quasi-critical chains show scaling even when $x \to L_x$ thus contributing to $\tilde{c}$. Here $L_x = 210$.

4.7 Entanglement Freedom

Reflecting on how remarkable it is that such a simple exactly solvable model can host both topological phases and topological order, we are inspired to compute the interaction distance, given by (3.16), of the ground state, $|\Psi\rangle_{\{+\}}$. As we will see, our result allows us to draw conclusions about states of other vortex sectors, as well. First we create a partition A which we take to be deformable to a disk, which is not our usual cylindrical cut on a torus, as here we are not interested in edge properties, but rather in just the structure of the many-body entanglement spectrum, and let the reduced density matrix supported on A be ρ.

Now recall Yao and Qi's result presented in section 4.3, stating that the correlations of the fermions and the gauge field across an entanglement cut are independent. In particular, in Ref [100] it is proven that the spectrum of ρ is the direct product of two spectra $\rho = \rho_u^\flat \otimes \rho_\gamma$, as the separability of the state into a u and a γ component is respected under reduction to A. The $\rho_u^\flat$ contribution stems from the $\mathbb{Z}_2$ gauge field and ρ_γ is the density matrix obtained from the free

Majoranas. In particular, for a partition boundary of length $|\partial A|$ (this is how many (i,j)-links are cut) the spectrum of $\rho_u^\flat$ has one eigenvalue with $2^{|\partial A|-1}$-fold degeneracy. We will call such spectra "flat". Now, $D_{\mathcal{F}}(\rho_\gamma) = 0$ by definition of the interaction distance. Furthermore, a flat spectrum of degeneracy equal to a power of 2 can be recreated by zero-modes whose number is equal to that power. We will explore this further in Section 6.5 for more generic flat spectra.

This means that $\rho_u^\flat$ and ρ_γ both satisfy a tensor product structure over free-fermion modes and as a result so does ρ. Therefore, $D_{\mathcal{F}}(\rho) = 0$, and since this argument holds for any cut, it renders $|\Psi\rangle_{\{+\}}$ free. This is a surprising result as it holds regardless of the coupling regime of the model, that can support Abelian anyons in the Toric Code extreme dimerisation limit and $\mathrm{SU}(2)_2$ non-Abelian anyons for $J_x \approx J_y \approx J_z$. However, these free fermions are in general non-local, and in fact in this case they are as articulated by the $\mathbb{Z}_2$ symmetrisation. We remind that this is also the source of the topological entanglement entropy [100].

Again from the Appendix of Ref [100] we conclude that the above analysis holds for any vortex sector, as also for them the entanglement spectrum is a direct product of a power-of-2 flat spectrum with a free-fermion one, giving again $D_{\mathcal{F}} = 0$. We note here that when analysing other eigenstates of the honeycomb one needs to enforce a the parity constraint on the fermions which is compatible with the number of vortices present in the system and the boundary conditions [117]. This however does not alter our result.

Finally, it is important to acknowledge that even if we have diagnosed the eigenstates (4.7) as free, the energy spectrum of the Honeycomb model is not one of free fermions. This can be confirmed as follows. We know that the Hamiltonian is a direct sum of free-fermion vortex sectors each with its own free-fermion energy spectrum and that $D_{\mathcal{F}} = 0$ for any free-fermion entanglement spectrum. Thus, given an energy spectrum we can rescale it so that it is normalised and then compute its $D_{\mathcal{F}}$. However, since the vortex sectors of a large system are too many to efficiently carry out this computation, and exact diagonalisation of the model in the spin language restricts us to too small system sizes compared to the correlation length, we work with random free spectra without loss of generality. That is, we take ρ_1^{f} and ρ_2^{f} diagonal matrices with random free fermion spectra generated as described in Appendix B.6.5. By construction each has $D_{\mathcal{F}}(\rho_{1,2}^{\mathrm{f}}) = 0$.

Then we compute $D_{\mathcal{F}}\left(\frac{1}{2}\left(\rho_1^{\mathrm{f}} \oplus \rho_2^{\mathrm{f}}\right)\right)$ and realise that in general it is non-zero. The numerical results presented in Appendix B.6.1 we show that for the special case $\rho_1^{\mathrm{f}} = \rho_2^{\mathrm{f}}$ the interaction distance of their direct sum is again zero. Regarding now the model's ability to host anyons, this can only be appreciated when one interpolates adiabatically between vortex sectors [91].

4.8 Summary

We have examined properties of both the fermionic and gauge part of the entanglement in Kitaev's honeycomb model. We have extracted universal manifestations of the edge states in the topological phases via our monogamy qualifier and provided consistent alternative interpretations to the origin of the entropic lower bound. For other topological phases of free Majorana fermions we expect that these results will hold, up to modifications to accommodate edge state deformations that can change the number of crossings without a phase transition in multilayer systems [118]. Furthermore, we explored the meaning of entanglement freedom in this model and connected it with the topological order, reinforcing the reason why this model is so important. In the next chapter we use the arguments and results obtained from this model to identify universal features of models that are related to the honeycomb directly or indirectly.

Chapter 5

Related Free Models

5.1 Introduction

We begin with Haldane's honeycomb model, a modification of graphene hosting a topological phase. In the same way that a Kitaev wire is located at the $p^\star = \pi$ momentum in the no-vortex sector, we find a Su-Schrieffer-Heeger chain in Haldane's case. Finally, we introduce a novel model which we name Chern semi-metal, exhibiting a vanishing indirect gap separating bands characterised by Chern numbers. These models are studied with our entanglement diagnostics and analogues of results obtained from the analysis of Kitaev's model.

5.2 Haldane's Honeycomb Model

Haldane's honeycomb is a toy model for the integer quantum Hall effect [119]. It is a modification of graphene, which describes free complex fermions with nearest-neighbour hoppings. Graphene is able to host edge states on its boundaries [120]. Haldane added chiral next-nearest neighbour hoppings to induce a gap while having vanishing net flux through the system. The hopping pattern is the same as that of Kitaev's no-vortex sector (see Fig.4.1) and the Hamiltonian is

$$H = \sum_{\langle i,j \rangle} t_1 f_i^\dagger f_j + \sum_{\langle\langle i,j \rangle\rangle} t_2 e^{i\phi} f_i^\dagger f_j + \text{h.c.}. \tag{5.1}$$

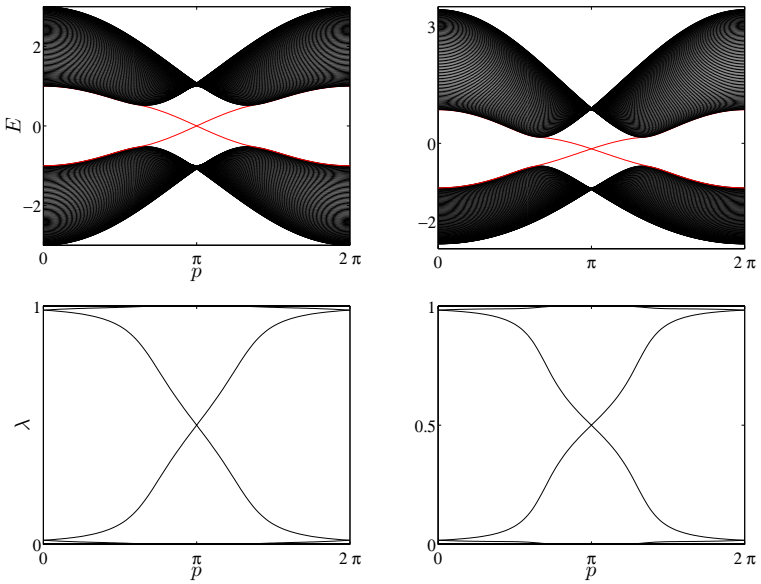

Figure 5.1: Energy on a cylinder (Top) and entanglement spectrum on a torus (Bottom) of Haldane's model for $t_1 = 1$, $t_2 = 0.1$. For $\phi = \frac{\pi}{2}$ (Left) the energy spectrum has a fake particle-hole symmetry and for $\phi = \frac{\pi}{4}$ (Right) it is mirror-symmetric around $p = \pi$ due to sub-lattice symmetry

where $t_1, t_2 > 0$, and the sign of $\phi \in [0, 2\pi)$ is consistent with a chosen chirality. The model also invites a staggered chemical potential term which creates an imbalance between the black and white sublattices and breaks inversion symmetry. The robustness of the topological phase to this staggering is highest when $|\phi| = \pi/2$. Here we do not explore the effect of this term, as the universal signatures we are interested in are easily generalisable to that case.

5.2.1 Monogamy

To get the covariance matrix for the Haldane model, we decompose the fermions in the Hamiltonian into Majoranas and then proceed as for the Kitaev model. That is, we compute their Majorana-Majorana correlations and then we obtain Γ. When $\phi \neq 0, \pi$ the system is in a gapped topological phase characterised by Chern number $|\nu| = 1$ and exhibits a single Dirac edge state per boundary. Placing the system on a torus and partitioning into two cylinders as was done

for the Kitaev's honeycomb, the monogamy qualifier $\mathcal{S}_q$ captures the signatures of maximally entangled pairs across the cut. In Fig. 4.7 (Left) we see $\mathcal{S}_\infty = 4$. This is the same result obtained for the full-vortex sector since in that case we have two Majorana edge states per edge whose dimensionalities combine to that of a singe Dirac fermion arising at the boundaries of Haldane's model. Thus the lower bound to the entropy is again $S \geq 4 \log \sqrt{2}$.

We expect this signature to be robust under disorder as it is for Kitaev's no-vortex sector. Disorder is added to the hoppings as is done for the Kitaev model with the addition of an on-site random chemical potential. As illustrated in Appendix D.1, the monogamy signature is stable under weak disorder. For strong disorder we observe the highest resilience deepest in the topological phase.

5.2.2 Chain Decomposition and SSH Model

Performing a Fourier transformation of the complex fermions in one direction, the Haldane model is decomposed into p-chains. Representative band structures and corresponding entanglement spectra are shown in Fig. 5.1 and are deformable to those obtained from the no-vortex sector of Kitaev's model (Fig. 4.3). Since we do not break sub-lattice symmetry the edge states cross at $p^\star = \pi$.

Haldane's $p^\star$-chain is mappable to the 1D Su-Schrieffer-Heeger model [121] of spinless fermions on a chain with alternating weak-strong hoppings

$$H = \sum_j -[t + \delta t(-1)^j] f_i^\dagger f_{j+1} + \text{h.c.}. \tag{5.2}$$

The momentum kernels of Kiteav's $p^\star$-chain in the no-vortex sector as well as Haldane's $p^\star$-chain have unitarily equivalent q-momentum kernels to that of the SSH model. This is because all these three models have winding number $w = 1$ in their topological phase as demonstrated in Fig. 5.2. In particular, when SSH is at its topological fixed point for $t = \delta t$ and the fermionic sites decouple completely from the Hamiltonian for open boundaries, its kernel becomes exactly equal to that of Haldane's $p^\star$ chain for $\phi = \frac{\pi}{2} \text{mod} \pi - q$ and $t = -\frac{t_1}{2}$. We refer to Appendix D.2 for more details on the mapping of the $p^\star$-chain to SSH and to Appendix D.3 for a brief study of SSH's resilience to the introduction of disorder.

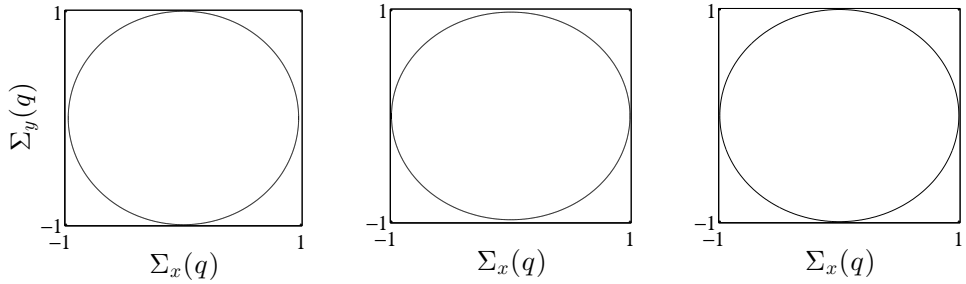

Figure 5.2: Winding of Pauli vector of q-momentum kernels obtained for Kitaev's no-vortex $p^\star$-chain ($J = 1$, $K = 0.1$) (Left), Haldane's $p^\star$-chain ($t_1 = 1$, $t_2 = 0.1$, $\phi = \frac{\pi}{2}$), and the SSH model ($t = 1$, $\delta t = 0.1$).

Origin of Entropic Lower Bound

In analogy with the Kitaev model, where the entropic lower bound arises from the existence of edge states in the Kitaev chain, the Haldane model's lower bound is due to the edge states of the SSH model. They cannot be adiabatically be removed and contribute the maximal entanglement of $\log 2$ entropy per edge. Thus from an entropic point of view we could call the no-vortex sector of Kitaev a "half Haldane model".

Entropy Toy Model

To push the analogy further, we can again capture the behaviour of the entropy considering only the edge states by constructing a toy model comprising four complex fermions

$$H = (a_1^\dagger a_4 + a_2^\dagger a_3) + iw_p(a_1^\dagger a_2 + a_3^\dagger a_4) + \text{h.c.} \tag{5.3}$$

with a π-flux through the 4-site chain implemented by making the weak hopping, $w_p = \kappa_{\text{tm}} E_\pm(p)$ imaginary since the ground stat. Its entropy, S_{tm}, is computed numerically via the correlation matrix which we restrict to sites $1, 2$ and κ_{tm} is again optimised so that $\frac{|S - S_{\text{tm}}|}{S} \approx 1\%$. The form of the toy model's entropy can be calculated analytically as well as shown in the Appendix D.4.

5.3 DKP Semimetal

In this section we present a novel model which we call Chern semi-metal and present its energy and entanglement spectrum and interpret them in light of our previous results obtained by our entanglement diagnostics. This model hosts gapless topological phases that share several properties with the Chern insulators like a well-defined Chern number associated to each band, topologically protected edge states and topological phase transitions that occur when the bands touch each, with linear dispersion around the contact points.

5.3.1 The Model

Our model describes free-fermions on a Lieb lattice (face-centered square) with hopping pattern shown in Fig.(5.3) (Left). The Hamiltonian is

$$H = \sum_{j,k} J(a^\dagger_{j,k} b_{j,k} + b^\dagger_{j,k} c_{j,k}) + K(a^\dagger_{j,k} b_{j+1,k} + b^\dagger_{j,k} c_{j,k+1}) + M c^\dagger_{j,k} a_{j,k} + \text{h.c.}, \quad (5.4)$$

where $a_{j,k}, b_{j,k}, c_{j,k}$ are complex fermions, represented by triangles, circles, and squares respectively in Fig.(5.3) (Left), living in the unit-cell with coordinates j, k on the square lattice, where $J, K > 0$ and $M = me^{i\theta}$. The model is constructed to resemble properties of the Haldane model. Note that the net flux through each square is zero.

5.3.2 Phase Diagram

Since the unit-cell contains three sites, there are three energy bands. For $m = 0$ there is a Dirac-like cone with tip at zero energy and a zero-energy flat band shown in Fig.(5.3). The flux threading the triangles breaks time-reversal symmetry and for appropriate flux-values detaches the bands but keeps a zero indirect gap and gives a Chern number to two of the bands as indicated in Fig.(5.3). In Appendix D.5 we present details regarding the quantum phase transitions in the phase diagram. The Chern number can be computed by integrating the Berry curvature on the bands since they do not touch and we present the phase diagram in Fig(5.4).

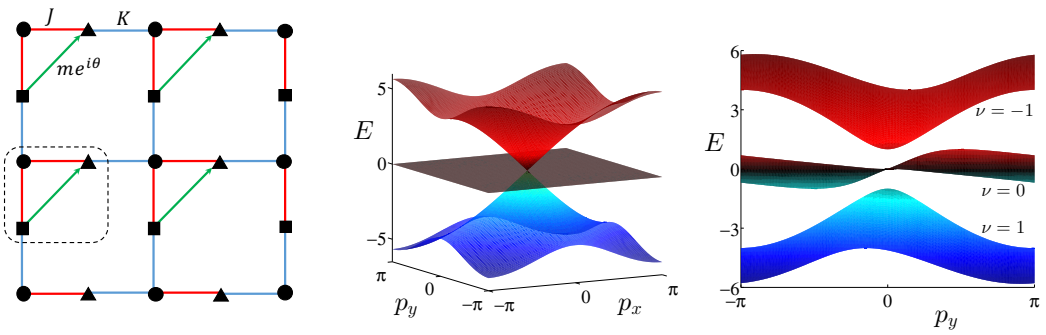

Figure 5.3: (Left) Hopping pattern on the Lieb lattice. The dashed line encloses the unit-cell. Intra-unit-cell hoppings (J) are in red lines and inter-unit-cell ones with blue (K). The flux-inducing complex hopping ($me^{i\theta}$), represented in green, breaks time-reversal symmetry. (Middle) For $M = 0$ the cone touches the flat band and for $M = 0.5i$ the cone gaps out and the flat band is deformed so that the system is gapless. Here $K = -J = 1$.

5.3.3 Relativistic Dispersion

Focusing on the cone appearing for the time-symmetric $M = 0$ case at momentum $p_x = p_y = 0$, we expand the Hamiltonian's momentum kernel, which is presented in the Appendix, around the tip of the cone and verify that the dispersion is linear. The linearised kernel, h_{eff}, is a relativistic first-order Hamiltonian,

$$h_{\text{eff}} = K\left[\beta^x, \beta^0\right] p_x + K\left[\beta^y, \beta^0\right] p_y + M\beta^0, \tag{5.5}$$

where we fixed $J = -K$ and the matrices

$$\beta^0 = \begin{bmatrix} 0 & 0 & -1 \\ 0 & 0 & 0 \\ 1 & 0 & 0 \end{bmatrix}, \beta^x = \begin{bmatrix} 0 & 0 & 0 \\ 0 & 0 & i \\ 0 & -i & 0 \end{bmatrix}, \beta^y = \begin{bmatrix} 0 & -i & 0 \\ i & 0 & 0 \\ 0 & 0 & 0 \end{bmatrix} \tag{5.6}$$

satisfy, as confirmed by Palumbo [21], the Duffin-Kemmer-Petiau algebra [122],

$$\beta^\mu \beta^\nu \beta^\sigma + \beta^\sigma \beta^\nu \beta^\mu = \beta^\mu \eta^{\nu\sigma} + \beta^\sigma \eta^{\nu\mu}, \tag{5.7}$$

where $\eta^{\mu\nu}$ is the Minkowski metric with signature $\text{diag}(\eta^{\mu\nu}) = (-1, 1, 1)$. The DKP theory describes relativistic spin-0 and spin-1 particles by employing the

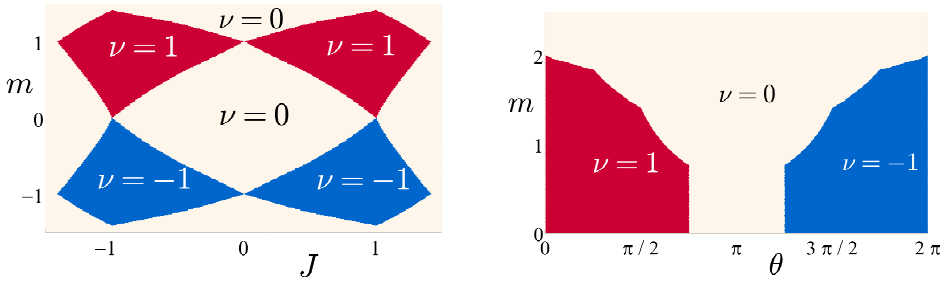

Figure 5.4: (Up) Chern number phase diagram in function of J and m with $K = 1$ and $\theta = \pi/2$ when the lowest band is completely filled. (Low) Phase diagram in function of m and θ with $K = -J = 1$.

same formalism used by Dirac for spin-1/2 particles, i.e. it is first order in the fields contrary to the second order Klein-Gordon equation. The effective Hamiltonian, h_{eff}, is thus fully relativistic but from a Dirac Hamiltonian. This implies that this model does not fit in the periodic table of topological gapless phases which classifies Hamiltonians constructed out of Pauli matrices [36].

The actual development of the model begun from the DKP algebra itself. The question was to find the simplest algebra of 3×3 matrices out of which to construct a three-band model which is gapless but still exhibits Chern numbers. Since the DKP algebra describes bosons, one would be sceptical to implement it in a fermionic system. However, starting from h_{eff}, we turn the imaginary unit in the $\beta^{x,y}$ matrices into phases that will play the role of momentum and obtain a matrix that can be interpreted as the kernel of a Hamiltonian of a condensed matter system and choose to fill these bands with fermions.

5.3.4 Edge States

Since two of the three bands can have a $|\nu| = 1$ Chern number, we the existence of edge states. After performing a Fourier along $\mathbf{v}_x$ we plot in Fig. 5.5 the energy spectrum on a cylinder as well as the entanglement spectrum on a torus which is computed by reducing the correlation matrix $\langle f_i^\dagger f_j \rangle$ on a cylinder, where $f = a, b, c$. This is done for $\frac{1}{3}$-filling, and the results are equivalent for $\frac{2}{3}$-filling. Edge states that traverse the gaps connect bands with opposite ν and flat edge

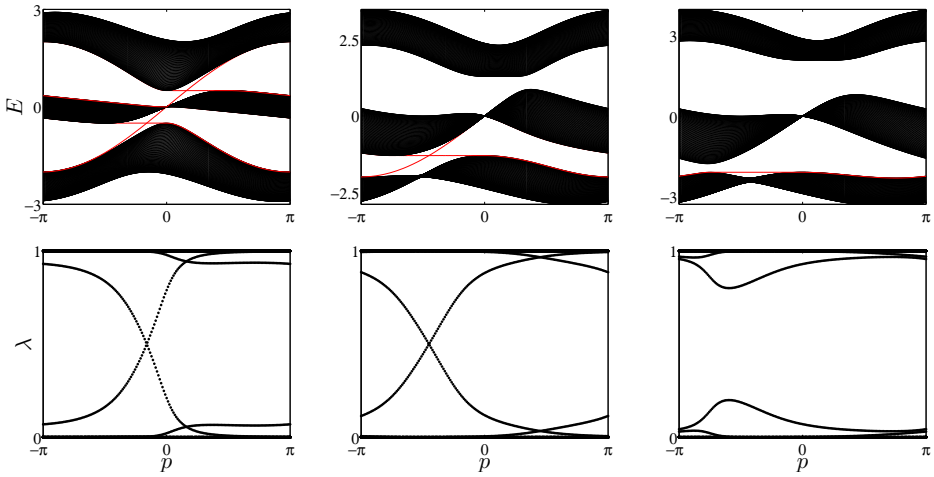

Figure 5.5: Energy on cylinder and entanglement spectrum on torus for $K = -J = 1$ and 1/3-filling. The edge states cross bands with opposite Chern numbers $\nu = \pm 1$ and the other band has has $\nu = 0$, (Left) $m = 0.5$, $\theta = \frac{\pi}{2}$ and (Right) $m = 1.3$ and $\theta = \frac{\pi}{4}$. When the flux is too large, $m = 2.1$ and $\theta = \frac{\pi}{4}$ the system is an trivial insulator with all bands having $\nu = 0$. (Bottom) The entanglement spectrum captures the dispersing edge states.

states traverse the vanishing indirect gap to connect a non-trivial band with a trivial one as shown in Fig. 5.5.

5.3.5 Resilience Against Disorder

We then show that the Chern semi-metal is robust under disorder. Disorder is introduced in all of the hopping amplitudes $t = K, J, m$ in the form $t(1 \pm \delta t)$, with $|\delta t| \leq \Delta$. In Fig. 5.6 we present the Chern number, ν, computed in real space from the correlation matrix as in (2.14) and averaged over disorder realisations, as a function of θ and Δ is shown in Fig. 5.6 (Left). The phase diagram is reminiscent of that obtained for the Haldane model in Fig. D.1. For weak disorder, $\Delta < 0.5$ the topological phase is robust showing a non-trivial value of the Chern number. In order to identify the semi-metallic band structure, we compute the average density of states for weak disorder and plot it in Fig. 5.6 (Right). In the clean case the density of states shows minima at the energies where the zero indirect gaps are located. The minima are not lifted for weak disorder

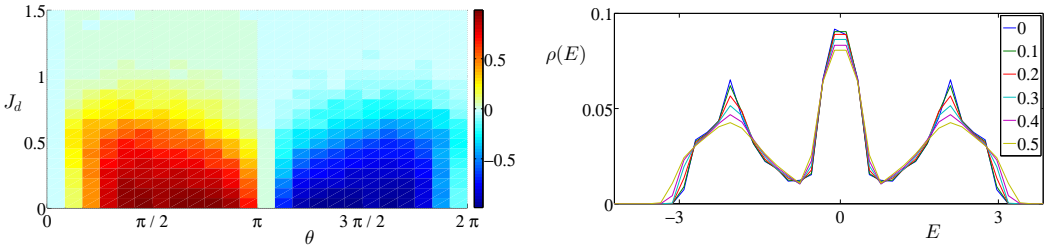

Figure 5.6: (Left) Chern number, ν, against θ and J_d. The filling is $\frac{1}{3}$ and the system size $L_x = L_y = 20$. Each disorder realisation was averaged 20 times. For weak disorder, $\Delta < 0.5$, the topological phase is robust and for strong disorder the ν vanishes. (Right) Density of states, $\rho(E)$, for $\Delta < 0.5$ (Legend). Here we averaged over 10^3 disorder realisations for $L_x = L_y = 26$. The two minima correspond to the zero indirect gap. The density of states profile does not change around the zero indirect gaps. Here $K = -J = 1$, $m = 0.5$ and $\theta = \pi/2$.

consistent with the non-trivial Chern number, $|\nu| \approx 1$, showing the robustness of the Chern semi-metallic phase.

5.4 Summary

In this chapter we studied free-fermion models, namely Haldane's honeycomb, the Su-Schrieffer-Heeger chain, and our novel Chern semi-metal. Entropically, we interpreted the Haldane model as a double no-vortex sector of Kitaev's honeycomb and equivalent to the full-vortex sector. Furthermore, we traced the origin of its entanglement in the gapped phase to the topological robustness of an SSH chain, in analogy with Kitaev's no-vortex sector and its robust Kitaev wire. Finally, the Chern semi-metal was examined using tools like the entanglement spectrum and parallels with Haldane's model.

Chapter 6

Related Interacting Models

6.1 Introduction

In this chapter we explore entanglement patterns in interacting fermionic lattice models. We start with the Su-Schrieffer-Heeger-Hubbard model, an interacting version of the SSH chain, and show that the monogamy argument holds in this case as well, rendering the monogamy signature non-trivial. Then we turn to capturing the effect that interactions have on the ground state. As a simple example we take interacting spinless fermions on a chain and capture the effect of interactions with the skewness of the entanglement spectrum. For a more sophisticated measure we then apply the interaction distance to the quantum Ising chain, as well as to parafermionic chains. Finally, we make remarks on Abelian string-nets, whose entanglement spectra resemble those obtained by parafermionic chains.

6.2 SSHH

The Su-Schrieffer-Heeger-Hubbard model describes spinful fermions hopping on a chain of length L with alternating weak-strong hoppings like the SSH model [121] with on-site Hubbard interaction of strength U. The Hamiltonian is

$$H = \sum_{s} \sum_{i=1}^{L} \left(- \left(t + \delta t (-1)^i \right) f_i^{s\dagger} f_{i+1}^{s} + \text{h.c.} \right) + \frac{U}{2} \sum_{i=1}^{L} (n_{\uparrow,i} + n_{\downarrow,i} - 1)^2. \quad (6.1)$$

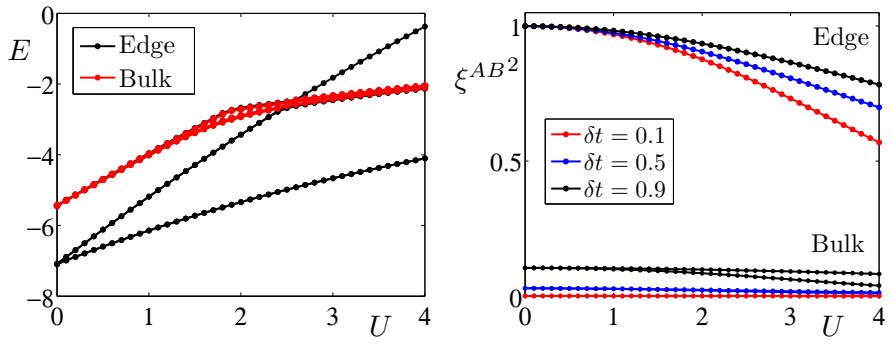

Figure 6.1: (Left) Spectrum of the twelve lowest many-body states of the SSH model with interactions U for $L = 6$ and open boundaries terminating on weak bonds, $\delta t = 0.75$. The black lines are two-fold degenerate. The ground state degeneracy reduces from four-fold ($U = 0$) to two-fold ($U > 0$). (Right) The M-fold degenerate squared singular values $\xi_j^{AB\,2}$ of Γ_{AB} with periodic boundary conditions. Region A (B) contains sites $1, 2, 3$ $(4, 5, 6)$, where we have allowed an entanglement cut through a unit-cell leading to $M = 4$.

where $s = \uparrow, \downarrow$ and $n_i^s = f_i^{s\dagger} f_i^s$ populations for each spin with total population in that spin component $N_s = \sum_i^L n_i^s$. The total spin is defined as $S_z = \frac{N_\uparrow - N_\downarrow}{2}$ and is a conserved quantity since the Hamiltonian conserves the particle number. Thus the Hamiltonian splits into S_z-sectors determined by numbers of particles which can take the values $N_\uparrow = 0, 1, \ldots, L$ and $N_\downarrow = L - N_\uparrow$.

Let us take $U = 0$. Then the chain decouples into two SSH chains, one for each spin component. For periodic boundary conditions the ground state is unique and lies in the $S_z = 0$ sector to which we restrict. For open boundary conditions there are $L - 2$ single-body states in the lower band and $L - 2$ in the upper band and four zero-energy modes. We work at half filling and we choose L to be even so that $N_\uparrow + N_\downarrow = L$. The lower band is fully occupied and the many-body ground state degeneracy is the number of ways 2 particles can occupy four zero-modes, which is six. Two of these many-body ground states have $S_z = \pm 1$ and the $S_z = 0$ has a four-fold degeneracy in the ground state. When interactions are turned on, $U > 0$, the degeneracy of the ground state becomes two-fold as shown in Fig. 6.1 (Left). This is due to the Hubbard interaction penalising triplets and favouring singlets on each site [123]. The intuition employed to construct the toy model for

the edge entropy for Kitaev's no-vortex sector and Haldane's honeycomb can be used again to reason about the entropy of the edge under the hubbard.

6.2.1 Monogamy

Consider now the system in terms of correlations. The many-body entanglement spectrum was later studied in Ref [124] extending the study also for $U < 0$. For periodic boundary conditions, when $U = 0$ and $\delta > 0$ so that each SSH s-chain is in the topological phase, and the covariance matrix Γ contains all the information about the ground state, the monogamy qualifier converges, $\mathcal{S}_{q\to\infty} \to 8$, indicating $M = 8$ maximally entangled Majorana pairs across the cut, consistent with two Dirac fermion virtual edge modes per ∂A-component. Since in the topological phase the weak bond is inside the unit-cell, ∂A cuts through strong bonds. On the contrary, in the trivial phase, the cut occurs on weak bonds leading to $M = 0$. For $U > 0$ we evaluate the Γ of the ground state by exact diagonalisation, which we expand upon in the Appendix. In this case, however, it does not contain all the information about the ground state. Then we proceed to extract the monogamy signatures from the singular values, ξ^{AB}, of Γ_{AB}. In Fig. 6.1 we see that while the degeneracy of the energy is lifted from four- to two-fold for open boundaries, all four virtual Majorana modes that are highly entangled across ∂A behave identically in terms of ξ^{AB}. They remain at high entanglement and are separated from the bulk contributions, through a "covariance gap". Interestingly, this behaviour holds also when U is large enough so that the energies of the edge states enter the bulk's energies.

We understand this result via the monogamy argument, in that high monogamy signature $\xi^{AB} \approx 1$ corresponds to localisation of the state when the boundary is physical and not virtual. In other words, some edge states may go up in energy but their localisation is unaffected. To verify this, we tune the dimerisation of the chain so that $\delta t \to 1$, reducing thus the localisation length of the edge states. This in turn results in an increase of the maximal ξ^{AB} for finite U-values. We claim that this procedure is analogous to increasing the system size, which is however prohibited by exact diagonalisation's runtime.

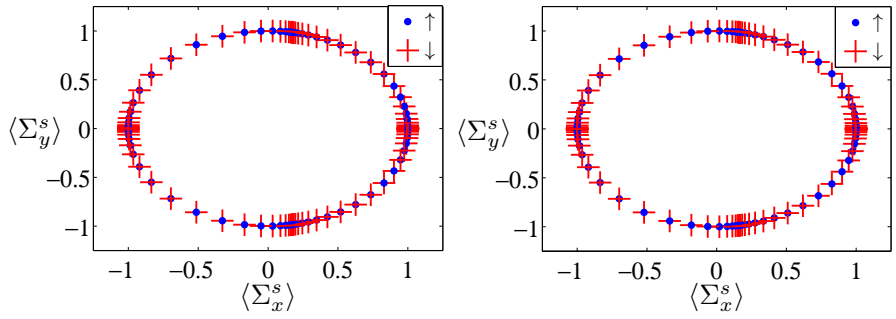

Figure 6.2: Winding of the vectors $\langle \mathbf{\Sigma}^{\uparrow} \rangle$ (blue dot) and $\langle \mathbf{\Sigma}^{\downarrow} \rangle$ (red cross) as the momentum p is varied from 0 to 2π for the interacting SSH model for $L = 8$ and $U = 2$. The vectors wind on the $x - y$ plane. The winding that is present in the non-interacting case $U = 0$ persists when interactions are turned on $U = 2$.

Furthermore, we reconcile the signature obtained by the qualifier $\mathcal{S}_q$ with the chain's non-trivial winding number. Indeed, there are no topological phase transitions and the winding number [125, 126] remains unchanged in the presence of interactions, $U > 0$. In other words, interactions only change adiabatically the edge spectrum and the edge modes remain well-defined. We underline that the key result here is that the covariance matrix can detect edge states also in the presence of interactions even though Γ no longer fully characterises the ground state nor is in one-to-one correspondence with the entanglement spectrum.

The edge entropy of the SSHH model is also studied in Ref [123]. There, the edge degeneracy is obtained from the difference of the entanglement entropy between open and periodic boundary conditions. This method thus captures the drop of the edge degeneracy from four to two. However, the difference from our method is that the monogamy signature indicates the existence of edge states regardless of their energy for open boundaries. In the Appendix E.2 we present a toy model for the edge entropy of the SSHH which is also compatible with the effective edge picture presented in Ref [123].

6.3 Interacting Spinless Fermions

We place spinless femions to hop on a chain with repulsive nearest neighbour interactions. Turning on the interactions, we see the effect on the entanglement

spectrum. The Hamiltonian on an $2L$-long chain is

$$H = \sum_{j=1}^{2L-1} \left(-f_j^\dagger f_{j+1} + \text{h.c.} \right) + U n_i n_{i+1}. \tag{6.2}$$

6.3.1 Asymmetry in the Entanglement Spectrum

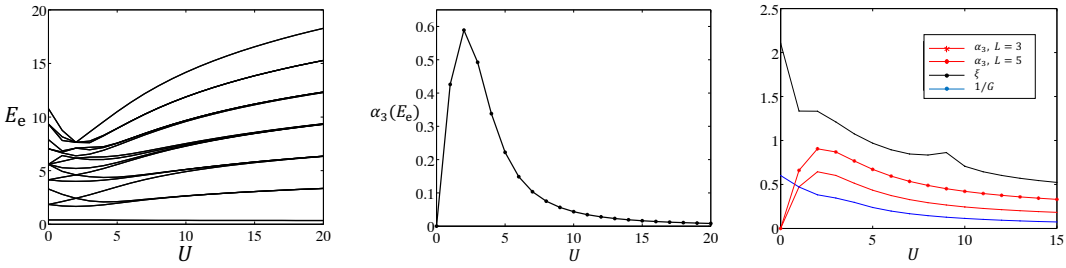

Figure 6.3: (Left) Entanglement spectrum, ξ, for $N = L = 5$, symmetric at $U = 0$ and in the large-U limit. (Middle) This behaviour is captured by the skewness, α_3. (Right) For large U the skewness and the correlation length behave similarly, and for a bigger system size the skewness is suppressed. The discontinuity in ξ is attributed to the ground state degeneracy changing.

The ground state is obtained in Fock space via exact diagonalisation. We equipartition the $2L$-long chain into regions into two segments containing L sites. For periodic boundary conditions we have a unique ground state. However, in the large-U limit the ground state degeneracy exponentially converges to two-fold. Increasing the repulsive interaction $U > 0$ we see the asymmetry in the entanglement spectrum E_e rising, $\alpha_3(E_\text{e}) > 0$. Then, the symmetry is restored in the large U limit where $U \gg 1$ witnessed by the skewness approaching zero $\alpha_3 \to 0$ as shown in Fig. 6.3. In the large U limit, the restoration of the symmetry in E_e implies that Wick's theorem effectively holds again and an effective free description of the ground state can be found in terms of the degrees of freedom that correspond to the Schmidt vectors of those symmetric entanglement eigenvalues. Finally, we observe that the correlation length and the skewness behave similarly under increase of U, as shown in Fig. 6.3. That is, there is a better chance that

there exists an effective free description of the state when the correlation length is small. Here the correlation length is computed as the characteristic length-scale from the decay of the off-diagonal elements in the correlation matrix, as well as setting it inversely proportional to the energy gap.

6.4 Quantum Ising Model

Going beyond the simple example of the previous section, we turn to the quantum Ising chain. We consider the ferromagnetic (FM) and antiferromagnetic (AFM) cases. The Hamiltonians are given by

$$H_{\pm}(h_z, h_x) = -\sum_{j=1}^{L}(\pm X_j X_{j+1} + h_z Z_j + h_x X_j), \tag{6.3}$$

where H_+ stands for FM and H_- for AFM [127], the transverse and longitudinal local magnetic fields are denoted h_z and h_x respectively, and we set periodic boundary conditions, $L+1 \to 1$.

Since we are interested in the effect that interactions have in this model, in the fermionic sense, we perform a Jordan-Wigner transformation (see Appendix E.3). When there is no longitudinal field, $h_x = 0$, the model (6.3) reduces to the Kitaev chain with the topological phase for $h_z < 1$. For finite longitudinal field, h_x, a non-local non-quadratic term is introduced.

6.4.1 Entanglement Freedom

We find the entanglement spectrum of the ground state as a function of (h_z, h_x) by exact diagonalisation. We then examine the phase diagram by use of the interaction distance, $D_{\mathcal{F}}$, defined in (3.18).

Freedom Phase Diagram

For a given system size, L, we find that $D_{\mathcal{F}}$ acquires the lowest values away from the critical point for FM (Fig. 6.4 (Left)) and critical line for AFM (Fig. 6.4 (Right)). In those regions, the single-body entanglement energies, ϵ, of the effectively free state σ, converge exponentially with the system size to their asymptotic

values (see Appendix E.4). Around criticality, the correlation length diverges and the effect of interactions is most significant as indicated by higher values of $D_{\mathcal{F}}$. Typically, we find that where mean-field theory is applicable then we find low $D_{\mathcal{F}}$-values. However the converse is not necessarily true.

Dependence on System Size

We now examine the behaviour of the phase diagram as we vary the chain's size. By increasing L we observe a difference in the behaviour of the regions with non-trivial $D_{\mathcal{F}}$-values between the FM and AFM cases. For FM the non-free region resembling a tilted lobe (Fig. 6.4 (Left)) shrinks towards the critical point situated infinitesimally above the phase transition point of the Kitaev chain, $(1, \delta h_x)$. Moreover, the value of $D_{\mathcal{F}}$ diverges with L, thus costituting the interaction as strongly relevant. A plot of $D_{\mathcal{F}}$ exponentially close to $(1, 0)$ is shown in Fig. 6.5. It is important to note here that since $D_{\mathcal{F}}$ is upper-bounded by construction, this divergence needs to be regulated. Turning to the AFM case, we see that the non-trivial region, again resembling a lobe following the critical line (Fig. 6.4 (Right)), shrinks towards the classical critical point $(0, 2)$. Importantly, $D_{\mathcal{F}}$ decreases as L increases, rendering the ground state free over the whole line (except at $(0, 2)$ where it's ill-defined due to its degeneracy extensively diverging with L).

A detailed scaling analysis is performed in Ref [128], where the entanglement spectrum of the ground state was obtained by DMRG [129] and thus larger L is accessible. There it is shown that it is possible to extract critical exponents corresponding to the correlation length around the criticalities of FM and AFM from the scaling of $D_{\mathcal{F}}$ with L. The interaction distance is computed along paths (dashed lines in Fig. 6.4) in the phase diagrams that cross the criticalities and for each system size this data-set is denoted $D_{\mathcal{F}}^L$. Then, a scaling ansatz, which accommodates the upper bound of $D_{\mathcal{F}}$, is used to collapse the $D_{\mathcal{F}}^L$ curves and the numerical values for the exponents obtained are confirmed by the existing values in the literature [128].

Finally, an observation regrading the renormalisation flow of the model should be made. We hint that it is parallel to the gradient of $D_{\mathcal{F}}$ (colour gradient of 6.4) with respect to the fields $h_{z,x}$. Reinterpreting this observation, we state that

an important property of $D_{\mathcal{F}}$ is that it is able to diagnose the renormalisation profile of a given model from data obtained for one choice of system size.

Mapping to the Free Line

We conclude that the ground state can be faithfully described by a Slater determinant everywhere in the phase diagram, save at $(h_z = 1, h_x = \delta h_x)$ and at $(h_z = 0, h_x = 2)$. We underline that this is a surprising result because the Hamiltonian is non-integrable as the energy scales of the Hamiltonian's terms are all comparable in magnitude in these regions of the phase diagram where we find the ground state to be almost free. Therefore now we may ask what the parent Hamiltonian of the free state might be. In this case we take the "free line" $h_x = 0$ and identify a free Ising model $H_{\pm}(h^{\mathrm{f}}, 0)$ with reduced ground state $\rho(h^{\mathrm{f}})$ for which the trace distance $D(\sigma(h_z, h_x), \rho(h^f))$ between the optimal $\sigma(h_z, h_x)$ at point (h_x, h_z) and $\rho(h^{\mathrm{f}})$ is minimised.

The results of this mapping are shown in Fig. 6.6. We observe that in the FM case adding infinitesimal interactions δh_x to the free Ising model with $h_z < 1$ maps the model to a free Ising with $h_z > 1$ in a discontinuous way, as shown in For $h_z > 1$, on the other hand, the map is continuous. In the AFM case the map flows parallel to the critical line and continuously maps the whole phase diagram on the free line. The distance $\min_{h^{\mathrm{f}}} D(\sigma(h_z, h_x), \rho(h^{\mathrm{f}}))$ is shown by the colour scale in Fig. 6.6, where also the equi-h^{f} contours are shown. We observe that away from criticality the mapping is most accurate. In the thermodynamic limit we expect the critical line of AFM to also be identified with a free Ising model because $\min_{h^{\mathrm{f}}} D(\sigma, \rho(h^{\mathrm{f}}))$ decreases with L. Furthermore, the CFT which describes this critical line is proposed to be free [127]. Importantly, note that the parent Hamiltonian that we attributed to the ground state is local with respect to the Hamiltonian whose ground state the freedom we diagnose. This need not in general be the case.

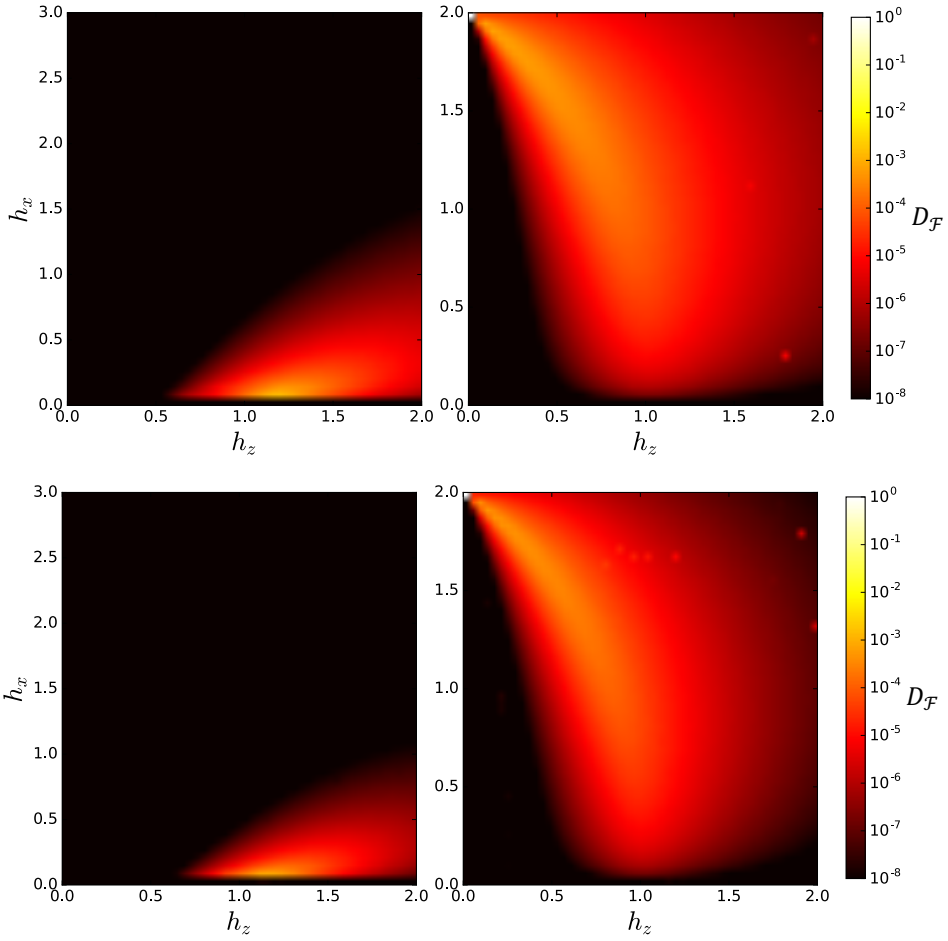

Figure 6.4: Interaction distance, $D_{\mathcal{F}}$ in the (h_z, h_x)-plane for $L = 12$ (Top) and $L = 16$ (Bottom). For FM (Left) we have $D_{\mathcal{F}}$ higher around the a critical point $(1, 0)$ and for AFM (Right) around the critical line connecting $(1, 0)$ and $(0, 2)$. Increasing system size L, the non-trivial regions shrinking around $(1, 0)$ for FM and $(0, 2)$ for AFM. Rogue points are attributed to local minima of $D_{\mathcal{F}}$'s cost function.

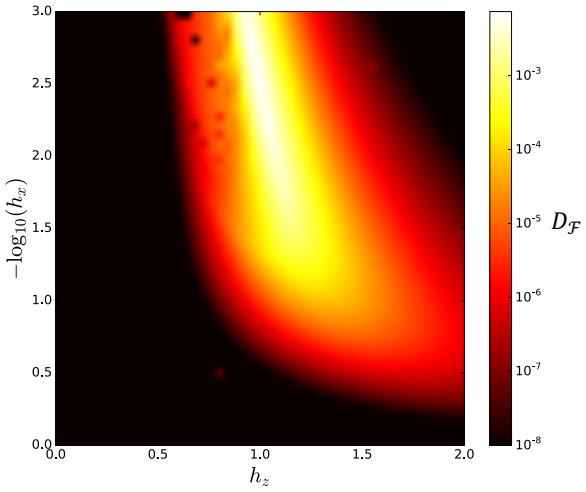

Figure 6.5: Interaction distance close to the critical point $(1, 0)$ for the FM case, where the longitudinal field is in log-scale. Infinitesimally close above the free line's critical point the interactions become a strongly relevant and $D_{\mathcal{F}}$ diverges. Impurities in the figure are attributed to local minima of $D_{\mathcal{F}}$.

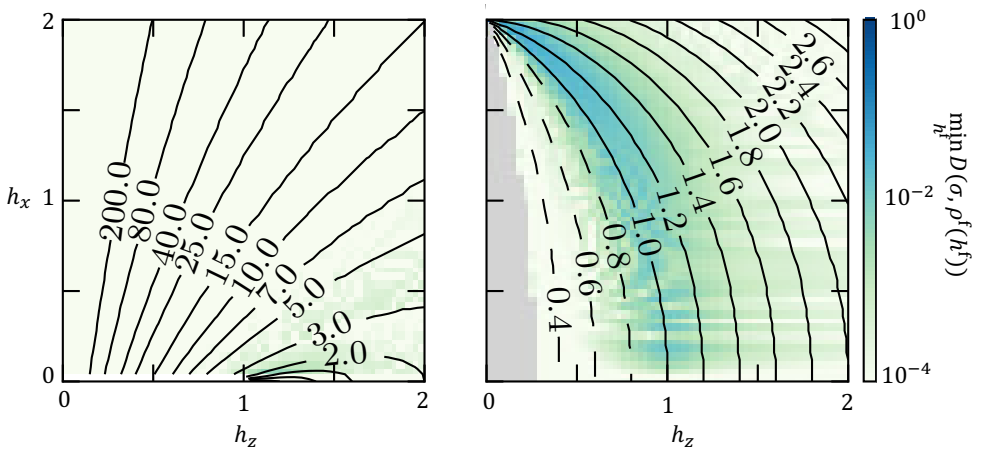

Figure 6.6: Mapping of $\sigma(h_z, h_x)$ to reduced ground states of the free line for FM (Left) and AFM (Right) model both at system size $L = 16$. Contours indicate the transverse-field h^{f}, dashed lines for those in the symmetry broken phase and solid otherwise (including the critical value $h^{\mathrm{f}} = 1$). The background colour plot gives the distance $\min_{h^{\mathrm{f}}} D(\sigma, \sigma^{\mathrm{f}})$ (log scale) signifying the success of the mapping. In this way the interacting system is given a description in terms of a free-fermion model. Unreliable data points due to unresolved ground state degeneracy is discarded (grey region).

6.5 Parafermionic Chains

For the quantum Ising chain studied in the previous section we found that the interaction distance, $D_{\mathcal{F}}$, is almost zero almost everywhere in the phase diagram. The natural question arising now is now what a simple example of a model is for which $D_{\mathcal{F}}$ is non-trivial in the thermodynamic limit or at least some stable fixed point of the model. Here we recall two facts. One, the size of the entanglement spectrum of a ground state composed of complex fermions is $2^{\min(|A|,|B|)}$, where 2 is the local Hilbert space dimension of a fermion and $|A|$ is the size of region A resulting from the bipartition. Second, there exist models comprising parafermions hopping on a chain which we choose as candidates for models that exhibit finite $D_{\mathcal{F}}$. The reason these models are considered is that they allow us to vary the rank of the the entanglement spectrum of their ground states at their topologically non-trivial fixed point. This is a result of their local Hilbert space not being in general a multiple of 2. Thus we expect that there will be instances where it is impossible for a given parafermionic entanglement spectrum to be matched with a free-fermion one leading to a non-trivial interaction distance.

As stated in section 6.4, the Ising model with a transverse field can be mapped to Kitaev's Majorana chain via the Jordan-Wigner transformation [130, 116]. Parafermionic chains are the $\mathbb{Z}_N$ generalisation of Majorana chains, which are obtained for $N = 2$. These $\mathbb{Z}_N$-spins are known as quantum clock or Potts models [131, 62]. The parachains are modelled by the Hamiltonian

$$H = \sum_j -f\gamma_j^{\mathrm{b}\dagger}\gamma_j^{\mathrm{w}} - \gamma_j^{\mathrm{w}\dagger}\gamma_{j+1}^{\mathrm{b}} + \mathrm{h.c.}, \tag{6.4}$$

where parafermionic operators γ_j satisfy $\gamma_j\gamma_k = \omega^{\mathrm{sgn}(k-j)}\gamma_k\gamma_j$, where $\omega = e^{i2\pi/N}$ the N-th root of unity. We also have $\gamma_j^\dagger = \gamma_j^{N-1}$ and $\gamma_j^N = 1$. It is obvious from these definitions that Majoranas correspond to $N = 2$. Recently, phase diagrams of such models have been mapped out numerically [132, 133, 134]. Note that this is not the most generic parafermion Hamiltonian as more terms can be added that respect the $\mathbb{Z}_N$ symmetry. Here however we choose to work with this simple case as our priority is to provide a simple model in properties of the interaction distance.

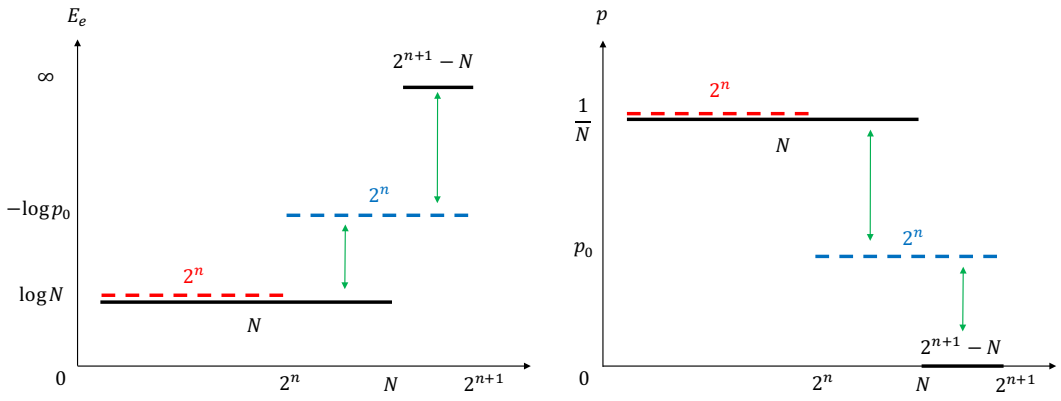

Figure 6.7: (Left) Flat spectrum $E^\flat(N)$ (solid black) and the entanglement energies $-\log \text{spec}(\sigma_{\text{guess}})$ (dashed). Green arrows denote the differences between levels that contribute to $D(\rho^\flat(N), \sigma_{\text{guess}})$.

In analogy with the Majorana case where the Hamiltonian respects fermionic parity, here the generalised $\mathbb{Z}_N$-version of parity, $Q = \prod_j \gamma_j^{\text{b}\dagger}\gamma_j^{\text{w}}$, is conserved. For open boundaries this leads to an N-fold degenerate ground state in the topological phase $|f| < 1$ and we again understand this in terms of parafermionic zero-modes localised at the ends of the chain. At the topological fixed point, $f = 0$, the parafermions at the ends completely decouple and the physics reduces to that of two parafermions or one-clock (on a site j). For periodic boundaries, unique ground state gives an N-fold degenerate entanglement spectrum [135], reflecting the N-fold degenerate ground state when the entanglement cut becomes a physical cut and can be understood in terms of parity compatibility between regions A, B into which we have bi-partitioned the chain. For $f > 0$ the ground state acquires a finite correlation length and we will explore the behaviour of the interaction distance away from the following, as well.

6.5.1 Guess for Optimal Free State

We denote an N-fold degenerate entanglement spectrum as $E_e^\flat(N)$ and a density matrix with such a flat spectrum is symbolised $\rho^\flat(N)$. Now we make a guess for

the optimal free state, σ_{guess}, such that $D(\rho^\flat(N), \sigma_{\text{guess}}) = D_{\mathcal{F}}(\rho^\flat(N))$. Define $n \in \mathbb{N}$ as the greatest natural number to not violate $2^n \leq N$. We conjecture that the optimal free spectrum to a N-flat spectrum is

$$\text{spec}(\sigma_{\text{guess}}) = \big(\underbrace{N^{-1}, \ldots, N^{-1}}_{2^n}, \underbrace{p_0, \ldots, p_0}_{2^n}\big), \tag{6.5}$$

where $p_0 = \frac{1}{2^n} - \frac{1}{N}$ for normalisation.

The thinking behind this form of σ_{guess} is as follows. Recall the free fermion entanglement structure $\text{spec}\,(\sigma_{\text{guess}}) = e^{-E_e^0} \otimes_{i=1} (1, e^{-\epsilon_i})$. The conjecture is it is optimal to match as many levels of $E_e^\flat(N)$ as possible by using zero-modes, $\epsilon_i = 0,\ i = 1, \ldots, n$, with background entanglement energy $E_e^0 = \log N$. Then, the remaining mode is fixed by normalisation of σ_{guess} to $\epsilon_{n+1} = \log \frac{2^n}{N - 2^n}$ and creates the 2^n entanglement levels at $-\log p_0$.

Note that $E_e^\flat$ needs to be padded with ∞s, or equivalently $\text{spec}(\rho^\flat)$ is padded with zeros so that the sizes of $\rho^\flat$ and σ_{guess} are equal. Then the interaction distance arises from the unmatched levels. In particular, there are two contributions to $D(\rho^\flat, \sigma_{\text{guess}})$. The first is from the entanglement levels $E^\flat_{e\,2^n+1} \ldots E^\flat_{e\,N}$ mismatching the corresponding levels of σ_{guess} at value $-\log p_0$. The second is from the tail of the levels ${\sigma^\flat}_{N+1} \ldots {\sigma^\flat}_{2^{n+1}}$. The matching is illustrated in Fig. 6.7.

In the trivial case where the flat spectrum is actually of power-of-two size, $N = 2^n$ for some $n \in \mathbb{N}$, then $\rho^\flat(N)$ can be reproduced entirely by zero-modes $\epsilon_j = 0,\ j = 1, \ldots, n$, and thus the spectrum is free, $D_{\mathcal{F}}(\rho^\flat(2^n)) = 0$. In these cases, the entanglement spectrum is equivalent to that of n stacked Kitaev chains.

6.5.2 Form of the Interaction Distance

Plugging $\rho^\flat(N)$ and the corresponding σ_{guess} in the trace distance we obtain

$$D(\rho^\flat, \sigma_{\text{guess}}) = 3 - \frac{N}{2^n} - \frac{2^{n+1}}{N}. \tag{6.6}$$

To find for which N the we have the maximum of (6.6), we make an analytic parametrisation of the interval $2^n \leq N \leq 2^{n+1}$. We parametrise N between two consecutive powers of 2 with a parameter $\alpha \in [0, 2]$ such that $N = \alpha 2^n \in \mathbb{R}$, yielding $D(\alpha) = 3 - \alpha - \frac{2}{\alpha}$. By setting $\partial_\alpha D(\alpha) = 0$ we find

$$\alpha_{\max} = \sqrt{2}\ , \quad \text{with} \quad D^{\max}(\rho^\flat, \sigma_{\text{guess}}) = 3 - 2\sqrt{2}. \tag{6.7}$$

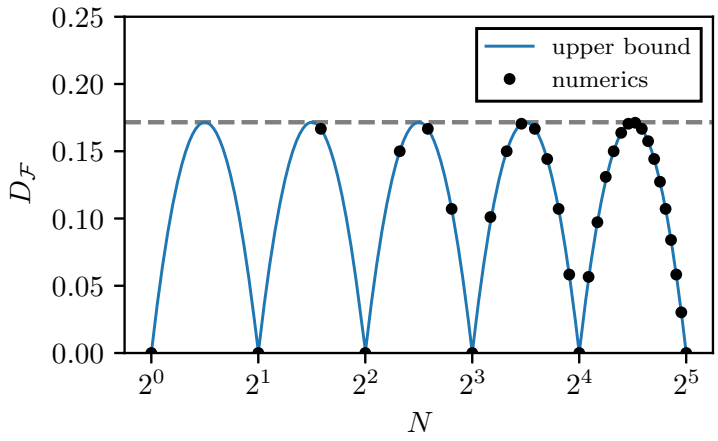

Figure 6.8: Interaction distance, $D_{\mathcal{F}}(\bar{\rho})$, for flat spectra $E_e^\flat(N)$. The blue line is $D(\rho^\flat, \sigma_{\text{guess}})$ given in (6.6) with maximal value $3 - 2\sqrt{2}$ (dashed). The dots are numerical results for $D_{\mathcal{F}}(\rho^\flat(N))$. Data up to $N = 2^8$ is shown in Appendix E.5.

Because $N \in \mathbb{N}$ and $\alpha_{\max} = \sqrt{2}$ is irrational, we can approximate $D^{\max}$ in the $N \to \infty$ limit, i.e. when $\mathbb{Z}_N \to U(1)$ for the parafermions.

Formally, what we have is just an upper bound, $D_{\mathcal{F}}(\rho^\flat) \leq D(\rho^\flat, \sigma_{\text{guess}})$, since we have not proved that our guess is indeed the correct one. In Fig. 6.8 we plot $D(\rho^\flat, \sigma_{\text{guess}})$ as well as $D_{\mathcal{F}}(\rho^\flat(N))$ computed numerically with Monte-Carlo basin-hopping as a function of N. The numerical results always converge on the conjectured form (6.6) for a large enough number of basins and we never find a value below it. Therefore, we take this numerical evidence to confirm our conjecture that $\sigma = \sigma_{\text{guess}}$ and thus indeed

$$D_{\mathcal{F}}(\rho^\flat) = D(\rho^\flat, \sigma_{\text{guess}}), \tag{6.8}$$

and parafermions on a chain behaving according to the simple Hamiltonian (6.4) provide an example of a model with non-trivial interaction distance. In other words, the correlations in the ground state cannot even effectively be described in terms of free fermions, constituting it a purely interacting system.

Some comments now are in order. The maximal value $D_{\mathcal{F}}^{\max}(\rho^\flat) = 3 - 2\sqrt{2}$ coincides with the numerical value for $D_{\mathcal{F}}^{\max}(\rho^\flat)$ obtained by maximising $D_{\mathcal{F}}$ (see Appendix B.6). We thus conclude that the parafermion chains can achieve $D_{\mathcal{F}}$ arbitrary close to $D_{\mathcal{F}}^{\max}$ for appropriate group-order $N \in \mathbb{N}$. Moreover, we observe

in Fig. 6.8 a log-periodic pattern, that is $D_{\mathcal{F}}(\rho^\flat(2N)) = D_{\mathcal{F}}(\rho^\flat(N))$. This again is a special case of our numerically supported conjecture $D_{\mathcal{F}}(\rho) = D_{\mathcal{F}}\left(\frac{1}{2}(\rho \oplus \rho)\right)$ (see Appendix B.6). Finally, we point to analytical results in Ref.[128] showing that $D_{\mathcal{F}}(\rho^\flat(3)) = \frac{1}{6}$, as well as that $D_{\mathcal{F}}(\rho^\flat(2^{n+1}-2)) = D_{\mathcal{F}}(\rho^\flat(2^n-1))$ by using the entanglement renormalisation argument, i.e. by integrating out the lowest lying single-body entanglement energy (see Appendix of Ref. [136]). We have confirmed these results with our numerical maximisation of the interaction distance.

6.5.3 Off the Fixed Point and Excited States

We now briefly examine what the case $f > 0$. Off the fixed point the system acquires a correlation length ξ, the degeneracy of the ground state for open boundaries splits with a gap exponentially suppressed by the system size L, and the intuition is the same as for Kitaev's wire. The same argument follows for the virtual edge states after a bi-partition. That is, if the partitions are large enough $L_{|A,B|} \gg \xi$ they do not overlap through the bulks of A, B and the degeneracy in the entanglement energies is protected. This leads to $D_{\mathcal{F}}$ being stable away from the fixed point and its value becoming more robust under system size scaling. An illustration of this effect studied with exact diagonalisation performed is presented in Appendix E.5 for $\mathbb{Z}_3$ and $\mathbb{Z}_4$. Also, it is important to note that $D_{\mathcal{F}}$ depends only on N and not the position of the cut. When there is a finite correlation length then this statement is true for reasonably large partitions.

We also can draw conclusions about excited states on the fixed point. For $f = 0$ the problem reduces to a one-clock and so excited states are all combinations of rotations of the individual clocks and each eigenstate belongs to a parity sector. The entanglement spectrum arises from the loss of knowledge about the parity when we cut through a clock. Thus it again is an N-fold degenerate spectrum and the analysis that was done for the ground state holds here again. Thus, the $\mathbb{Z}_{2^n}$-parachains have $D_{\mathcal{F}} = 0$ for all eigenstates at the fixed point. However, at $f > 0$, the excited states of $\mathbb{Z}_{N\neq 2^n}$ in general have non-zero $D_{\mathcal{F}}$, with the exception of single-clock excitations above the ground state, which remain approximately free for $f > 0$ close to the fixed point. This is consistent with the models, e.g.,

$\mathbb{Z}_4$, being non-integrable for general f [135], although its ground state remains Gaussian.

6.5.4 Equivalent Interaction Distance Leads to Equivalent States

Finally, inspired by the observation that at the fixed point the ground state of a $\mathbb{Z}_{2^n}$ chain has equivalent entanglement with that of n decoupled $\mathbb{Z}_2$ chains for any cut, we comment on the equivalence between the states. The intriguing element in this is that the group $\mathbb{Z}_{2^n}$ is not in general isomorphic to $\times_{i=1}^{n}\mathbb{Z}_2$. And even more generally, we can confirm that same equivalence holds for parachains with groups $\mathbb{Z}_{pq}$ and $\mathbb{Z}_p \times \mathbb{Z}_q$. We stress here that this equivalence holding for any cut is a stronger than what is allowed by the definition of $D_{\mathcal{F}}$; the effective free-fermion modes on which the optimal free state is defined are allowed to be non-local inside the partitions but they can be different modes for different cuts, in general. Here however we have that for any cut we obtain the same σ.

In Ref. [136], the language of matrix product states (MPS) is employed in order to prove that at the fixed point there exists in fact a local unitary (tensor product of site-local unitaries) which maps the ground state of a $\mathbb{Z}_4$-chain to that of a $\mathbb{Z}_2 \times \mathbb{Z}_2$-chain. This is consistent with the fact that no symmetry-respecting unitary can map between distinct symmetry-protected topological phases [37] because our unitary need not respect the symmetry of either chain. We also expect the mapping for the ground state to hold off the fixed point as well, since our numerical results suggest that the interaction distance is stable for $f > 0$.

Regarding excited states, it is shown that if the local unitary that performs the mapping for the ground state is used on them, then the equivalence stops holding. We thus conclude that a single unitary cannot be chosen to map all the eigenstates of the $\mathbb{Z}_p \times \mathbb{Z}_q$ chain onto the $\mathbb{Z}_{pq}$ chain, and that each eigenstate requires a different unitary, even if their corresponding entanglement spectra are equivalent.

6.6 String-nets

In our final section we will discuss the interaction distance in the context of string-nets [137, 138]. Beginning with Abelian $\mathbb{Z}_N$ string-nets we see that the results obtained for the $\mathbb{Z}_N$ parafermion chains in the previous section apply here as well. We conclude with a brief study of non-Abelian string-nets and view our results through the lens of understanding that we shaped by studying Kitaev's honeycomb.

String-nets are 2D discrete fixed-point models of topological quantum field theories (TQFTs). Their Hamiltonians are of the stabiliser formalism and are defined on a honeycomb lattice and by construction they support topological order and consequently anyonic excitations. It is useful here to keep in mind the gauge part of Kitaev's honeycomb as the analogy is enough to understand what is needed for our purposes. On the links of the honeycomb, i, anyonic "charges", $\mathcal{J}_i$, are defined as irreducible representations of a finite group of our choice and this group determines the topological order of the theory. We can view each trivalent vertex of the lattice as a fusion process, $\mathcal{J} \times \mathcal{J}' \to \mathcal{J}''$, where two anyons fuse to a third one according to the fusion rules of the group. Similarly to Kitaev's honeycomb, whose gauge part is a superposition of closed vortex loops, the ground state of a string-net model is a superposition of closed loops carrying certain charges, and once a loop is opened into a string, the end-points act as anyonic excitations.

6.6.1 String-net Entanglement Spectrum

We create a bipartition of the honeycomb. The entanglement spectrum, which here we call just the spectrum of the reduced density matrix, $p = \mathrm{spec}(\rho_A)$ is given by [139]

$$\rho_a = \frac{\prod_{i \in j} d_{\mathcal{J}_i}}{\mathcal{D}^{2(|\partial A| - b_0)}}, \tag{6.9}$$

where j labels charge configurations along the boundary, ∂A, which have the vacuum as a fusion channel, and $\mathcal{J}_i$ is an element of the boundary configuration j. The number of components of $|\partial A|$ is denoted b_0, and we will be concerned with cases for which $b_0 = 1$. In particular, a cut so that A is deformable to a disk

is shown in Fig. 6.9. We can now directly evaluate the entanglement spectra of any string-net models, Abelian or non-Abelian, and for any partition [139]. In Appendix E.6 we provide a simple example for the calculation of (6.9) for Abelian and non-Abelian groups, which we study in the following.

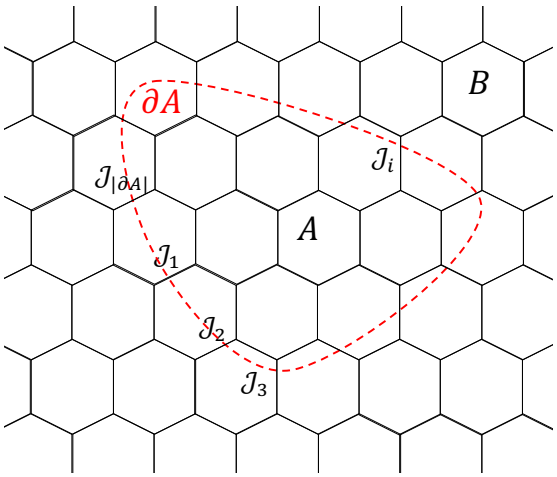

Figure 6.9: Bipartition of a 2D string net. Charges on the boundary (red dashed) are labelled $\mathcal{J}_i$, $i = 1, \ldots, |\partial A|$. The ground state demands that they fuse to the vacuum.

6.6.2 Abelian String-nets

We begin by considering string-nets endowed with the Abelian group $\mathbb{Z}_N$. All charges, $\mathcal{J} = 0, 1, \ldots, N-1$, have trivial quantum dimension $d_{\mathcal{J}} = 1$ and thus $\mathcal{D} = \sqrt{N}$. The calculation of the entanglement spectrum entails the enumeration of charge configurations on ∂A that fuse to the vacuum, which here we choose to be the element 0. Then, these configuration are determined then by the condition $(\sum_i \mathcal{J}_i) \,\mathrm{mod} N = 0$. Consequently, Eq. (6.9) tells us that the entanglement spectrum for any bipartition is a flat one, $E_e^{\flat}(N^{|\partial A|-b_0})$. Hence, we can refer to our result for the interaction distance in Eq. (6.6) obtained in the context of parafermion chains. We underline here an important difference between the 1D parafermion chains and the Abelian string-nets. The entanglement spectrum of the former does not depends on the cut's position. However, for string-nets, the entanglement spectrum depends on the length and the topology of the cut, property which we will put into context in the following.

Free Abelian String-nets

When $N = 2^n$ we have $D_{\mathcal{F}} = 0$ for any partition and the correlations in the ground state admit a free-fermion description in terms of zero-modes. This might, at first glance, be a surprising result as anyons are expected to emerge in interacting systems. Nevertheless, the corresponding free states are not necessarily local as discussed in paragraph 3.3.3. While this analysis is performed for the correlations in the ground state, the energy spectrum of these models is not necessarily be given by occupying fermionic single-body modes.

To stretch the analogy with $\mathbb{Z}_{2^n}$ string-nets whose entanglement spectrum is the same as that obtained from n stacked Kitaev chains, the entanglement spectrum obtained from $\mathbb{Z}_{2^n}$ string-nets can be recreated by n layers of $\mathbb{Z}_2$ string-nets. Note that this is the case for any cut. Furthermore, as local unitaries map between the ground states of $\mathbb{Z}_4$ and $\mathbb{Z}_2 \times \mathbb{Z}_2$ parachains, we expect there to be local unitaries that map between the analogous string-nets. This again is consistent with the fact that these topological orders cannot be adiabatically connected [41], since we do not require this unitary to map all eigenstates to each other, but only one of them, namely the ground state. A different local unitary, however, is expected to exist for each pair of eigenstates between which one wishes to map. Indeed, the excited states of $\mathbb{Z}_{2^n}$ string-nets are again free. The only thing that changes is that the fusion condition for the boundary charges has to match the charges that are enclosed by $|\partial A|$, with the vacuum being the corresponding special case for the ground state.

An interesting fact about the $N = 2$ case is that it corresponds to the Toric Code [29, 28], which is also obtained as the $J \ll 1$ limit of Kitaev's honeycomb [13]. As we saw in section 4.7, Kitaev's honeycomb gives rise to two independent contributions to the entanglement from a bi-partition, one from free fermions and one from a $\mathbb{Z}_2$ gauge field. The latter being reproducible with entanglement zero-modes is crucial to deem the ground state free, which is consistent with interaction distance being zero for the $\mathbb{Z}_2$ string net.

Non-Free Abelian String-nets

Finally, for string nets with $N \neq 2^n$, we have $D_{\mathcal{F}} > 0$ for any cut and its value depends on $|\partial A|$. To see what this entails we argue as follows. We recall that $D_{\mathcal{F}}(\rho^{\flat})$ is $\log_2$ periodic and that the degeneracy of the entanglement spectrum is N^k, where we defined $k = |\partial A| - b_0 \in \mathbb{N}$. Let us see what values $D_{\mathcal{F}}$ takes when we increase k. If $N \neq 2^n$ then $\log_2 N \in \mathbb{R} \setminus \mathbb{Q}$. and we define $a = k \log_2 N \mathrm{mod} 1$ which parametrises the interval $[0, 1]$ under the $D_{\mathcal{F}}$ curve periodically. Then, we see that if one takes k-many steps of irrational length, $\log_2 N$, one samples a uniformly, $P(a) = 1$. Thus values of $D_{\mathcal{F}}$ are sampled densely, and the distribution obtained for the interaction distance, $P(D_{\mathcal{F}})$ is given in the Appendix of Ref. [136]. In other words, for Abelian string-nets for given N there exist partitions that asymptotically maximise $D_{\mathcal{F}}$ for all $N \neq 2^n$. Another way to understand this is to consider that since we are at a fixed point, boundary length's don't matter and what is important is the topology of the boundary. The case where k is fixed and the group order, $N \in \mathbb{N}$, is varied is also studied. For a value of k, we imagine that k-many steps of irrational length $\log_2 N$ are taken, but the length is different for each N-choice. This is studied in detail by in the Appendix of Ref. [136] where it is shown that a is again sampled uniformly in $[0, 1]$. Thus, we conclude that a $\mathbb{Z}_N$ string net is either free or not free with no intermediate options.

6.6.3 Non-Abelian String-nets

We next consider non-Abelian string-nets with charges taking values from the group $\mathrm{SU}(2)_k$, $k \geq 2$ as $\mathcal{J} = 0, \frac{1}{2}, 1, \ldots, \frac{k}{2}$ and the fusion rules are given by $\mathcal{J} \times \mathcal{J}' = \sum_{\mathcal{J}''=|\mathcal{J}-\mathcal{J}'|}^{\min(\mathcal{J}+\mathcal{J}', k-\mathcal{J}-\mathcal{J}')} \mathcal{J}''$. The level $k = 2$ gives rise to Ising anyons, which have exchange statistics similar to Majoranas and occur in Kitaev's honeycomb model. Fusing Ising anyons σ_j and σ_k is equivalent to measuring the parity of two Majoranas $i\gamma_j\gamma_k$, and assigning the ± 1 outcomes to the anyonic vacuum 1 or the fermion ψ. For an example using Ising anyons see Appendix E.6. For $k = 3$ we have Fibonacci anyons, which are universal for quantum computation [140, 2]. Here we cut around one vertex on the honeycomb lattice on which the string-net is defined, so that $|\partial A| = 3$, and examine how the interaction distance of

the ground state behaves with the group level, k. We find that $D_{\mathcal{F}} \neq 0$ for all $k \leq 20$, as shown in Appendix E.7. Hence, it is not possible to find a free fermion description of these non-Abelian string-net models.

However, it is known that Kitaev's honeycomb supports Ising anyons and we found that for this model we have $D_{\mathcal{F}} = 0$ for any eigenstate. The reconciliation happens when we realise that Kitaev's honeycomb is chiral and not at a fixed point. Furthermore, it may be that eigenstates are free, but the modes in which they are free in general differ among eigenstates. More importantly, the properties of the anyons arise under braiding, and braiding is achieved when one interpolates between fixed vortex-sectors.

Finally, in contrast with Abelian string-nets, the topology of the entanglement cut, ∂A, affects the entanglement spectrum. In particular for a 2D string-net, when region A is equivalent to a disk, it is only the fusion rules that determine the entanglement spectrum and the braiding properties do not come into play. However, there exist 3D string-nets, called Walker-Wang models [141]. Now ∂A can be deformable to spherical surface, or a toroidal surface. Computing numerically $D_{\mathcal{F}}$ for various k-levels for the two cases we observe that indeed there is a difference, something that does not occur for the Abelian case.

6.7 Summary

In conclusion, we have employed the diagnostics of monogamy and interaction distance on ground states of interacting models. For the SSHH model we found that the monogamy signature remains robust as long as the edge states are localised. For the quantum Ising chain, we compute the interaction distance over the phase diagram. Then, the ground state at every point in the phase diagram is mapped to the free line. In this way, the mapping is accurate when the interaction distance is almost equal to zero. Therefore, we have found a free parent Hamiltonian for ground states whose spectrum is free according to the interaction distance. Then we generalised the local degrees of freedom to parafermions. Interestingly we found that the interaction distance approaches its maximal value for certain parafermion chains, rendering them purely interacting. For Abelian string-nets

we found that they either are free or there exists a cut for which the interaction distance is approximately maximal. On the other hand, the correlations in non-Abelian string-nets cannot be desribed by free fermions.

Finally, we mention that we have obtained preliminary results on entanglement spectra of the integer and fractional quantum Hall states. The integer case for filling factor 1 shows $D_{\mathcal{F}} = 0$ to numerical precision with respect to free fermions, as expected, since this physics can be reproduced by Haldane's honeycomb model. The fractional cases are considered purely interacting. For filling factors $\frac{1}{2}$ for bosons and $\frac{1}{3}$ for fermions, we obtain a decaying $D_{\mathcal{F}}$ with system size, compatible with the composite fermion effective picture also confirmed by Ref. [142]. There, a similar approach to ours is taken, where the entanglement spectrum of the fractional state is constructed as a weighted combination of spectra of integer states, with the weights as variational parameters.

Appendix A

Correlations and Topological Quantum Matter Appendix

A.1 Single-particle Entanglement Entropy

Consider the mixed gaussian state $\rho = \frac{e^{-H_A^\flat}}{Z}$, where $Z = \mathrm{tr} e^{-H_A^\flat}$, representing the reduced density matrix of region A and $H_A^\flat = \sum_{ij\in A} h_{ij}^\flat f_i^\dagger f_j$ is the bland-flattened free-fermion Hamiltonian restricted to region A. Peschel proved that the eigenvalues λ_k of the sub-matrix C_A, are related to the eigenvalues ϵ of $h_A^\flat$ via [25]

$$e^{-\epsilon_j} = \frac{\lambda_j}{1-\lambda_j}. \tag{A.1}$$

We can use this relation to derive the expression of the entropy for free systems by writing the state in terms of the normal modes of A as $\rho = \otimes_k \rho_k$ with $\rho_k = \frac{e^{-\epsilon_k n_k}}{Z_k}$where $Z_k = \mathrm{tr}(e^{-\epsilon_k^A \hat{n}_k})$ and n_k is the population of the k-th mode annihilated by $\tilde{f}_k$. Since each mode is independent the entropy is additive over their contributions $S = -\sum_{k,n_k} p_k^{n_k} \log p_k^{n_k}$, where $p_k = \frac{e^{-\epsilon_k}}{1+e^{-\epsilon_k^A}}$. Using (A.1), the von Neumann entropy (2.19) gives

$$S = -\sum_k (1-\lambda_k)\log(1-\lambda_k) + \lambda_k \log \lambda_k. \tag{A.2}$$

If the Hamiltonian is written in terms of Majoranas, then (2.16) inherits a $\frac{1}{2}$ factor to take care of double-counting degrees of freedom due to the Majorana reality condition. This can be seen as follows. Considering N fermions with $2N$ Majoranas defined as $\tilde{a}_j = \tilde{f}_j^\dagger + \tilde{f}_j$ and $\tilde{b}_j = \frac{1}{i}(\tilde{f}_j - \tilde{f}_j^\dagger)$ we find their correlations $\tilde{C}_{jk} = \langle \tilde{\gamma}_j \tilde{\gamma}_k \rangle$, where $\gamma = a, b$. Computing the correlations we find $\langle \tilde{a}_j \tilde{a}_k \rangle = \langle \tilde{b}_j \tilde{b}_k \rangle = \delta_{jk}$ and $\langle \tilde{a}_j \tilde{b}_k \rangle = -i(2\lambda_j - 1)\delta_{jk}$. Thus the correlation matrix in the Majorana basis is

$$\tilde{C} = \frac{1}{2} \begin{bmatrix} 1 & -i(2\lambda_n - 1) \\ i(2\lambda_n - 1) & 1 \end{bmatrix}, \tag{A.3}$$

with eigenvalues t_k given by $(\frac{1}{2} - \mu_k) = \pm(\lambda_k - \frac{1}{2})$, which implies that the eigenvalues of the correlation matrix C and the covariance matrix $\tilde{C}$ are related by $t_k = \lambda_k, (1 - \lambda_n)$. Thus if one inserts the ts in (2.16) to calculate the entropy, one obtains twice the value that one would obtain by inserting the λs, and hence the need for the $\frac{1}{2}$ factor in the entropy.

A.2 Many-Body Entanglement Spectrum

Here we present ways of obtaining the entanglement spectrum of a many-body state. A many-body fermionic state $|\Psi\rangle$ on L sites can be written as a convex combination of Fock basis vectors $|b\rangle$, $b = 1, 2, \ldots, 2^L$,

$$|\Psi\rangle = \sum_b a_b |b\rangle \tag{A.4}$$

where b labels binary words $n_1 n_2 \ldots n_L$ representing the occupations on the sites. Now assume that we have enumerated the sites so that they respect the bipartition such that binary words $n_1 n_2 \ldots n_{\partial A}$ represent occupations in A and are labelled by the Fock basis $|b_A\rangle$, and similarly for region B. Now we write the state as

$$|\Psi\rangle = \sum_{b_A} \sum_{b_B} M_{b_A b_B} |b_A b_B\rangle , \tag{A.5}$$

where M is the *entanglement matrix*. Now the entanglement spectrum can be obtained in two ways. We can create the pure density matrix $|\Psi\rangle\langle\Psi|$. In Fig.A.1 we represent the reduced density matrix obtained by tracing out the B-basis.

Then the entanglement spectrum is simply obtained by (2.18). On the other hand we can reshape the vector $|\Psi\rangle$ into the $2^{|A|} \times 2^{|B|}$ entanglement matrix, M, and perform a singular value decomposition to get its singular values $\mathrm{svd}(M)$. Since $\rho = M^\dagger M$, we have that $\mathrm{spec}(\rho) = \mathrm{svd}(M)$. Of course, if the basis is ordered in a different way, we can always compute the elements of the entanglement matrix as $M_{b_A b_B} = \langle b_A b_B|\, b\rangle$.

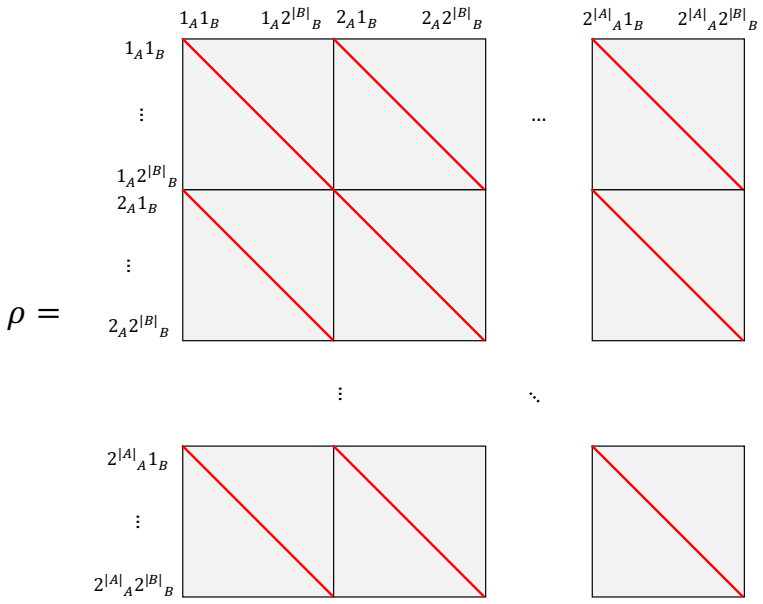

Figure A.1: Depiction of reduced density matrix $\rho = \mathrm{tr}_B\, |\Psi\rangle\langle\Psi|$. The rows and columns are spanned by the binary words $b_A b_B$ corresponding to the Fock basis vectors $|b_A b_B\rangle$. The $2^{|B|} \times 2^{|B|}$ grey blocks are in general dense and their traces (red lines) are the elements of the resulting $2^{|A|} \times 2^{|A|}$ matrix ρ.

For quantum spin or clock models, the Hamiltonian is constructed as usual as a sum of terms of tensor products of the local spin/clock operators with weights the corresponding couplings. Then diagonalising the Hamiltonian matrix, the lowest eigenvector is the ground state. We can then use the reshape method to form M and then obtain the entanglement spectrum.

Appendix B

Entanglement Diagnostics

B.1 Jordan-Wigner of Two-Mode State

Let σ be two-fermion density matrix, with corresponding covariance matrix given by (3.3). Applying a Jordan-Wigner transformation on the two-fermion system the state can be written as [143]

$$\sigma = \frac{\mathbb{I}}{4} + \frac{1}{4}\begin{bmatrix} \eta_{11} & 0 & 0 & \eta_{14} \\ 0 & \eta_{22} & \eta_{23} & 0 \\ 0 & \eta_{32} & \eta_{33} & 0 \\ \eta_{41} & 0 & 0 & \eta_{44} \end{bmatrix}, \tag{B.1}$$

with $\eta_{11} = -(a+d)+(ad+bc)$, $\eta_{22} = (a-d)-(ad+bc)$, $\eta_{33} = -(a-d)-(ad+bc)$, $\eta_{44} = (a+d)+(ad+bc)$, $\eta_{14} = \eta_{41} = -b-c$, and $\eta_{23} = \eta_{32} = -b+c$.

For σ to be pure and maximally entangled we substitute $a = d$ and $b = c$. Using also that the squared eigenvalues of Ξ_A plus the squared singular values of Ξ_{AB} sum to unity we have $b = \sqrt{1-a^2}$, and σ depends only on a.

B.2 Monogamy Bound

From the relationship between the entanglement of formation and the tangle [54], one finds that $E_F^2 \leq \tau \log^2 2$ and $E_F \geq \tau \log 2$. Then, if the state of modes 1 and 2 is of the form $\sigma = (1-\varepsilon)\omega + \varepsilon\eta$ in terms of a maximally entangled pair ω then it follows that

$$E_F(1:2) \geq (1-\varepsilon)\log 2, \tag{B.2}$$

making use of the convexity of E_F and taking the convention that $E_F(\omega) = \log 2$. The monogamy of entanglement property derived in Ref. [55] reads as

$$\tau(1:2) + \tau(1:3) + \cdots + \tau(1:n) \leq 1, \tag{B.3}$$

from which it follows that

$$\begin{aligned} \sum_{j=3}^{N} E_F(1:j)^2 &= \log^2 2 \sum_{j=3}^{N} \tau(1:j) \\ &\leq \log^2 2 \, (1 - \tau(1:2)) \\ &\leq \log^2 2 - E_F(1:2)^2 \\ &\leq \log^2 2 \left(1 - (1-\varepsilon)^2\right). \end{aligned} \tag{B.4}$$

B.3 Entropy Lower Bound

In order to show the validity of (3.11) it is instructive to first consider a two-mode problem, with quantum state σ. The covariance matrix of σ has again the form

$$\Xi = \begin{bmatrix} 0 & a & 0 & b \\ -a & 0 & c & 0 \\ 0 & -c & 0 & d \\ -b & 0 & -d & 0 \end{bmatrix} = \begin{bmatrix} \Xi_A & \Xi_{AB} \\ -\Xi_{AB}^T & \Xi_B \end{bmatrix}. \tag{B.5}$$

On using the Jordan Wigner transformation and the concavity of the von-Neumann entropy, one finds that

$$S(\sigma) \geq \frac{1}{2}(|c+b| + |c-b|). \tag{B.6}$$

The right hand side, in turn, can be lower bounded by $\|\Xi_{AB}\|_2^2/2$. The generalisation of this to a bi-partitioned N mode fermionic system with even N can be performed by making use of the fact that by means of suitable special orthogonal mode transformations $O_A, O_B, U_A, U_B \in SO(N)$ local to A and B, one can bring the off-diagonal block Γ_{AB} into the form

$$(O_A \oplus O_B)\Gamma_{AB}(U_A \oplus U_B)^\dagger = \bigoplus_{j=1}^{N/2} \begin{bmatrix} 0 & b_j \\ c_j & 0 \end{bmatrix}. \tag{B.7}$$

Therefore,

$$S(\rho_A) \geq \frac{1}{2}\|\Gamma_{AB}\|_2^2 \log 2, \tag{B.8}$$

A related lower bound to the entropy in terms of Bogoliubov quasiparticles has been presented in Ref. [27].

B.4 Optimisation Details for the Interaction Distance

The optimisation to find σ and $D_{\mathcal{F}}$ in (3.18) is performed by Monte Carlo basin-hopping [144]. A Nelder-Mead algorithm finds a local minimum in the landscape of the cost function, in which case is the trace distance, thus defining a basin. Then another basin is randomly chosen by a hopping of empirically specified step size and its local minimum is found. The more basins we allow, the more minima are collected, and the probability that we obtained the global one is higher.

Before the optimisation beings, we need to provide an initial guess for ϵ, and we describe it as it was implemented by Turner. Most important during this step is the size of the initial guess, i.e. how many single-body energies ϵ are going to be the variational parameters of the minimisation. The initial guess for an input entanglement spectrum E_{e}, consisting of energies $E_{\mathrm{e}1} < E_{\mathrm{e}2} < E_{\mathrm{e}3} < \ldots$, with a background entanglement energy $E_{\mathrm{e}0}$ ensuring normalisation. First we choose an entanglement energy cut-off E_e^{coff}. First we take E_1 and E_2 and subtract them from $E_{\mathrm{e}0}$ to produce the single-particle levels ϵ_1 and ϵ_2. Then we generate the four many-body levels out of these ϵs according to (3.14) and discard those that exceed E_e^{coff}. If $|E_{\mathrm{e}3} - (\epsilon_1 + \epsilon_2)| \leq E_{\mathrm{tol}}$, where E_{tol} is a tolerance we specify, then we mark level $E_{\mathrm{e}3}$ as matched. We iterate this process by taking the lowest unmatched level in the spectrum and subtracting $E_{\mathrm{e}0}$ to produce a new single-particle level ϵ_k. Then we again generate, according to (3.14), the many-body energies caused by the inclusion of ϵ_k to our set of single particle levels, discard those above E_e^{coff}, and mark as matched the E_{e} levels that are E_{tol}-close to them. The process halts when all of the input spectrum is either matched or included to the single-particle set.

B.5 Efficiency of $D_{\mathcal{F}}$

Finally, the calculation of $D_{\mathcal{F}}$ is a search problem. Its runtime complexity is polynomial in its input, i.e. the number, $|\epsilon|$, of entanglement levels. This is performed efficiently by using well known minimisation methods as mentioned above (B.4). Furthermore, considering that region A is a disk (reducing to a line interval in 1D) and symbolising the correlation length with ξ, we have the following for the runtime T. In 1D, for gapped states $|\epsilon| = \text{const.}$ and for gapless states $|\epsilon| \sim L$, and thus typically $T \sim \text{poly}(\log L)$. In dD, we have for gapped states $|\epsilon| \sim \exp \xi^{d-1}$ due to the area law leading to $T \sim \text{poly}(|\epsilon|^{d-1})$, while gapless states have a logarithmic correction [145] so that $|\epsilon| \sim \exp \xi^{d-1} \log \xi$ giving $T \sim \text{poly}(|\epsilon|^{d-1} \log \xi)$. Thus, since T is polynomial in the number of variational parameters, we can call it the optimisation efficient. Note that providing a good initial guess to the optimisation significantly reduces T. The construction of the initial guess is described above (B.4).

B.6 Properties of $D_{\mathcal{F}}$ for Generic States

In this section we present numerical evidence for conjectures regarding the interaction distance. First, we provide results supporting that for any input entanglement spectrum which is doubly degenerate the interaction distance is the same as for the spectrum without the degeneracy. Second, we present evidence for the conjectured maximal value for the interaction distance. Finally, we explore the distribution of the interaction distance over random states and pose open questions of future work.

B.6.1 Numerical Evidence for the Degenerate Spectrum Conjecture

Let ρ represent a generic diagonal density matrix. The random ρ is simply a random probability distribution, which albeit an improper way to sample states, it is sufficient for our purposes here. Its doubly degenerate version, $\frac{1}{2}(\rho \oplus \rho)$, can be interpreted as the result of adding a zero-entanglement-energy in the

system, where entanglement energy is defined as the negative logarithm of a probability [43]. This becomes clear when considering that each member of a degenerate pair of eigenvalues corresponds to the zero-mode being occupied or not. We compute $D_{\mathcal{F}}^{\text{diff}} = D_{\mathcal{F}}(\rho) - D_{\mathcal{F}}(\frac{1}{2}(\rho \oplus \rho))$ for random diagonal density matrices. The distribution $P(D_{\mathcal{F}}^{\text{diff}})$ is peaked at zero indicating the validity of the zero-mode conjecture, as shown in Fig.B.1 (Top). The peak is more prominent when the number of basins is increased. Note that $D_{\mathcal{F}}(\frac{1}{2}(\rho \oplus \rho)) \leq D(\frac{1}{2}(\rho \oplus \rho), \frac{1}{2}(\sigma \oplus \sigma)) = D_{\mathcal{F}}(\rho)$, where σ is the optimal free state of ρ. The inequality holds because $\frac{1}{2}(\sigma \oplus \sigma) \in \mathcal{F}$ is a member of the variational class $\mathcal{F}$. Thus, we attribute $D_{\mathcal{F}}^{\text{diff}} < 0$ to failure of the minimisation in finding the global minimum for $D(\frac{1}{2}(\rho \oplus \rho)$ due to the greater number of input probabilities.

B.6.2 Numerical Evidence for Maximal Interaction Distance

Regarding the maximal $D_{\mathcal{F}}$, we use yet again basin-hopping in order to perform the maximisation $\max_\rho D_{\mathcal{F}}(\rho)$, where ρ is diagonal by definition (see 3.3.3) and so the variational parameters of the maximisation are its entanglement energies. For each instance of ρ, we find $D_{\mathcal{F}}$ by the Nelder-Mead method. To take care of local minima, we put the condition that if the cost function is greater than the conjectured value $3-2\sqrt{2}$, then basin-hopping is performed to ensure that it was not a false outcome. Indeed, the maximisation of $D_{\mathcal{F}}$ never manages to exceed $3-2\sqrt{2}$ as shown in Fig.B.1 (Bottom).

B.6.3 Interaction Distance for Random States

It is known that the entanglement spectrum ratio-statistics can characterise the degree of scrambling of information in a state when viewed as the output of a random time-evolution with input a product-state [146]. When the ratio distribution follows what is dictated by a Poisson process then the state is not truly scrambled and the evolution is reversible. On the other hand, if the ratio distribution is of a Wigner-Dyson form, i.e. corresponding either to GOE or GUE depending whether the state is real or complex, then the evolution is characterised irreversible and the the information encoded in the state is scrambled.

The reversibility of a quantum evolution is defined by the runtime complexity of the optimisation whose goal is to completely disentangle an output state with local unitary gates. Polynomial time corresponds to reversible evolutions and exponential to irreversible.

In the following we sample Σ-many entanglement spectra, E_{e}^{σ}, obtained by equi-partitioning random states $|\psi^{\sigma}\rangle$ of L-many 2-level degrees of freedom, where $\sigma = 1, \ldots, \Sigma$. We either generate random states by sampling their amplitudes $\psi_j^{\sigma} \in \mathbb{C}$ from a normal distribution centred at the origin of the complex plane, or we get them as outputs of a random quantum circuit whose input is a random product state. Note that whenever we sample from the normal distribution we mean $N(0,1)$. After sampling, we compute the ratio-statistics $P(r)$ and the interaction distance distribution $P(D_{\mathcal{F}})$. The fitting of the former to Poisson or Wigner-Dyson distributions characterises the scrambling and we find that the latter fits to a log-normal distribution.

B.6.4 Ratio Level Statistics

The ratio-statistics is computed as follows. For each instance of the entanglement spectrum E_{e}^{σ} we sort it in descending order ${E_{\mathrm{e}}}_k{}^{\sigma} \geq {E_{\mathrm{e}}}_{k+1}{}^{\sigma}$, compute its consecutive spacings $s_k^{\sigma} = {E_{\mathrm{e}}}_k{}^{\sigma} - {E_{\mathrm{e}}}_{k+1}{}^{\sigma}$, and then their consecutive ratios, $r_k^{\sigma} = \min(s_k^{\sigma}, s_{k+1}^{\sigma})/\max(s_k^{\sigma}, s_{k+1}^{\sigma})$. After collecting all sets of ratios in $r = \cup_{\sigma} r^{\sigma}$, we can obtain the normalised histogram $P(r)$.

B.6.5 Random Free Entanglement Spectra

Free fermionic $E_{\mathrm{e}}^{\mathrm{f}}$ spectra of the form (3.14) have by definition zero free-fermion interaction distance, $D_{\mathcal{F}}(E_{\mathrm{e}}^{\mathrm{f}}) = 0$. After sampling Σ-many Gaussian spectra E^{f}, we compute the ratio distribution, $P(r)$. A random free entanglement spectrum is generated by picking N single-body entanglement energies from the normal distribution such that $\epsilon_i \leq \epsilon_{i+1},\ i = 1, \ldots, N-1$. After creating the many body entanglement spectrum we can normalise it by shifting all ϵs by $\log \sum_k e^{-E_{ek}^{\mathrm{f}}}$.

As expected, $P(r)$ for free spectra follows the Poisson distribution, $P_{\mathrm{Poisson}}(r) \propto \frac{1}{(1+r)^2}$ as shown in Fig.B.2. We understand these states as the outputs of Gaussian channels with input a random product state. Gaussian channels are of the

form e^{iHt} where H is a quadratic in fermions. Thus populations are not coupled and the correlations remain Gaussian and thus $D_{\mathcal{F}} = 0$.

B.6.6 Random Entanglement Spectra

We now sample random states from the Hilbert space constructed on L-many 2-level degrees of freedom. A random state $|\psi\rangle$ is represented as a $2^L \times 1$ array with elements $\psi_j = \alpha_j e^{i\beta_j \theta}$, $j = 1, 2, \ldots, 2^L$ where α_j are random numbers from the normal distribution $\beta \in [0, 1]$ box-random numbers. The angle $\theta \in \{0, 2\pi\}$ determines whether the amplitudes are real or complex. Then we normalise by dividing the amplitudes by $\sum_j |\psi_j|^2$. To get the entanglement spectrum for an equipartition of $|\psi\rangle$ we use the reshape method. In Fig. B.3 (Left) we then confirm that $P(r)$ fits the Wigner-Dyson distributions, $P_{\text{WD}}^{\text{GOE}}$ or $P_{\text{WD}}^{\text{GUE}}$, for $\psi_j \in \mathbb{R}$ or $\psi_j \in \mathbb{C}$ respectively, as expected. These are given by

$$P_{\text{WD}}(r) \propto \frac{1}{Z} \frac{(r + r^2)^\beta}{(1 + r + r^2)^{1+3\beta/2}}, \tag{B.9}$$

with $Z = \frac{8}{27}$ and $\beta = 1$ for $P_{\text{WD}}^{\text{GOE}}$ and $Z = \frac{4}{81}\frac{\pi}{\sqrt{3}}$ and $\beta = 2$ for $P_{\text{WD}}^{\text{GUE}}$ [146].

Proceeding to compute $D_{\mathcal{F}}$ for the sample, we find that its distribution, $P(D_{\mathcal{F}})$, is fitted well with a log-normal distribution

$$P_{\text{LN}}(r, \mu_{\text{LN}}, \delta_{\text{LN}}) = \frac{1}{r\delta_{\text{LN}}\sqrt{2\pi}} e^{-(\ln r - \mu_{\text{LN}})^2/2\delta_{\text{LN}}^2}, \tag{B.10}$$

as demonstrated in Fig.B.3 (Right). Note the steep tail of the distribution for high values of the interaction distance indicating how rare maximally interacting states are.

B.6.7 Random Quantum Circuits

Another way to sample random states from the Hilbert space of L qubits is from outputs of random circuits C, as illustrated in Fig. B.4. These can be seen as time evolutions with input a random product state of L qubits, $|\psi_0^\sigma\rangle = \otimes_j |q_j\rangle$ with $|q_j\rangle = \cos\frac{\theta_j}{2}|0\rangle + e^{i\phi_j}\sin\frac{\theta_j}{2}|1\rangle$ where $\theta_j \in [0, \pi]$ and $\phi_j \in [0, 2\pi]$ box-random angles on the j-th Bloch sphere.

For a each C_σ, we repeatedly apply a random quantum gates to a randomly chosen qubit or pair of neighbouring qubits. What is important here is that the gate set from which gate g_t is drawn can be non-universal or universal. For the former case, we choose g_t by picking from the set $\{NOT, H, CNOT\}$ uniformly. For the latter case we apply a $U(4)$ Haar-random 2-qubit unitary at each t. A Haar random matrix in $U(N)$ is generated as follows. We create $X = \frac{1}{\sqrt{2}}(A+iB)$ where A, B are $N \times N$ matrices with elements in $\mathrm{N}(0,1)$. Then we perform a QR decomposition of X and get the orthogonal Q and upper-triangular R matrices. Now redefine R so that it is diagonal keeping only the phases of its original diagonal, $R \to \mathrm{diag}(\mathrm{diag}(R)/|\mathrm{diag}(R)|)$, where the division and absolute functions act element-wise. Finally, recompose to obtain Haar random $U = QR$.

The entanglement spectrum $E^\sigma_{e\,t}$ is obtained by equi-partitioning the state at a certain time-step t, and from it we can obtain the entanglement entropy S_t and interaction distance $D_{\mathcal{F}t}^\sigma$. We then sample Σ-many circuits C_σ and compute their averages at each time step, $\langle S_t \rangle$ and $\langle D_{\mathcal{F}t} \rangle$, and find that they saturate at approximately the same time, $t = T$, see Fig. B.5 and Fig. B.6. For each C_σ, at saturation time T we stop the evolution and obtain the mixed output state $|\psi_T^\sigma\rangle$ which is accompanied by its $D_{\mathcal{F}T}^\sigma$. For these states we can compute the distribution $P(D_{\mathcal{F}})$ over the sample of outputs $|\psi_T^\sigma\rangle$ and the ratio-statistics $P(r)$ over the spectra E^σ_{eT}.

If $g_t \in \{NOT, H, CNOT\}$, then $|\psi_T\rangle$ is not scrambled, consistent with $P(r)$ following P_{Poisson}, see Fig. B.5. If $g_t \in U(4)$, then it is scrambled, consistent with $P(r)$ following $P^{\text{GUE}}_{\text{WD}}$, see Fig. B.6. In particular, if we project the amplitudes of the outputs to their real components $\mathrm{Re}(\psi^\sigma_{Tj})$ then $P(r)$ fits to $P^{\text{GOE}}_{\text{WD}}$, shown in Fig. B.6, still capturing the fact that the evolution is chaotic. The $D_{\mathcal{F}}$-statistics again fits a log-normal.

B.6.8 Comments and Open Questions

Free-fermion states have by definition $D_{\mathcal{F}} = 0$, and their Poisson ratio-statistics shows non-scrambling. However, obvserving Poisson r-statistics for generic random states, as observed for outputs of non-chaotic circuits using non-universal gates, still allows for finite $D_{\mathcal{F}}$-values. This is due to the fact that any two-qubit

gate, in our case $CNOT$ as part of the non-universal gate set we used, can be seen as a time evolution with a Hamiltonian containing quartic fermion terms.

In any case, we found that the distribution of interaction distance follows the log-normal distribution, for both scrambled and non-scrambled states. However, we notice that consistently the non-scrambled states (Fig.B.5) have the absolute value of the log-normal fitting parameter $|\mu_{\text{LN}}|$ almost three times that of the one for scrambled states (Figs.B.3 and B.6). However it is a quantitative difference and not a qualitative one. Nevertheless, it seems consistent and robust. For example, when the random state's amplitudes are sampled from a uniform or a power-law distribution these results remain unaltered.

As an open question, we aks how the free states $\sigma \in \mathcal{F}$ are distributed in the space of reduced states $\mathcal{D}(\mathcal{H}_{\text{e}})$. This question is left for future work to explicitly be fleshed out. However we can make some first observations. We know that $\mathcal{D}(\mathcal{H}_{\text{e}})$ can be represented as a sphere of unit radius in in units of the trace distance due to this distance's upper bound. We also found that $\forall\rho$ there exists a σ at most $D_{\mathcal{F}}^{\max}$ far. This means that the illustration in Fig.(3.2) is not accurate. More accurate would be to depict a foam-like distribution of free states around every $\rho \in \mathcal{D}(\mathcal{H}_{\text{e}})$. Finally, we hint towards future work entailing the use of the results obtained for outputs of random circuits to detect the localisation-delocalisation transition. Of relevance is the work of Ref. [147] where the XXZ model is studied. At each time-step of the circuit, we can obtain the distribution $P(D_{\mathcal{F}})$. Since we know that in the infinite time limit it should converge to the Wigner-Dyson distributions we can construct the Kolmogorov distance between them and track its decay in time. In the delocalised phase the decay should be exponential, but a polynomial decay would signal the onset of the many-body localised phase.

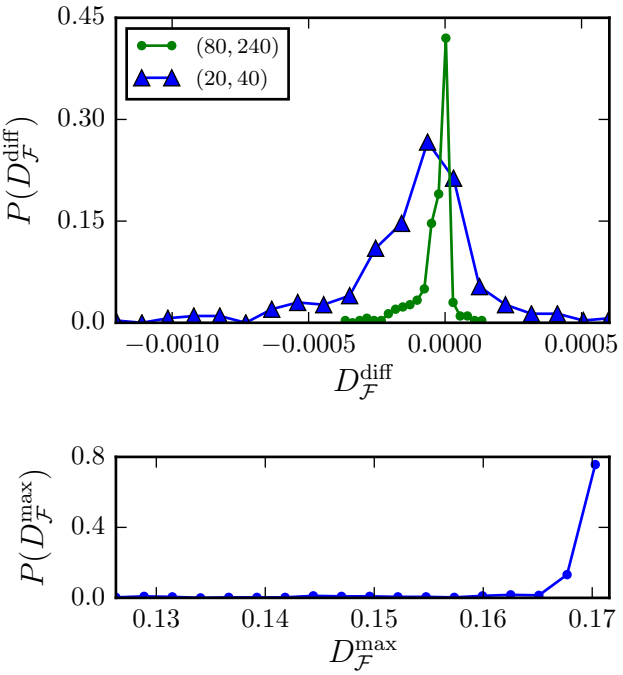

Figure B.1: (Top) Distribution $P(D_{\mathcal{F}}^{\text{diff}})$ of $D_{\mathcal{F}}^{\text{diff}} = D_{\mathcal{F}}(\rho) - D_{\mathcal{F}}(\frac{1}{2}(\rho \oplus \rho))$ for random states ρ and their doubled versions $\frac{1}{2}(\rho \oplus \rho)$. The sample contains 300 instances of ρ. Increasing the number of basins in the minimisations of $D_{\mathcal{F}}(\rho)$ and $D_{\mathcal{F}}(\frac{1}{2}(\rho \oplus \rho))$, indicated as a tuple (Legend), reinforces our conjecture that $D_{\mathcal{F}}^{\text{diff}} = 0$. (Bottom) Distribution of outputs of $\max_\rho D_{\mathcal{F}}(\rho)$ performed 400 times where ρ's rank is randomly selected between 3 and 8. Here, the number of basins in $D_{\mathcal{F}}$'s minimisation is 30. The number of basins for the maximisation is randomly selected from the set $\{5, 15, 50\}$. The maximisation achieves the conjectured upper bound $3 - 2\sqrt{2} \approx 0.1716$ but never exceeds it.

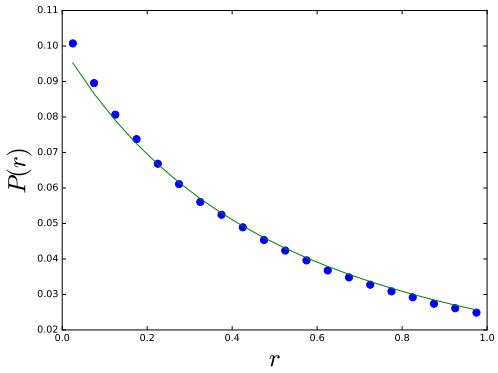

Figure B.2: $P(r)$ for free spectra E_{e}^{f} of $N = 10$ fermions, with energies ϵ sampled from $\text{N}(0, 1)$ for $\Sigma = 10^4$ samples. $P(r)$ fits P_{Poisson} showing that the free states are non-scrambled.

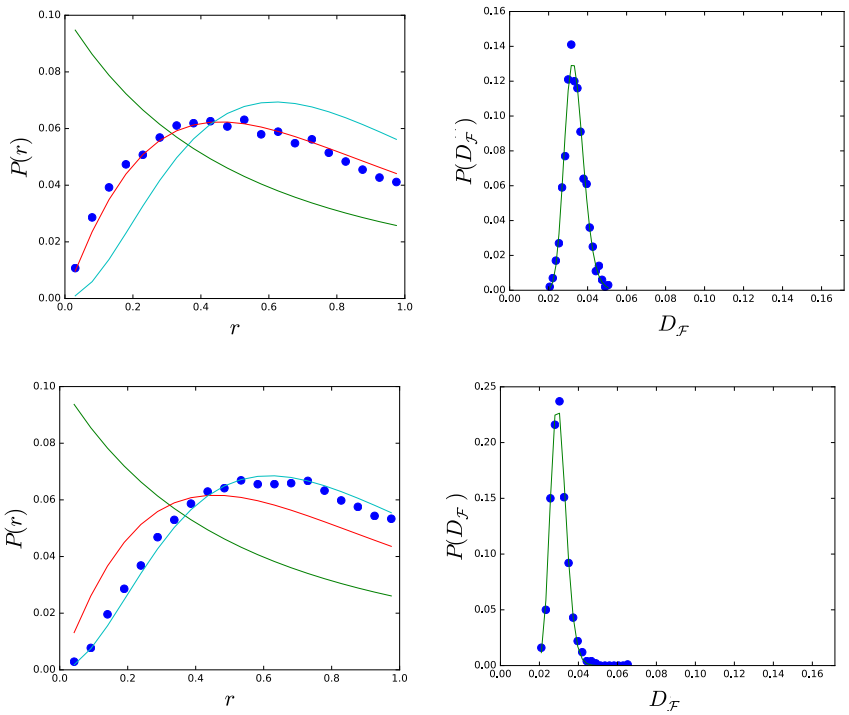

Figure B.3: $P(r)$ and $P(D_{\mathcal{F}})$ for $\Sigma = 10^3$ states of $L = 10$ degrees of freedom. $P(r)$ follows P_{GOE} when $\psi_j \in \mathbb{R}$ (Top) and P_{GUE} when $\psi_j \in \mathbb{C}$ (Bottom). Interaction distance distribution $P(D_{\mathcal{F}})$ is fitted with P_{LN} given by (B.10) with $(\mu_{\text{LN}} = -0.15, \delta_{\text{LN}} = -3.41)$ when $\psi_j \in \mathbb{R}$ (Top) and with $(\mu_{\text{LN}} = 0.13, \delta_{\text{LN}} = -3.52)$ when $\psi_j \in \mathbb{C}$ (Bottom).

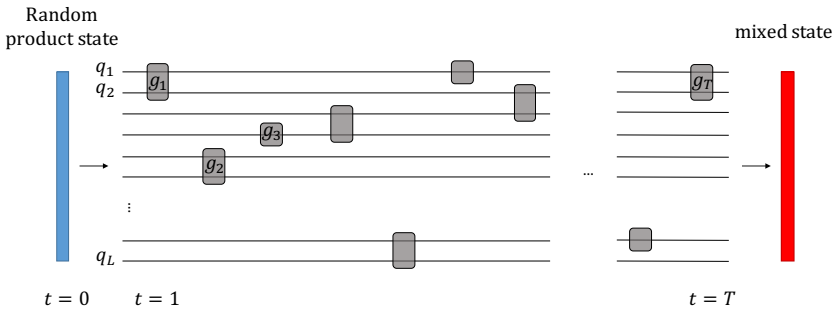

Figure B.4: Example of random circuit C. A random one- or two- qubit gate g_t is applied at a random quibit or neighbouring qubits respectively at every time-step $t = 0, 1, \ldots, T$.

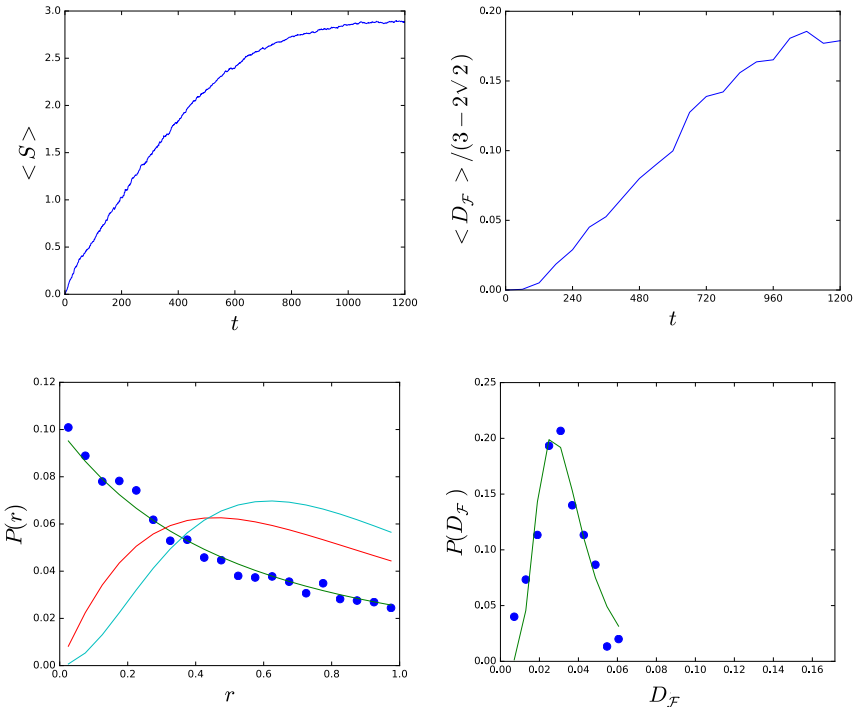

Figure B.5: We realise $\Sigma = 150$ circuits C_σ, with $\sigma = 1, \ldots, \Sigma$, comprising randomly selected non-universal gates $g_t \in \{NOT, CNOT, H\}$, with $t = 1, \ldots, T$ and $T = 1200$ gates. Average entropy $\langle S \rangle$ and interaction distance $\langle D_{\mathcal{F}} \rangle$ saturate at the same time $t \approx 1100$. Ratio distribution $P(r)$ of the outputs $|\psi_T^\sigma\rangle$ follows P_{Poisson}, thus the evolution is reversible. Interaction distance distribution $P(D_{\mathcal{F}})$ follows P_{LN} with $\mu_{\text{LN}} = 0.42$ and $\delta_{\text{LN}} = -3.44$.

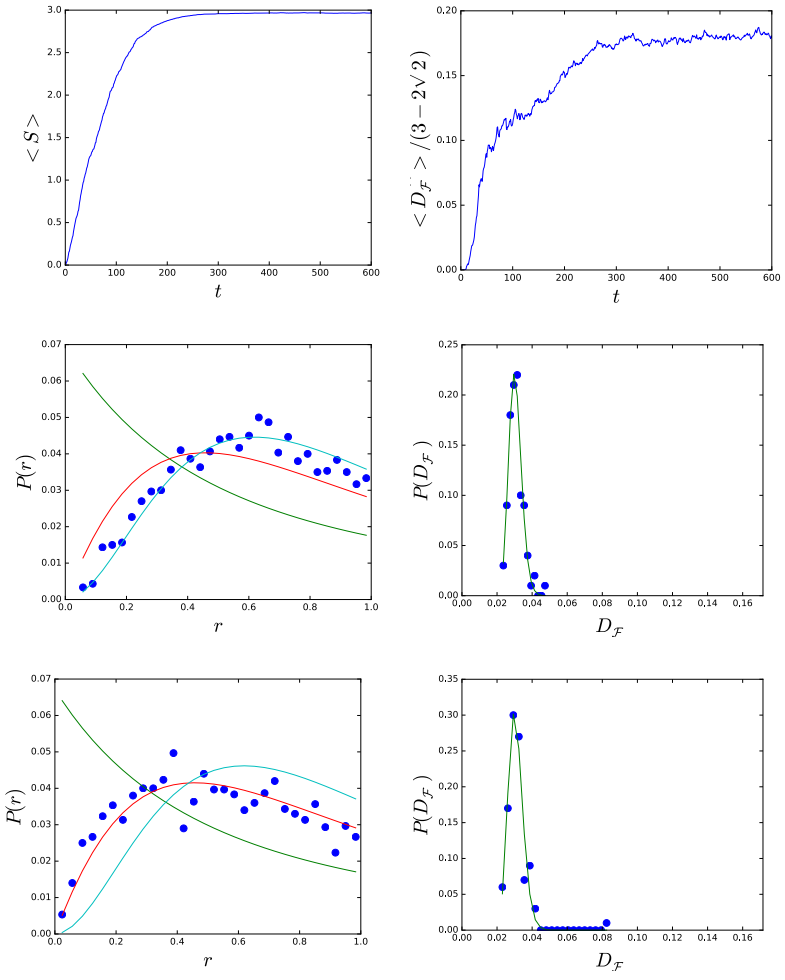

Figure B.6: We realise $\Sigma = 100$ circuits C_σ, with $\sigma = 1, \ldots, \Sigma$, consisting of Haar-random two-qubit unitary gates $g_t \in U(4)$, $t = 1, \ldots, T$ and $T = 600$. Average entropy $\langle S \rangle$ and interaction distance $\langle D_{\mathcal{F}} \rangle$ saturate at the same time $t \approx 300$. Ratio distribution $P(r)$ of the outputs $|\psi_T^\sigma\rangle$ follows $P_{\text{WD}}^{\text{GUE}}$, thus the evolution is chaotic. Interaction distance distribution $P(D_{\mathcal{F}})$ follows P_{LN} with $\mu_{\text{LN}} = -0.12$ and $\delta_{\text{LN}} = -3.50$. If the amplitudes of the output state are projected to their real part $\text{Re}(\psi_{j_T}^\sigma)$, then $P(r)$ follows $P_{\text{WD}}^{\text{GOE}}$ and the chaotic evolution is still apparent. Also $P(D_{\mathcal{F}})$ again follows P_{LN} now with $\mu_{\text{LN}} = 0.14$ and $\delta_{\text{LN}} = -3.44$.

Appendix C

Kitaev Model

C.1 Band Structure

Here we present the momentum kernels of the no- and full-vortex sectors, obtained by a Fourier both along $\mathbf{v}_x$ and $\mathbf{v}_y$ to get the corresponding momenta q, p.

For the no-vortex sector we have

$$h(q,p) = \frac{i}{2}\begin{bmatrix} K(e^{i(q-p)} + e^{ip} + e - iq) & J(e^{-ip} + e^{-iq}) + 1 \\ 0 & K * (e^{i(p-q)} + e^{-ip} + e^{iq}) \end{bmatrix} + \text{h.c.}. \quad \text{(C.1)}$$

In the full-vortex sector we have unit-cells containing two z-links along the x direction and so the Bravais vector that enumerates them is $2\mathbf{v}_x$ and thus

$$\begin{aligned} h(q,p) &= \text{diag}\,(-K\sin p,\ K\sin p,\ K\sin p,\ -K\sin p) \\ &+\Big(\tfrac{i}{2}\begin{bmatrix} 0 & (1+Je^{-ip}) & K(e^{-ip}+e^{-iq}+e^{i(p-q)}-1) & Je^{-iq} \\ 0 & 0 & -J & K(e^{i(p-q)}-e^{-iq}+e^{-ip}+1) \\ 0 & 0 & 0 & 1-Je^{-ip} \\ 0 & 0 & 0 & 0 \end{bmatrix} \\ &+\text{h.c.}\Big). \end{aligned} \quad \text{(C.2)}$$

Their spectra for $J = 1$ and $K = 0.1$ are shown in Fig. C.1.

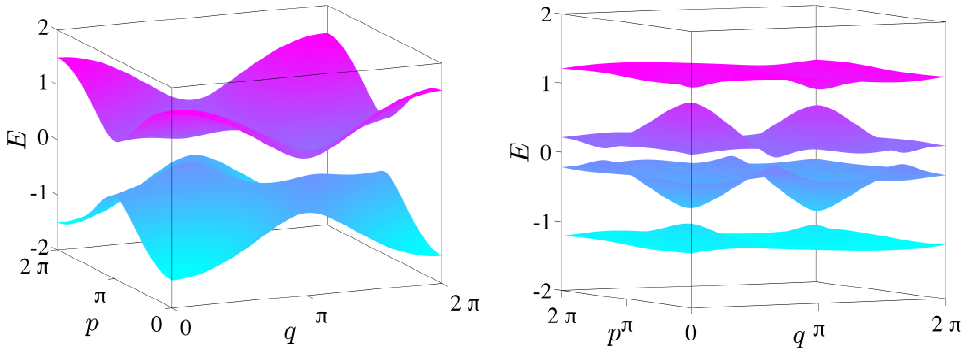

Figure C.1: Spectra of no-vortex and full-vortex momentum-kernels.

C.2 Analytic Forms of the Energy Gaps

The eigenvalues for the above kernels $h(q,p)$ can be found analytically and the energy gap $G(p)$ for each p chain can be found from them as the difference of the two eigenvalues closest to zero and then minimizing over the q-momentum. In the vortex-free sector we have

$$\begin{aligned} G(p) &= \min_q \sqrt{|f(q,p)|^2 + g(q,p)^2}, \\ f(p,q) &= 2i(1 + \frac{1}{2}e^{iq} + \frac{1}{2}e^{ip}), \\ g(p,q) &= 4K(\sin p - \sin q + \sin(q-p)), \end{aligned} \tag{C.3}$$

where $q \in [0, 2\pi]$. For $K = 0$, in the full-vortex sector the gap is given by

$$\begin{aligned} G(p) &= \min_q 2\sqrt{1 + 2J^2 - J\sqrt{2g(q,p)}}, \\ g(p,q) &= 2 + \cos 2p - \cos 2q + J^2(1 + \cos 2(p-q)), \end{aligned} \tag{C.4}$$

and for $K > 0$ its form is unpleasantly complicated.

C.3 $J - \theta$ Phase Diagram

Here we compute the Chern number (Eq. (2.10)) of Kitaev's honeycomb as a function of the microscopic parameters J and θ for a finite $K > 0$. In Fig. C.2 we plot the energy gap (Left) and the Chern number (Right). We observe a

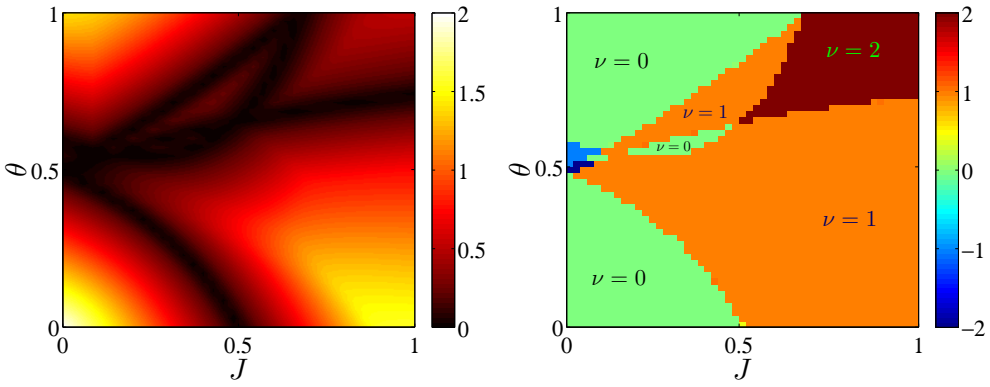

Figure C.2: Kitaev model's phase diagram showing the energy gap G (Left) and the corresponding Chern number ν, for $K > 0$.

$\nu = 1$ phase between the $\nu = 0$ and $\nu = 2$ phases for $\theta > 1/2$. We conjecture that effectively there we have a Hofstadter model with staggered strips, and leave this exploreation for future work. The apparent non-trivial phases phase between the no-vortex and full-vortex trivial phases for $J \approx 0$ are attributed to the unreliability of the method used to compute the Chern number since that regions seems gapless. The trivial phases, the gapped topological phases for $K > 0$, and the phase boundaries between them that are studied in Chapter 4 are located at the boundary of the phase diagram of Fig. C.2.

C.4 Winding Numbers of No-vortex p-chains

In this section we investigate the relation between the the $|\nu| = 1$ Chern number of the no-vortex sector with the winding number of its p-chains (Eq. (4.7)) to which it decomposes after a Fourier transformation. We Fourier transform along the p-chains whose momentum we call q and obtain Hamiltonian kernel $h(q, p)$ for each p-chain. In the Fig. C.3 we show the q-paths traced by the pauli vector $\Sigma_p(q)$ of the kernel for each p-chain. We see that only the p-chains with p between the Fermi points, where edge states exist, give paths that when projected to the $x - y$ plane enclose the origin. Increasing the system size, or equivalently the momentum density we recover the picture consistent with chern number $|\nu| = 1$.

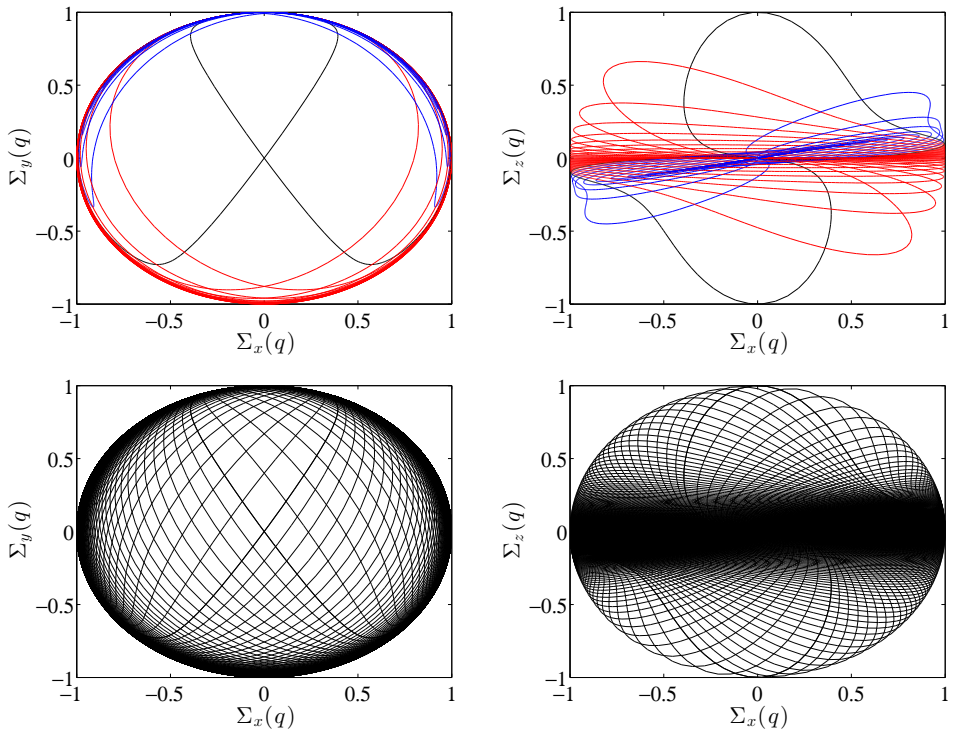

Figure C.3: Paths traced by pauli vectors $\Sigma_p(q)$ for each p-chain on the surface of the unit sphere. (Top) Those corresponding to $\frac{2\pi}{3} < p < \frac{4\pi}{3}$ (red) enclose the origin when projected to the $x-y$ plane to which we assign $w = 1$(Left). Chains at p outside those Fermi points (blue) do not enclose the origin, and for $p = \pm\frac{2\pi}{3}$ (black) the path intersects the origin. We also show the projection to the $x-z$ plane (Right). (Bottom) By increasing momentum density the paths densely cover the sphere once, giving rise to Chern number $|\nu| = 1$.

C.5 Edge Velocity and Entropy for No-vortex: Generating Function Method

We present here the details of the calculation by Cirio based on Refs [104, 105], mainly following the calculation in the Appendix of Ref [103], and presented in even more detail in the Appendix of Ref [106].

In the no-vortex sector, the p-chains in (4.7) look like

$$H(p) = \sum_j \chi_j^\dagger \mathcal{G}_1 \chi_j + \chi_j^\dagger \mathcal{G}_2 \chi_{j-1} + \chi_j^\dagger \mathcal{G}_2^\dagger \chi_{j+1}, \tag{C.5}$$

where $\chi_j^\dagger = \left[\gamma_j^{\mathrm{b}\dagger}\ \gamma_j^{\mathrm{w}\dagger}\right]$, $\mathcal{G}_1 = \begin{bmatrix} g_1 & g_2 \\ {g_2}^* & -g_1 \end{bmatrix}$, and $\mathcal{G}_2 = \begin{bmatrix} g_3 & g_4 \\ 0 & -g_3 \end{bmatrix}$, with $g_1 = -K\sin p$, $g_2 = \frac{i}{2}(Je^{-ip}+1)$, $g_3 = \frac{i}{2}K(1-e^{ip})$, and $g_4 = \frac{i}{2}J$. We express the edge state as $\Psi = \sum_{j=1}^{\infty}\chi_j^\dagger\Psi_j\left|0\right\rangle$ with $\Psi_j = \left[\Psi_j^1\ \Psi_j^2\right]^T$.

Placing the system on a semi-infinite cylinder with circumference along $\mathbf{v}_y$, the Schrödinger equation $H(p)\Psi = E\Psi$ leads to the following recursive equation

$$\mathcal{G}_2\Psi_{j-1} + (\mathcal{G}_1 - E)\Psi_j + \mathcal{G}_2^\dagger\Psi_{j+1} = 0, \tag{C.6}$$

and imposing semi-infinite boundary conditions such that the cylinder is open at $j = 1$ and extends to $j \to +\infty$ we have

$$(\mathcal{G}_1 - E)\Psi_1 + \mathcal{G}_2^\dagger\Psi_2 = 0. \tag{C.7}$$

We then multiply (C.6) by $z^j \in \mathbb{C}$ and sum over j. The generating function is defined as $G(z) = \sum_{j=1}^{\infty} z^{j-1}\Psi_j$. Gathering the terms proportional to $G(z)$ and imposing the boundary condition (C.7) we obtain

$$\left(z^2\mathcal{G}_2 + z(\mathcal{G}_1 - E) + \mathcal{G}_2^\dagger\right)G(z) = \mathcal{G}_2^\dagger\Psi_1, \tag{C.8}$$

and thus the generating function is given by

$$G(z) = \left(z^2\mathcal{G}_2 + z(\mathcal{G}_1 - E) + \mathcal{G}_2^\dagger\right)^{-1}\mathcal{G}_2^\dagger\Psi_1. \tag{C.9}$$

More explicitly we write

$$G(z) = \frac{1}{\det\Delta}\begin{bmatrix}\tilde{\phi}_1 \\ \tilde{\phi}_2\end{bmatrix},\ \text{with}\ \begin{bmatrix}\tilde{\phi}_1 \\ \tilde{\phi}_2\end{bmatrix} = \begin{bmatrix}\tilde{g}_1 & \tilde{g}_2 \\ \tilde{g}_3 & \tilde{g}_4\end{bmatrix}\begin{bmatrix}\phi_1 \\ \phi_2\end{bmatrix},\ \begin{bmatrix}\phi_1 \\ \phi_2\end{bmatrix} = \mathcal{G}_2^\dagger\Psi_1, \tag{C.10}$$

where $\Delta = z^2\mathcal{G}_2 + z(\mathcal{G}_1 - E) + \mathcal{G}_2^\dagger$, $\tilde{g}_1 = -g_3z^2 + (-g_1 - E)z - g_3^*$, $\tilde{g}_2 = -g_4z^2 - g_2z$, $\tilde{g}_3 = -g_2^*z - g_4^*$, $\tilde{g}_4 = g_3z^2 + (g_1 - E)z + g_3^*$, and $\tilde{\phi}_{1,2}$ are quadratic in z.

The energy dispersion $E(p)$ can be obtained from an analysis of the poles of $G(z)$. Since $\det\Delta$ is quartic in z, it has four roots. However, note that for a root $z_0 \neq 0$ we have that $\Delta(\frac{1}{z_0^*}) = \frac{1}{z^{*2}}\Delta^*(z_0) = 0$, and so the poles of $G(z)$ come in pairs, $(z_{1,2}, \frac{1}{z_{1,2}})$. In general an edge mode exists at the ends of a p-chain if the all the poles lie outside of the unit circle [103]. Since the poles of the generating function come in inverse pairs, at least two of them are inside the unit

circle in any case. Therefore, for an edge mode to exists, the poles $z_{1,2}$ of $G(z)$ must cancel with the roots of both $\tilde{\phi}_1$ and $\tilde{\phi}_2$. Imposing that these binomials are proportional to $(z-z_1)(z-z_2)$ leads to to the requirement that the prefactors of their corresponding powers of z must be proportional to each other with the same proportionality constant, t, leaving us with three equations with which to work. From the z^2- and z^0-equations we get $\phi_1 = \xi_\pm \phi_2$, with $\xi_\pm = \frac{-|g_4|^2 \pm \sqrt{|g_4|^4+4|g_3|^2|g_4|^2}}{-2g_3 g_4^*}$, which by substitution back to either of them determines the proportionality constant $t_\pm = \frac{-g_3\xi_\pm - g_4}{g_3}$. Finally, from the z-equation we solve for the energy

$$E_\pm = \frac{t_\pm\,(g_1 - g_2^*\xi_\pm) + g_1\xi_\pm + g_2}{t_\pm - \xi_\pm}, \tag{C.11}$$

with the subscript indicating the right- and left-moving edge mode that can be localised on that edge.

The process can be repeated for semi-infinite boundary conditions with the p-chains extending to $j \to -\infty$ resulting in the reversal of the chirality of the edge modes, $E_\mp$. Furthermore, the magnitude of the poles of $G(z)$ between the two choices of boundary conditions are inversely related. This means that if the system is placed on a finite cylinder, one boundary hosts an edge mode with E_+ and the other with E_-. Linearising its expression around the momentum where the zero energy occurs, $p^\star = \pi$ as shown in Fig. 4.3, we get

$$E_\pm = \pm v_E(p-\pi) + \dots \quad , \qquad v_E = (2J+1)\cos\arctan\left(\frac{J}{4K}\right) \tag{C.12}$$

This analytic expression for the velocity is valid in the momentum range Δp where the pole conditions for the edge states' existence are satisfied (see App and App of Ref. [106]). To find Δp we need to study numerically the behaviour of the roots of $\tilde{\phi}_1$, or equivalently $\frac{\tilde{\phi}_1}{\phi_2}$ and Δ. For a choice of J, K, we denote $N_\pm(p)$ the set of roots of the former and $D(p)$ of the latter, and we collect the poles of $G(z)$ in the set $Z_\pm = \{z | z \in D(p) \wedge z \notin N_\pm(p)\}$ containing all the roots of Δ not cancelled by the numerator $\tilde{\phi}_1$. Then Δp is the momentum range for which poles of $G(z)$ are all either inside or outside of the unit circle, that is $p \in \Delta p \Leftrightarrow |z_0| > 1 \vee |z_0| < 1, \forall z_0 \in Z_\pm\}$. Numerically, one finds that Δp coincides accurately with the distance between the Fermi momenta, between which the edge states exist as shown in the Appendix of Ref [106].

Fog $E_\pm = 0$, the determinant, Δ, of the generating function $G(z)$ given by (C.9) has two roots ($z_1 \to 0, \frac{1}{z_1} \to \infty$) and two roots ($z_2 = \frac{1+Je^{ip}}{J}, \frac{1}{z_2}$). The condition for existence of edge states then is $\{p : |z_2| < 1\}$ which implies $|Je^{ip} + 1| \leq J$ which is satisfied in the momentum interval $\Delta p = 2 \arccos \frac{1}{2J}$.

C.6 Entropy from Edge Toy Model

The four-Majorana Hamiltonian of the toy model is

$$H = i(a_L b_L - a_R b_R) + i w_p (a_L a_R + b_L b_R). \tag{C.13}$$

The von Neumann entropy of the ground state can be computed analytically by combining the Majoranas $a_{\mathrm{L,R}}$ and $b_{\mathrm{L,R}}$ pairwise into into complex fermions f_a and f_b. We then perform a Jordan-Wigner transformation to obtain the 2-spin Hamiltonian

$$H = \begin{bmatrix} \frac{w}{2} & 0 & 0 & -1 \\ 0 & 0 & 0 & 0 \\ 0 & 0 & 0 & 0 \\ -1 & 0 & 0 & -\frac{w}{2} \end{bmatrix}, \quad \text{in the basis} \{|\uparrow\uparrow\rangle, |\uparrow\downarrow\rangle, |\downarrow\uparrow\rangle, |\uparrow\uparrow\rangle\}. \tag{C.14}$$

The ground state is $|\Psi\rangle = \frac{1}{s^2+1}(s|\uparrow\uparrow\rangle + |\downarrow\downarrow\rangle)$ with $s = -\frac{w_p - \sqrt{w_p^2+4}}{2}$ and the reduced density matrix after tracing out one of the spins is $\rho_r = \frac{1}{s^2+1}\mathrm{diag}\,(s^2, 1)$. Its Neumann entropy can be readily calculated.

C.7 Comments on Finite-Size Effects in Kitaev's Honeycomb

In the ideal case of maximal entangled virtual edge modes q can in principle be infinite. This is not always the case for finite-size systems or with the introduction of disorder, as shown Fig. 4.7 (Right). In finite-size systems the edge states can hybridise leading to smaller entanglement between them, and hence a smaller lower bound. Moreover, the entanglement spectrum can exhibit even-odd effects in $|\partial A|$ that can wash out lower bound completely [123]. Nevertheless, due to

the exponential localisation of the edge states, the lower bound can still be recovered in all cases by increasing the system size sufficiently and tuning q to an appropriately large but finite value. Even-odd effects should vanish polynomially in $|\partial A|$, while decoupling of edge states occurs exponentially in the distance between boundary components.

C.8 Monogamy and Temperature

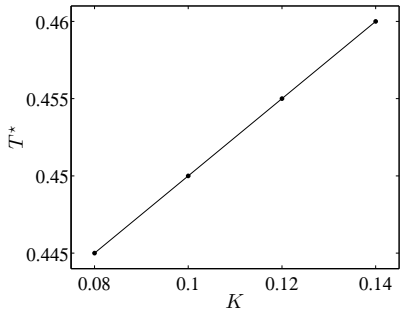

Figure C.4: Critical temperature $T^\star$ for which the maximal entanglement condition $\max \xi^{AB} > 0.98$ is violated for arbitrary cutoff at 0.98, as a function of K.

The $T > 0$ case is studied in Ref [109] where the energy current I appearing at open boundaries in the no-vortex sector is numerically demonstrated to scale as $I \propto cT^2$, confirming Kitaev's prediction (see Appendix of Ref [13]), with $c = \frac{1}{2}$ being the central charge of the CFT describing the chiral Majorana edge. For $J = 1$ and fixed K it is shown that there exists a critical temperature $T^\star$ at which I deviates from the conformal field theory prediction to an arbitrarily chosen degree. Then it is found that $T^\star \propto K$, and as a consequence proportional to the energy gap since $G \propto K$.

Here we want extract the signature of this phenomenon via the singular values ξ^{AB}. First of all we describe how temperature is introduced to Γ. As we saw in section 2.2.2 for $T = 0$ one needs to replace $\pm\varepsilon_i \to 0, 1$ in the diagonal of D. Finite temperature is captured by introducing Botlzmann weights instead of definite occupations as $\pm\varepsilon_i \to \frac{e^{\mp\varepsilon_i/T}}{Z_i}$, where $Z_i = e^{-\varepsilon_i/T} + e^{+\varepsilon_i/T}$.

For each instance of K, we obtain the highest singular values $\max \xi^{AB}(T)$. As the critical amount of deviation from the $I \propto cT^2$ scaling was arbitrary, we also set an arbitrary critical $\xi^{AB\star} < 1$ and $T^\star$ is identified as the temperature at which $\max \xi^{AB}$ drops below $\xi^{AB\star}$.

Appendix D

Related Free Models

D.1 Disorder on Haldane

We add disorder to the Haldane model and examine the resilience of the edge states with the monogamy qualifier $\mathcal{S}_q$. Disorder of amplitude Δ is added to the hoppings as in is done for the Kiteav honeycomb's Js and Ks plus local disorder in the form of random on-site energies implemented by adding $\sum_j w_j f_j^\dagger f_j$ to the Hamiltonian, with $0 < w_j < \Delta$. The stability of such Chern insulating phases is studied in Refs. [16, 15] and we conclude here that as long as the disorder amplitude is smaller compared to the energy gap, $\Delta \ll G$, then the monogamy signature is reliable. In Fig. D.1 the monogamy signature is captured by $\mathcal{S}_q$ given by (3.12) for an appropriately large q. Deep in the topological phase, $\phi \approx \frac{\pi}{2}, \frac{3\pi}{2}$, the edge entanglement persists for higher disorder amplitudes Δ.

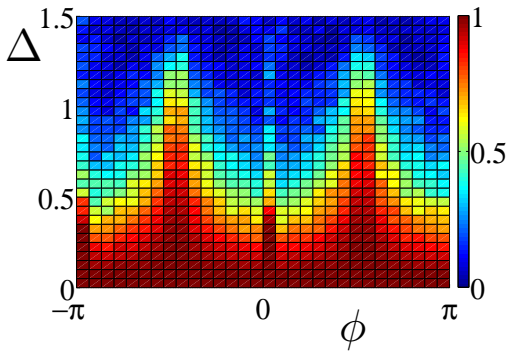

Figure D.1: Haldane's phase diagram showing the resilience of the topological Haldane phase, measured by $\frac{1}{4}\mathcal{S}_q$ for finite $q \gg 1$, against disorder amplitude Δ. The monogamy signature is most robust deep in the topological phase. Here $L_x = L_y = 30$ unit-cells and the data is averaged over 30 disorder realisations.

D.2 From Haldane to SSH

As mentioned in 5.2.2, we label the lattice as shown in Fig. 4.1 and perform a Fourier transformation along $\mathbf{v}_y$ for the Haldane model. Focusing at the $p^\star$-chain, we can obtain its momentum kernel by performing a Fourier transformation along this chain to obtain

$$h_{\text{Hal}}(q) = (t_1 \cos q)X + (t_1 \sin q)Y + 2t_2 \left(-\cos(\phi + q) - \cos\phi + \cos(\phi - q)\right) Z. \tag{D.1}$$

Now, performing a Fourier along the SSH chain written in (5.2) we find its momentum kernel to be

$$h_{\text{SSH}}(q) = \left(-(t - \delta t) - (t + \delta t)\cos q\right) X + \left((t + \delta t)\sin q\right) Y. \tag{D.2}$$

The winding number of h_{SSH} is $w = 1$ as long as $|\delta t| < t$ and a quantum phase transition to the trivial phase with $w = 0$ occurs when $\delta t = 0$, i.e. when the hoppings are uniform. On the other hand, the winding number of h_{Hal}, under the physically reasonable assumption that $|t_2| < |t_1|$, is $w = 1$, $\forall \phi \neq \kappa\pi$, $\kappa \in \mathbb{Z}$. These statements are extremely simple to confirm numerically by plotting the $\Sigma(q)$ vector of both kernels and tracking its winding on the unit sphere. Specifically, we can choose $t_1 = -(t + \delta t)$. Then we can set the SSH model to be at its topological fixed point with $t = \delta t$. Finally, to make the two kernels equal we impose $\left(-\cos(\phi + q) - \cos\phi + \cos(\phi - q)\right) = 0$ which results in the solution $\phi = -2\arctan\left(2\sin q - \sqrt{4\sin^2 q + 1}\right)$.

D.3 Disorder on SSH

Here we examine the effect that disorder has on the correlations of the SSH model 5.2 at half-filling. This we measure by the skewness, α_3 given by (2.15), of the single-body entanglement spectrum, i.e. the eigenvalues of the restricted to a segment of the chain. Disorder of amplitude Δ is added to the hoppings $t \pm \delta t$ as symmetric and uniform randomness. A local random chemical potential, $\sum_j 2(\Delta_j - \frac{1}{2}) f_j^\dagger f_j$, where $|\Delta_j| < \Delta$ a uniform random number, is also added to the Hamiltonian.

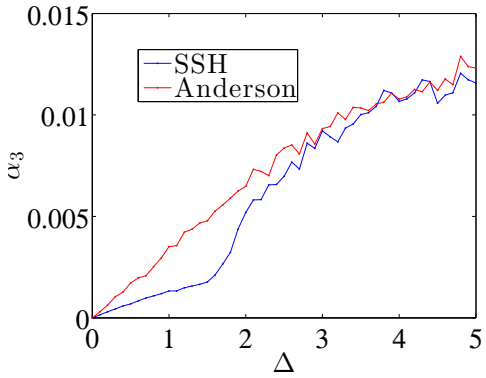

Figure D.2: Skewness α_3 increasing with disorder amplitude Δ for a uniform-hoppings chain at half filling $F = L = 100$ for Anderson (red) and SSH (blue). For each Δ-value we averaged 100 disorder realisations. SSH is protected by the gap and for large Δ behaves as Anderson.

For every value of w we obtain α_3 for 300 disorder realisations and average over them. In Fig. D.2 we show α_3 as a function of disorder amplitude Δ. Setting uniform hoppings we have the Anderson model [148], $\delta t = 0$, and α_3 increases with Δ. We then set alternating hoppings $\delta t = \frac{1}{2}$ and see that the effect disorder has on the SSH model is suppressed by the gap for small w and then it behaves like the Anderson model for large Δ.

D.4 Analytic Form of Toy Model's Entropy for Haldane's Honeycomb

The Haldane model hosts Dirac edge states. Thus the analogue of the toy model constructed for the no-vortex sector of Kitaev's Honeycomb in this case is a four-site complex-fermion hopping model,

$$H = (d_4^\dagger d_1 + d_2^\dagger d_3) + iw(d_1^\dagger d_2 + d_3^\dagger d_4) + \text{h.c.} \tag{D.3}$$

where w represents a weak tunneling amplitude through the bulk. Higher hybridisation w represents moving away from the ideally decoupled end state case, or equivalently moving away from the $p^\star$-momentum which contributes maximal entropy.

Performing a Jordan-Wigner transformation we get a 4-spin Hamiltonian of size 16×16 in the 4-spin basis $\{|s_0 s_1 s_2 s_3\rangle \, | s_i = \uparrow, \downarrow\}$. The reduced density matrix of the ground state, $|gs\rangle$ with energy $E_{gs} = -\sqrt{2 - 5w^2 + 2|1 + 2w^2|}$, is obtained

by tracing out two of the spins in $\rho = |gs\rangle \langle gs|$ and its von Neumann Entropy is

$$S_{2\text{spin}} = -\frac{1}{8N}(16 \log \frac{1}{N} + (F - GR) \log \frac{(F - GR)}{8N} \tag{D.4}$$

$$+(F + GR) \log \frac{(F + GR)}{8N}), \tag{D.5}$$

where

$$N = 2 - \left(\frac{w}{2}\right)^2 + 2s_1^2 + s_2^2 \quad , \quad F = -w^2 + 8s_1^2 + 4s_2^2,$$
$$G = iw + 2s_2 \quad , \quad R = \left(-w^2 - 4iws_2 + 4\left(4s_1^2 + s_2^2\right)\right)^{frac12},$$
$$s_1 = \frac{4 - w^2}{2|E_{gs}|} \quad , \quad s_2 = \frac{iw(4 - w^2)}{2E_{gs}^2}.$$

D.5 Chern Semi-metal Phase Transition

Here we present details regarding the phase transitions of the Chern Semi-metal. For simplicity, we fix $K = -J = 1$ and $\theta = \frac{\pi}{2}$ the kernel of the Hamiltonian in momentum space is

$$h = \begin{bmatrix} 0 & e^{-ip_x} - 1 & -im \\ e^{ip_x} - 1 & 0 & e^{-ip_y} - 1 \\ im & e^{ip_y} - 1 & 0 \end{bmatrix}, \tag{D.6}$$

Because the kernel is traceless, only two of its eigenvalues, $E_i(p_x, p_y, m)$ with $i = 1, 2, 3$, are independent. Therefore we find the parameter values for which the higher band E_1 touches the middle band E_2 in order to identify the phase transitions. Furthermore, we notice that the extrema of these bands occur on the diagonal of the Brillouin zone. and so we set $p_x = p_y$. In particular, the minimum of the higher band, $E_1^{\min}$ is unique and located at $p_x = 0$ for any value of $m < m_c$. At the same time, the maximum of middle band $E_2^{\max}$ is located at $p_x \approx 1.583$ for any value of $m \leq m_c$, see Fig.(D.3) (Left). We determine the value of m_c numerically to be $m_c \approx 1.4$ as shown in Fig.(D.3) (Right).

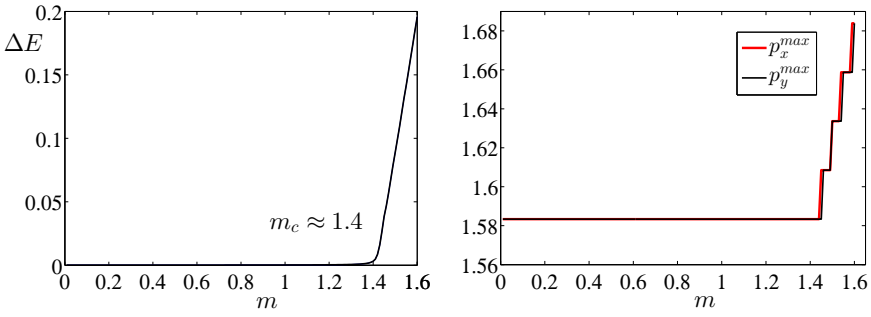

Figure D.3: (Left) Opening of the indirect gap $\Delta E = E_1 - E_2$ of the model when m_c is reached. (Right) The momenta $p_x^{\max}, p_y^{\max}$ where the maximum of the middle band occurs. As the parameter m is varied and as long as $m \leq m_c$, the position of the maximum does not move. The lines are degenerate because the extrema of the bands occur on the diagonal of the Brillouin Zone.

When a phase transition occurs for $m = m_c$, the bands touch each other. In this critical case, E_1^{min} becomes doubly degenerate, i.e. at another momentum $p_x \approx 1.583$ the higher band comes down to the same value as the value it has for $p_x = 0$. The value of the minimum of the higher band which coincides with the maximum of the middle band is a function of m for $m \leq m_c$, given by

$$E_1^{\min} = E_2^{\max} = \sqrt{\frac{3}{2}}\, m. \tag{D.7}$$

Appendix E

Related Interacting Models

E.1 Covariance Matrix for the SSHH Model

The Fock basis is $\left|b_1^{\uparrow},\ldots,b_L^{\uparrow},b_1^{\downarrow},\ldots,b_L^{\downarrow}\right\rangle$ where $b_i^s \in \{0,1\}$, or fermionic occupations on each site, for spin $s =\uparrow,\downarrow$. The constraint for half filling and $S_z = 0$ demands $\sum_{i,s} b_i^s = L$ and $\sum_i b_i^{\uparrow} = \sum_i b_i^{\downarrow}$. The dimension of the Fock space is the number of the binary words that satisfy these two conditions.

After exact diagonalisation for periodic boundary conditions, we find the unique ground state vector to be a superposition on this basis

$$|gs_{PBC}\rangle = \sum_{b^{\uparrow},b^{\downarrow}} A_{b^{\uparrow},\mathbf{b}^{\downarrow}} \left|b^{\uparrow},b^{\downarrow}\right\rangle . \tag{E.1}$$

From the correlation matrices $C_{i,j}^{s,s'} = \langle f_i^{s\dagger} f_j^{s'}\rangle$ and $\tilde{C}_{i,j}^{s,s'} = \langle f_i^{s} f_j^{s'}\rangle$, which are expressed in terms of the amplitudes $A_{\mathbf{b}^{\uparrow},\mathbf{b}^{\downarrow}}$ we get $\langle\gamma_k\gamma_l\rangle$ and so we compute Γ as follows. We begin by decomposing f_j in terms of Majorana fermions $\gamma_{2j-1} = \frac{1}{\sqrt{2}}(f_j + f_j^{\dagger})$ and $\gamma_{2j} = \frac{-i}{\sqrt{2}}(f_j - f_j^{\dagger})$. From the correlation matrices $\langle f_i^{\dagger} f_j\rangle$ and $\langle f_i f_j^{\dagger}\rangle$ we get the correlations of Majoranas in the matrix $P_{kl} = \langle\gamma_k\gamma_l\rangle$ whose dimension

is double that of the correlation matrices' and whose elements are

$$\begin{aligned} P_{2i-1\ 2j-1} =& \frac{1}{2}\langle f_i f_j + f_i f_j^\dagger + f_i^\dagger f_j + f_i^\dagger f_j^\dagger \rangle \\ P_{2i-1\ 2j} =& \frac{-i}{2}\langle f_i f_j - f_i f_j^\dagger + f_i^\dagger f_j - f_i^\dagger f_j^\dagger \rangle \\ P_{2i\ 2j-1} =& \frac{-i}{2}\langle f_i f_j + f_i f_j^\dagger - f_i^\dagger f_j - f_i^\dagger f_j^\dagger \rangle \\ P_{2i\ 2j} =& \frac{-1}{2}\langle f_i f_j - f_i f_j^\dagger - f_i^\dagger f_j + f_i^\dagger f_j^\dagger \rangle. \end{aligned}$$

If there are no pairing terms in the Hamiltonian, then the terms $\langle f_i f_j \rangle = 0.\ \forall i, j$. From P we can now build the Covariance matrix $\Gamma = i\left(P - P^T\right)$.

E.1.1 Winding Number for the SSHH Model

The SSHH model supports a non-trivial winding number $|w| = 1$ for $\delta t > 0$. We want the winding number as the winding of a unit vector $\langle \Sigma^s(p) \rangle$ on the surface of the sphere, where $p \in [0, 2\pi)$ is the momentum in the Brilluin zone. We rename the fermionic operators that act on either site in the unit cell as $f^s_{2x-1} \to a^s_x, f^s_{2x} \to b^s_x$ and define the observables that will give us a winding number for each spin component as $\Sigma^s_x = a^{s\dagger}{}_p b^s{}_p + b^{s\dagger}{}_p a^s{}_p$, $\Sigma^s_y = -ia^{s\dagger}{}_p b^s{}_p + ib^{s\dagger}{}_p a^s{}_p$, $\Sigma^s_z = a^{s\dagger}{}_p b^s{}_p - b^{s\dagger}{}_p a^s{}_p$, where $s = \uparrow, \downarrow$, as is done in Refs [125, 126]. In order to calculate its expectation value with the ground state for periodic boundaries, $\langle gs_{PBC}| \Sigma^s(p) |gs_{PBC}\rangle$, we Fourier transform the fermionic operators $a^s{}_p, b^s{}_p$ back to real space to obtain

$$\Sigma^s_x = \sum_{x',x=1}^{L/2} C^{s,s}_{2x'-1,2x} e^{ip(x-x')} + C^{s,s}_{2x,2x'-1} e^{-ip(x-x')}, \tag{E.2}$$

$$\Sigma^s_y = \sum_{x',x=1}^{L/2} -iC^{s,s}_{2x'-1,2x} e^{ip(x-x')} + iC^{s,s}_{2x,2x'-1} e^{-ip(x-x')}, \tag{E.3}$$

$$\Sigma^s_z = \sum_{x',x=1}^{L/2} C^{s,s}_{2x'-1,2x'-1} - C^{s,s}_{2x,2x}. \tag{E.4}$$

Each vector $\langle \Sigma^\uparrow(p) \rangle$, $\langle \Sigma^\downarrow(p) \rangle$ gives a winding number $|w| = 1$ in the topological phase ($\delta t > 0$) in the free limit $U = 0$ and still does so when we turn on the interactions $U > 0$. In Fig. 6.2 we show how the winding number is robust under interactions in the topological regime ($\delta t > 0$).

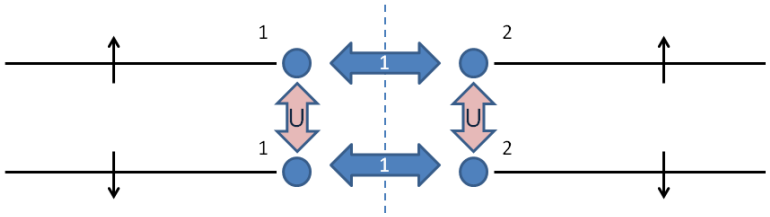

Figure E.1: Toy model for the virtual edges on either side of an entanglement cut (dashed blue line). Each spin component is shown as a separate chain. The virtual edge modes are shown as blue dots and would become physical ones if the cut was physical. The cross-cut hopping isset to 1 and we also add a repulsive interaction U between $\uparrow, \downarrow$ on each $1, 2$ site.

E.2 Toy Model for SSHH's Virtual Edge

The toy model Hamiltonian for the SSHH's edge is illustrated in Fig. E.1 and given by

$$H = -a^\dagger_{\uparrow 1} a_{\uparrow 2} - a^\dagger_{\downarrow 1} a_{\downarrow 2} + \text{h.c.} + U(n_{\uparrow 1} n_{\downarrow 1} + n_{\uparrow 2} n_{\downarrow 2}). \tag{E.5}$$

The Fock basis at half filling with $S_z = 0$ is $\{|1010\rangle, |0101\rangle, |0110\rangle, |0101\rangle\}$, where the first two bits refer to $\uparrow$ and the last two to $\downarrow$. The first and third bit refer to site 1 and the second and fourth to 2.

The ground state is

$$|gs\rangle = \frac{1}{\sqrt{N}}(|1010\rangle + |0101\rangle + \frac{1}{2}\left(U + \sqrt{4+U^2}\right)(|1001\rangle + |0110\rangle)), \tag{E.6}$$

where $N = 2 + \frac{1}{2}(U + \sqrt{4+U^2})^2$. From it we obtain the reduced density matrix, $\rho_1 = \text{tr}_2 |gs\rangle \langle gs|$ whose entropy is

$$\begin{aligned} S \;=\; & \frac{1}{U^2 + \sqrt{U^2+4}U + 4}(2\log\left(\frac{1}{U^2 + \sqrt{U^2+4}U + 4}\right) \\ & + \left(U^2 + \sqrt{U^2+4}U + 2\right)\log\left(\frac{\left(\sqrt{U^2+4}+U\right)^2}{4\left(U^2 + \sqrt{U^2+4}U + 4\right)}\right)). \end{aligned} \tag{E.7}$$

The 2-point correlation matrix is $C = \langle gs| a^\dagger_{\sigma i} a_{\sigma' j} |gs\rangle$, $i, j = 1, 2$ and is 4×4 in size. When non-interacting, C contains all the information of the system and it has eigenvalues μ with $\mu_j = 1$ for as many particles occupying the lattice and

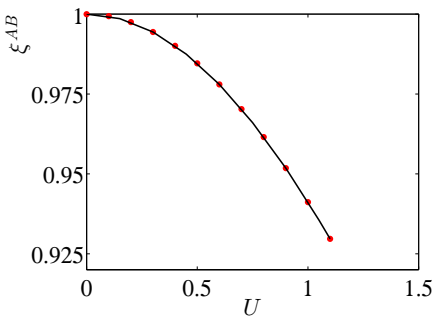

Figure E.2: Signatures ξ^{AB} of highly entangled pairs as a function of the interaction U. In red dots are numerical results from SSHH at the fixed point, $\delta t = 1$, for $L = 6$. Black line is the toy model's result.

the rest are $\mu_k = 0$. When interactions are turned on then this stops being true, as information about the system is spread into all high-order correlations and the μ move away from 0 and 1. Note that the interaction does not induce 2-point correlations between $\uparrow, \downarrow$, so C always remains block-diagonal.

Its correlation block C_{AB} is 2×2 in size and looks like

$$C_{AB} = \text{diag}\left(\frac{U + \sqrt{U^2+4}}{\frac{1}{2}\left(U + \sqrt{U^2+4}\right)^2 + 2}, \frac{U + \sqrt{U^2+4}}{\frac{1}{2}\left(U + \sqrt{U^2+4}\right)^2 + 2} \right). \tag{E.8}$$

The two maximally entangled fermion pairs appear as eigenvalues $\xi^{AB} \approx 1$ of the matrix $4C_{AB}^T C_{AB}$. This matrix is 2×2 and its spectrum is

$$\kappa = \left\{ \frac{4}{U^2+4}, \frac{4}{U^2+4} \right\} \tag{E.9}$$

which we plot in FIG.16 as a function of U. We see that the two pairs lose their entanglement as the interaction becomes stronger.

This toy model captures the bahaviour of the virtual edge modes around an entanglement cut. For the spinful SSHH model we performed two entanglement cuts which can be regarded as independent due to a finite localisation length of the virtual edge states. This explains the four highly entangled fermion pairs, correspoinding to an $M = 8$ signature in terms of Majorana pairs, all losing their entanglement together. Finally, in Fig. E.2 we show how the expression $\xi^{AB} = \frac{4}{U^2+4}$ from the toy model captures the shift from maximal entanglement for the SSHH model. We argue that if the covariance matrix were expressed in the basis in which the operators that create the edge states are decoupled from the Hamiltonian, then the monogamy signature would not decrease.

E.3 Jordan Wigner on the Ising Chain

The non-local relations between fermionic operators and Pauli spin-$\frac{1}{2}$ operators are given by [149]

$$\begin{aligned} Z_j &= 1 - 2n_j \ , \quad n_j = f_j^\dagger f_j \\ X_j &= -\prod_{l<j} Z_l (f_j + f_j^\dagger) \\ Y_j &= i \prod_{l<j} Z_l (f_j - f_j^\dagger). \end{aligned} \tag{E.10}$$

Substituting the expressions for X and Z in the quantum Ising's Hamiltonian given by 6.3 we obtain

$$H_\pm = \sum_{j=1}^{L} \mp f_j^\dagger f_{j+1} + f_j f_{j+1} + h_z n_j - h_x \prod_{l<j} (1 - 2n_l) f_j + \text{h.c.},$$

where $n_j = f_j^\dagger f_j$ the on-site fermionic population. When $h_x = 0$ this model is Kitaev's wire, given by 4.17, for $t = \pm 2$, $\Delta = 2$, $\phi = 0$, and $\mu = -2h_z$. The topological phase occurs for $|t| > |\mu|$ implying $h_z < 1$. Note that the sign determining ferromagnetism or anti-ferromagnetism does not change the physics due to particle-hole symmetry which allows $f_j^\dagger \leftrightarrow f_j$. The h_x-term makes the model non-quadratic for finite h_x with the introduction of an annihilation which non-locally depends on the parity of the chain-segment before it before it.

E.4 Convergence of Ising's Single-body Entanglement Levels

Here we present details on the rate of convergence to the optimal set of single body energies, ϵ, for the quantum Ising chain as a function of its length, L. We find that they converge exponentially, as shown in Fig. E.3. This is the case even near criticality due to the finite size induced gap. In the thermodynamic limit, however, the entanglement spectrum is gapless at criticality [44]. Hence the convergence to the optimal model is expected to be polynomial in L. We observe that a power law convergence can be well fitted around criticality, with the goodness of the fit decreasing away from it.

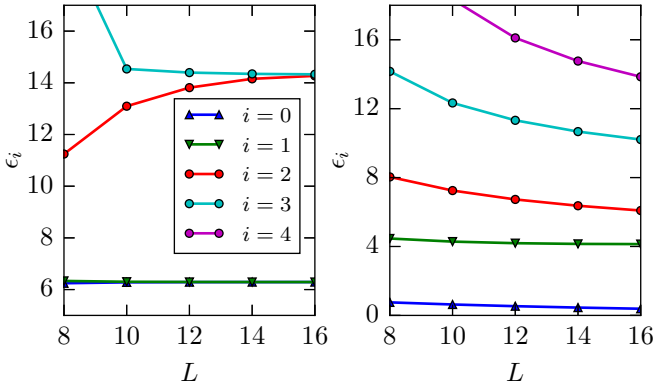

Figure E.3: Exponential convergence of lowest lying single-body entanglement energies ϵs with system size L for FM (Left) and AFM (Right) at a non-critical generic point ($h_z = 0.88, h_x = 0.16$).

E.5 Parachains: Higher N and Off the Fixed Point

In Fig. E.4 (Left) we present supplementary data for the support that the analytic form of $D_{\mathcal{F}}$ for flat spectra is indeed given by 6.6. In Fig. E.4 (Right) we present results obtained by Farjami and Turner. We see that $D_{\mathcal{F}}$ for $N = 3$ and $N = 4$ off the fixed point. We see that $\mathbb{Z}_4$ has $D_{\mathcal{F}} = 0$ for any $f > 0$, while the $D_{\mathcal{F}}$ value for $\mathbb{Z}_3$ persists throughout the topological phase.

The entanglement spectra used for computing $D_{\mathcal{F}}$ are obtained by exact diagonalisation of the parafermion Hamiltonian (6.4) in the clock basis. We transform the parafermions to the quantum clocks via the parafermionic version of the Jordan-Wigner transformation [150]

$$\gamma_l^{\mathrm{b}} = \left(\prod_{k<l} \tau_k\right) \sigma_l \quad , \qquad \gamma_l^{\mathrm{w}} = -\omega^{\frac{1}{2}} \left(\prod_{k\leq l} \tau_k \sigma_l\right) . \tag{E.11}$$

The $N \times N$ clock matrices have elements $\tau_{2,1} = \tau_{3,2} = \ldots = \tau_{N,N-1} = 1 = \tau 1, N$ and $\sigma = \mathrm{diag}(1, \omega, \ldots, \omega^{N-2}, \omega^{N-1})$. We then treat it like a usual spin Hamiltonian which conserves the parafermionic parity, $Q = \prod_l \tau_l$, the operator that winds each clock on the chain a phase ω. Obtaining the ground state in a

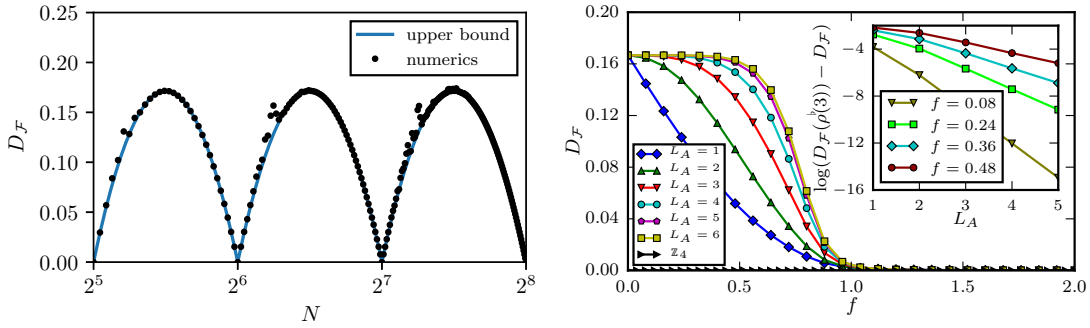

Figure E.4: (Left) Interaction distance, $D_\mathcal{F}$, for $E_\mathrm{e}^\flat(N)$. Numerical results (black dots) agree with the conjectured form of $D_\mathcal{F}$ given by 6.6 (blue line). The dots floating above the line are attributed to failure of the numerical optimisation to find the global minimum. We confirm this by increasing the number of basins the algorithm visits and observe that they land on the line. (Right) Interaction distance for the $\mathbb{Z}_4$ parafermion chains of length $L = 8$ and $\mathbb{Z}_3$ of length $L = 12$, with various partition sizes, L_A, as we move away from the fixed point, $f = 0$. While $D_\mathcal{F} = 0$ for $\mathbb{Z}_4$ for all values of f, it becomes a step function for $\mathbb{Z}_3$ as the partition size increases. (Inset) $\log(D_\mathcal{F}(\rho^\flat(3)) - D_\mathcal{F})$ for the $\mathbb{Z}_3$ chain shows that $D_\mathcal{F}$ converges exponentially to its fixed point value $D_\mathcal{F}(\rho^\flat(3))$ as we increase L_A.

Q-sector we can obtain the entanglement spectrum by reshaping the ground state in order to create the entanglement matrix and take its singular values.

Interestingly, there exists a parafermionic Fock space [151]. There exist analogues of creation and annihilation operators which are non-linear in terms of the parafermions for $N > 2$ with the difference that the vacuum is not annihilated but instead it transitions to the highest state as a clock should behave. The graded tensor product structure of fermions that takes care of the minus signs arising from fermionic exchange now turns into an ω-graded tensor product which introduces phases ω upon exchanging para-creation and para-annihilation operators. Then one can construct the Hamiltonian in the paraFock vectors compatible with a particular Q-sector and compute desired quantities as is done in ref [134], and in our case that would be the entanglement matrix.

E.6 Entanglement Spectrum for String-nets

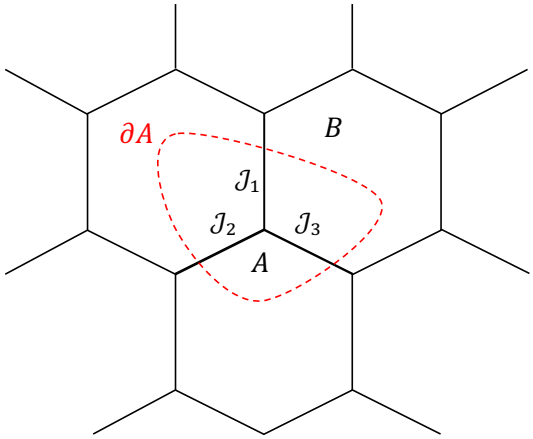

$\mathbb{Z}_3$	p	$SU(2)_2$	p
000	$\frac{1}{9}$	111	$\frac{1}{16}$
111	$\frac{1}{9}$	$1\sigma\sigma$	$\frac{2}{16}$
222	$\frac{1}{9}$	$\sigma 1\sigma$	$\frac{2}{16}$
012	$\frac{1}{9}$	$\sigma\sigma 1$	$\frac{2}{16}$
021	$\frac{1}{9}$	$1\psi\psi$	$\frac{1}{16}$
102	$\frac{1}{9}$	$\psi 1\psi$	$\frac{1}{16}$
120	$\frac{1}{9}$	$\psi\psi 1$	$\frac{1}{16}$
201	$\frac{1}{9}$	$\sigma\sigma\psi$	$\frac{2}{16}$
210	$\frac{1}{9}$	$\sigma\psi\sigma$	$\frac{2}{16}$
		$\psi\sigma\sigma$	$\frac{2}{16}$

Figure E.5: (Left) Entanglement cut around a vertex cutting three links on a string-net. Charges $\mathcal{J}_i$ occupy the $i = 1, 2, 3$ links. (Right) Charge configurations on ∂A for $\mathbb{Z}_3$ and $SU(2)$ together with their correspoinding propability.

Here we provide two simple examples, one for an Abelian and one for a non-Abelian group, of calculating the entanglement spectrum on a string-net using (6.9). The topologically trivial region we are cutting contains only one vertex of the honeycomb and thus the boundary ∂A cuts three links, $|\partial A| = 3$, as shown in Fig. E.5 (Left).

Take for the Abelian case the group $\mathbb{Z}_3$ with charges $\mathcal{J} = 0, 1, 2$. The calculation of the entanglement spectrum entails the enumeration of charge configurations on ∂A that fuse to the vacuum, which here we choose to be the element 0. These configurations of charges are determined then by the condition $\left(\sum_{i=1}^{3} \mathcal{J}_i\right) \text{mod} 3 = 0$. For the non-Abelian case we take the group $SU(2)_2$ which gives rise to Ising anyons. Each charge can take values $\mathcal{J} = 1, \sigma, \psi$, where 1 denotes the vacuum. The Ising fusion rules are $\sigma \times \sigma = 1 + \psi$, $\sigma \times \psi = \sigma$, and $\psi \times \psi = 1$. The allowed configurations on ∂A are those which have a finite probability to fuse to the vacuum. In Fig. E.5 (Right) we show the charge configurations which can fuse to the vacuum for both cases.

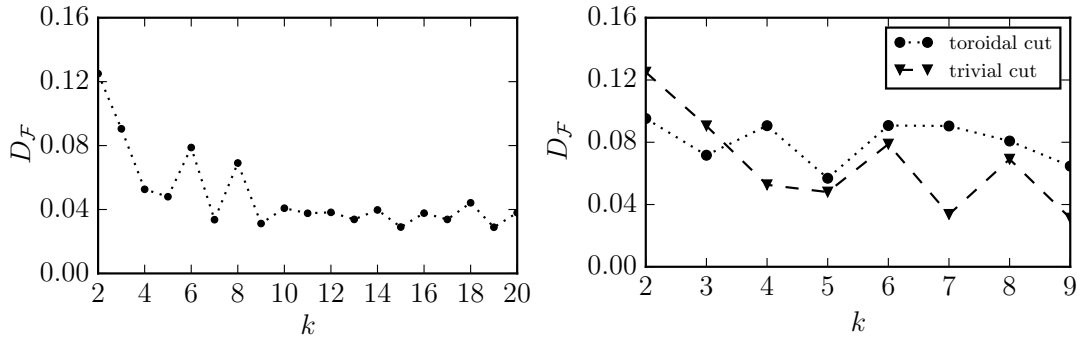

Figure E.6: (Left) Interaction distance $D_{\mathcal{F}}$ vs k for string-net endowed with group $SU(2)_k$ for a trivial entanglement cut deformable to a disk. (Right) When the entanglement cut has non-trivial topology, braiding properties affect the entanglement spectrum and $D_{\mathcal{F}}$ behaves differently quantitatively but not qualitatively.

E.7 Interaction Distance for Non-Abelian String-nets

Here we show numerical results for 2D and 3D string-nets endowed with the non-Abelian group $\mathrm{SU}(2)_k$ with total quantum dimension $\mathcal{D} = (\sqrt{\frac{2}{k+2}} \sin \frac{\pi}{k+2})^{-1}$ [52]. In Fig. E.6 (Left) we see that $D_{\mathcal{F}}$ for a 2D string net were we cut around a vertex as in Fig. E.5(Left) is finite for all $k \geq 2$ that we examined. Furthermore, we observe that $D_{\mathcal{F}}$ converges to $\approx \frac{D_{\mathcal{F}}^{\max}}{5}$ which is the most common value as seen from our numerical experiments with random states. Considering that for large k the multiplicities of the fusion channels of the anyons diverge and the vertices of the string-net represent random processes, we conjecture that the entanglement spectrum, and thus the interaction distance, resemble that of a random state. In the 3D case we compare $D_{\mathcal{F}}$ from a spherical cut and from a toroidal cut. In Fig. E.5(Right) we observe that indeed the braiding affects the entanglement spectrum and thus the interaction distance.

Bibliography

[1] A. Kitaev, Toward topological classification of phases with short-range entanglement, 2011. 4

[2] J. K. Pachos, *Introduction to Topological Quantum Computation* (Cambridge University Press, 2012). 7, 14, 39, 94

[3] B. Bernevig and T. Hughes, *Topological Insulators and Topological Superconductors* . 7, 9

[4] T. Fukui, Y. Hatsugai, and H. Suzuki, Journal of the Physical Society of Japan **74**, 1674 (2005), http://dx.doi.org/10.1143/JPSJ.74.1674. 8

[5] M. Atala *et al.*, Nat Phys **9**, 795 (2013). 9

[6] M. Aidelsburger *et al.*, Nat Phys **11**, 162 (2015), Letter. 9

[7] L. Fidkowski, Phys. Rev. Lett. **104**, 130502 (2010). 10, 11, 20, 34, 44, 45, 47

[8] I. Peschel, J. Phys. A **36**, L205 (2003). 10, 27

[9] S. Bravyi, Lagrangian representation for fermionic linear optics, 2005. 10

[10] J. Eisert, M. Cramer, and M. B. Plenio, Rev. Mod. Phys. **82**, 277 (2010). 10, 17, 55

[11] C. Weedbrook *et al.*, Rev. Mod. Phys. **84**, 621 (2012). 10

[12] V. Eisler and Z. Zimbors, New Journal of Physics **17**, 053048 (2015). 10

[13] A. Kitaev, Annals of Physics **321**, 2 (2006), January Special Issue. 11, 16, 36, 40, 41, 59, 93, 120

[14] J. Bellissard, A. van Elst, and H. S. Baldes, Journal of Mathematical Physics **53**, 5373 (1994). 11

[15] E. Prodan, T. L. Hughes, and B. A. Bernevig, Phys. Rev. Lett. **105**, 115501 (2010). 11, 121

[16] E. Prodan, Journal of Physics A: Mathematical and Theoretical **44**, 113001 (2011). 11, 121

[17] E. Prodan, A computational non-commutative geometry program for disordered topological insulators, 2016, arXiv:1611.09737. 11

[18] M. B. Hastings and T. Koma, Communications in Mathematical Physics **265**, 781 (2006). 11

[19] D. Gosset and Y. Huang, Phys. Rev. Lett. **116**, 097202 (2016). 11

[20] V. Lahtinen, A. W. W. Ludwig, J. K. Pachos, and S. Trebst, Phys. Rev. B **86**, 075115 (2012). 11, 38, 39, 40, 41, 53

[21] G. Palumbo and K. Meichanetzidis, Phys. Rev. B **92**, 235106 (2015). 11, 71

[22] T. L. Hughes, E. Prodan, and B. A. Bernevig, Phys. Rev. B **83**, 245132 (2011). 12

[23] M. T. Fishman and S. R. White, Phys. Rev. B **92**, 075132 (2015). 12

[24] J. E. Wilkins, Ann. Math. Statist. **15**, 333 (1944). 12

[25] I. Peschel and M.-C. Chung, EPL (Europhysics Letters) **96**, 50006 (2011). 13, 26, 97

[26] J. I. Latorre, E. Rico, and G. Vidal, Quantum Info. Comput. **4**, 48 (2004). 13

[27] I. Klich, (2004), arXiv:quant-ph/0406068. 13, 44, 47, 102

[28] X.-G. Wen, *Quantum Field Theory of Many-Body Systems* (Oxford Graduate Texts, 2007). 14, 93

[29] A. Kitaev, Annals of Physics **303**, 2 (2003). 14, 40, 93

[30] M. H. Freedman, A. Kitaev, M. J. Larsen, and Z. Wang, Topological quantum computation, 2001, arXiv:quant-ph/0101025. 14

[31] A. Roy and D. P. DiVincenzo, Topological quantum computing, 2017, arXiv:1701.05052. 14

[32] Z.-C. Gu, Z. Wang, and X.-G. Wen, Phys. Rev. B **90**, 085140 (2014). 14

[33] C. Nayak, S. H. Simon, A. Stern, M. Freedman, and S. Das Sarma, Rev. Mod. Phys. **80**, 1083 (2008). 14

[34] N. E. Bonesteel, L. Hormozi, G. Zikos, and S. H. Simon, Phys. Rev. Lett. **95**, 140503 (2005). 15

[35] E. Witten, Comm. Math. Phys. **121**, 351 (1989). 15

[36] S. Matsuura, P.-Y. Chang, A. P. Schnyder, and S. Ryu, New Journal of Physics **15**, 065001 (2013). 15, 72

[37] X. Chen, Z.-C. Gu, Z.-X. Liu, and X.-G. Wen, Phys. Rev. B **87**, 155114 (2013). 16, 90

[38] X. G. Wen and Q. Niu, Phys. Rev. B **41**, 9377 (1990). 16

[39] M. B. Hastings and X.-G. Wen, Phys. Rev. B **72**, 045141 (2005). 16

[40] S. Bravyi, M. B. Hastings, and S. Michalakis, Journal of Mathematical Physics **51**, 093512 (2010), http://dx.doi.org/10.1063/1.3490195. 16

[41] X. Chen, Z.-C. Gu, and X.-G. Wen, Phys. Rev. B **82**, 155138 (2010). 16, 93

[42] A. Stern, Annals of Physics **323**, 204 (2008), January Special Issue 2008. 16, 25

[43] H. Li and F. D. M. Haldane, Phys. Rev. Lett. **101**, 010504 (2008). 16, 17, 104

[44] P. Calabrese and A. Lefevre, Phys. Rev. A **78**, 032329 (2008). 17, 130

[45] X.-L. Qi, H. Katsura, and A. W. W. Ludwig, Phys. Rev. Lett. **108**, 196402 (2012). 17

[46] X.-L. Qi, Y.-S. Wu, and S.-C. Zhang, Phys. Rev. B **74**, 045125 (2006). 17

[47] F. G. S. L. Brandão and M. Horodecki, Communications in Mathematical Physics **333**, 761 (2015). 17

[48] A. Chandran, C. Laumann, and R. Sorkin, Entropy (2016). 17

[49] L. Masanes, Phys. Rev. A **80**, 052104 (2009). 17

[50] M. Srednicki, Phys. Rev. Lett. **71**, 666 (1993). 17

[51] J. C. Budich, J. Eisert, and E. J. Bergholtz, (2013), arXiv:1311.3309. 17, 38, 47

[52] A. Kitaev and J. Preskill, Phys. Rev. Lett. **96**, 110404 (2006). 18, 39, 134

[53] M. Levin and X.-G. Wen, Phys. Rev. Lett. **96**, 110405 (2006). 18

[54] V. Coffman, J. Kundu, and W. K. Wootters, Phys. Rev. A **61**, 052306 (2000). 20, 22, 23, 100

[55] T. J. Osborne and F. Verstraete, Phys. Rev. Lett. **96**, 220503 (2006). 20, 22, 23, 101

[56] P. Fendley, Journal of Physics A: Mathematical and Theoretical **49**, 30LT01 (2016). 21, 49

[57] W. K. Wootters, Phys. Rev. Lett. **80**, 2245 (1998). 22, 23

[58] C. H. Bennett, H. J. Bernstein, S. Popescu, and B. Schumacher, Phys. Rev. A **53**, 2046 (1996). 22

[59] A. P. Schnyder, S. Ryu, A. Furusaki, and A. W. W. Ludwig, Phys. Rev. B **78**, 195125 (2008). 24

[60] A. Kitaev, AIP Conference Proceedings **1134**, 22 (2009), http://aip.scitation.org/doi/pdf/10.1063/1.3149495. 24

[61] R. Thomale, A. Sterdyniak, N. Regnault, and B. A. Bernevig, Phys. Rev. Lett. **104**, 180502 (2010). 24

[62] J. Alicea and P. Fendley, Annual Review of Condensed Matter Physics **7**, 119 (2016), 10.1146/annurev-conmatphys-031115-011336. 25, 62, 85

[63] Y.-C. Ou, Phys. Rev. A **75**, 034305 (2007). 25

[64] Q. Li, J. Cui, S. Wang, and G.-L. Long, Scientific Reports **7**, 1946 (2017). 25

[65] M. S. Rudner, N. H. Lindner, E. Berg, and M. Levin, Phys. Rev. X **3**, 031005 (2013). 25

[66] M. Nowakowski, Monogamy of quantum entanglement in time, 2016, arXiv:1604.03976. 25

[67] B. Sutherland, *Beautiful Models: 70 Years of Exactly Solved Quantum Many-body Problems* (World Scientific, 2004). 26

[68] R. P. Feynman, Phys. Rev. **94**, 262 (1954). 26

[69] J. Bardeen, L. N. Cooper, and J. R. Schrieffer, Phys. Rev. **108**, 1175 (1957). 26

[70] M. C. Gutzwiller, Phys. Rev. Lett. **10**, 159 (1963). 26

[71] R. B. Laughlin, Phys. Rev. Lett. **50**, 1395 (1983). 26

[72] R. Ors, Annals of Physics **349**, 117 (2014). 26, 34

[73] F. Verstraete, V. Murg, and J. I. Cirac, Advances in Physics **57**, 143 (2008). 26, 34

[74] G. Vidal, Phys. Rev. Lett. **101**, 110501 (2008). 26, 34

[75] J. Carrasquilla and R. G. Melko, Nat Phys **13**, 431 (2017). 26

[76] X. Gao and L.-M. Duan, Efficient representation of quantum many-body states with deep neural networks, 2017, arXiv:1701.05039. 26

[77] E. P. L. van Nieuwenburg, Y.-H. Liu, and S. D. Huber, Learning phase transitions by confusion, 2016, arXiv:1610.02048. 26

[78] C. A. Fuchs and J. van de Graaf, IEEE Trans. Inf. Theory **45**, 1216 (1999). 29

[79] D. Markham, J. A. Miszczak, Z. Puchała, and K. Życzkowski, Phys. Rev. A **77**, 042111 (2008). 29, 32

[80] M. A. Nielsen and I. L. Chuang, *Quantum Computation and Quantum Information: 10th Anniversary Edition*, 10th ed. (Cambridge University Press, New York, NY, USA, 2011). 31

[81] C. Weedbrook *et al.*, Rev. Mod. Phys. **84**, 621 (2012). 32

[82] M. G. Genoni, M. G. A. Paris, and K. Banaszek, Phys. Rev. A **78**, 060303 (2008). 32

[83] P. Marian and T. A. Marian, Phys. Rev. A **88**, 012322 (2013). 32

[84] J. Gertis, M. Friesdorf, C. A. Riofrío, and J. Eisert, Phys. Rev. A **94**, 053628 (2016). 32

[85] K. Byczuk, J. Kuneš, W. Hofstetter, and D. Vollhardt, Phys. Rev. Lett. **108**, 087004 (2012). 32

[86] A. D. Gottlieb and N. J. Mauser, ArXiv e-prints (2015), 1510.04573. 32

[87] J. M. Zhang and M. Kollar, Phys. Rev. A **89**, 012504 (2014). 32

[88] S. Zhang, *Quantum Monte Carlo Methods for Strongly Correlated Electron Systems* (Springer New York, New York, NY, 2004). 34

[89] A. S. Holevo and R. F. Werner, Phys. Rev. A **63**, 032312 (2001). 34

[90] C. Schilling, D. Gross, and M. Christandl, Phys. Rev. Lett. **110**, 040404 (2013). 35

[91] V. Lahtinen and J. K. Pachos, New Journal of Physics **11**, 093027 (2009). 36, 41, 65

[92] G. Kells, J. K. Slingerland, and J. Vala, Phys. Rev. B **80**, 125415 (2009). 36

[93] H.-D. Chen and Z. Nussinov, Journal of Physics A: Mathematical and Theoretical **41**, 075001 (2008). 36

[94] F. L. Pedrocchi, S. Chesi, and D. Loss, Phys. Rev. B **84**, 165414 (2011). 36

[95] J. Knolle, D. L. Kovrizhin, J. T. Chalker, and R. Moessner, Phys. Rev. Lett. **112**, 207203 (2014). 36

[96] E. H. Lieb, Phys. Rev. Lett. **73**, 2158 (1994). 37

[97] J. K. Pachos, Annals of Physics **322**, 1254 (2007). 38, 40

[98] V. Lahtinen, A. W. W. Ludwig, and S. Trebst, Phys. Rev. B **89**, 085121 (2014). 38, 39, 40

[99] V. Lahtinen and J. K. Pachos, Phys. Rev. B **81**, 245132 (2010). 38, 40, 41, 57

[100] H. Yao and X.-L. Qi, Phys. Rev. Lett. **105**, 080501 (2010). 38, 39, 63, 64

[101] V. Lahtinen, New Journal of Physics **13**, 075009 (2011). 39, 40

[102] V. Lahtinen *et al.*, Annals of Physics **323**, 2286 (2008). 39, 40

[103] S. S. Pershoguba and V. M. Yakovenko, Phys. Rev. B **86**, 075304 (2012). 44, 45, 116, 117

[104] D. Sticlet, F. Piéchon, J.-N. Fuchs, P. Kalugin, and P. Simon, Phys. Rev. B **85**, 165456 (2012). 44, 116

[105] R. S. K. Mong and V. Shivamoggi, Phys. Rev. B **83**, 125109 (2011). 44, 116

[106] K. Meichanetzidis, M. Cirio, J. K. Pachos, and V. Lahtinen, Phys. Rev. B **94**, 115158 (2016). 45, 58, 116, 118

[107] C. R. Laumann, A. W. W. Ludwig, D. A. Huse, and S. Trebst, Phys. Rev. B **85**, 161301 (2012). 53

[108] V. Lahtinen, New Journal of Physics **13**, 075009 (2011). 53

[109] C. N. Self, J. K. Pachos, J. R. Wootton, and S. Iblisdir, Conformal energy currents on the edge of a topological superconductor, 2016, arXiv:1607.06100. 53, 120

[110] P. Francesco, *Conformal Field Theory* (Springer, 1997). 55, 58

[111] P. Calabrese and J. Cardy, Journal of Statistical Mechanics: Theory and Experiment **2004**, P06002 (2004). 55

[112] A. M. Turner, Y. Zhang, and A. Vishwanath, Phys. Rev. B **82**, 241102 (2010). 57

[113] E. Ardonne, P. Fendley, and E. Fradkin, Annals of Physics **310**, 493 (2004). 58

[114] T. Månsson, V. Lahtinen, J. Suorsa, and E. Ardonne, Phys. Rev. B **88**, 041403 (2013). 58

[115] V. Lahtinen, T. Månsson, and E. Ardonne, Phys. Rev. B **89**, 014409 (2014). 58

[116] A. Y. Kitaev, Physics-Uspekhi **44**, 131 (2001). 58, 85

[117] F. L. Pedrocchi, S. Chesi, and D. Loss, Phys. Rev. B **84**, 165414 (2011). 64

[118] A. Chandran, V. Khemani, and S. L. Sondhi, Phys. Rev. Lett. **113**, 060501 (2014). 65

[119] F. D. M. Haldane, Phys. Rev. Lett. **61**, 2015 (1988). 66

[120] J. Lado, N. Garca-Martnez, and J. Fernndez-Rossier, Synthetic Metals **210**, 56 (2015), Reviews of Current Advances in Graphene Science and Technology. 66

[121] W. P. Su, J. R. Schrieffer, and A. J. Heeger, Phys. Rev. Lett. **42**, 1698 (1979). 68, 75

[122] R. A. Krajcik and M. M. Nieto, Phys. Rev. D **10**, 4049 (1974). 71

[123] D. Wang, S. Xu, Y. Wang, and C. Wu, Phys. Rev. B **91**, 115118 (2015). 76, 78, 119

[124] B.-T. Ye, L.-Z. Mu, and H. Fan, Phys. Rev. B **94**, 165167 (2016). 77

[125] J. de Lisle *et al.*, New Journal of Physics **16**, 083022 (2014). 78, 127

[126] E. Alba, J. K. Pachos, and J. J. Garca-Ripoll, New Journal of Physics **18**, 033022 (2016). 78, 127

[127] A. Dutta *et al.*, *Quantum Phase Transitions in Transverse Field Models* (Cambridge University Press, 2015). 80, 82

[128] C. J. Turner, K. Meichanetzidis, Z. Papic, and J. K. Pachos, Nat. Commun. **8**, 14926 (2017). 81, 89

[129] S. R. White, Phys. Rev. Lett. **69**, 2863 (1992). 81

[130] T. D. Schultz, D. C. Mattis, and E. H. Liev, Rev. Mod. Phys. **36**, 856 (1964). 85

[131] E. Fradkin and L. P. Kadanoff, Nuclear Physics B **170**, 1 (1980). 85

[132] J. Motruk, E. Berg, A. M. Turner, and F. Pollmann, Phys. Rev. B **88**, 085115 (2013). 85

[133] W. Li, S. Yang, H.-H. Tu, and M. Cheng, Phys. Rev. B **91**, 115133 (2015). 85

[134] N. Moran, D. Pellegrino, J. K. Slingerland, and G. Kells, Phys. Rev. B **95**, 235127 (2017). 85, 132

[135] P. Fendley, Journal of Statistical Mechanics: Theory and Experiment **2012**, P11020 (2012). 86, 90

[136] K. Meichanetzidis, C. J. Turner, A. Farjami, Z. Papi, and J. K. Pachos, Free-fermion descriptions of parafermion chains and string-net models, 2017, arXiv:1705.09983. 89, 90, 94

[137] M. A. Levin and X.-G. Wen, Phys. Rev. B **71**, 045110 (2005). 91

[138] C.-H. Lin and M. Levin, Phys. Rev. B **89**, 195130 (2014). 91

[139] A. Bullivant and J. K. Pachos, Phys. Rev. B **93**, 125111 (2016). 91, 92

[140] S. Trebst, M. Troyer, Z. Wang, and A. W. W. Ludwig, Progress of Theoretical Physics Supplement **176**, 384 (2008). 94

[141] K. Walker and Z. Wang, Frontiers of Physics **7**, 150 (2012). 95

[142] S. C. Davenport, I. D. Rodríguez, J. K. Slingerland, and S. H. Simon, Phys. Rev. B **92**, 115155 (2015). 96

[143] J. Eisert, V. Eisler, and Z. Zimbors, Entanglement negativity bounds for fermionic gaussian states, 2016, arXiv:1611.08007. 100

[144] D. J. Wales and J. P. K. Doye, J. Phys. Chem. A **101**, 5111 (1997). 102

[145] C. Park, Phys. Rev. D **92**, 126013 (2015). 103

[146] D. Shaffer, C. Chamon, A. Hamma, and E. R. Mucciolo, Journal of Statistical Mechanics: Theory and Experiment **2014**, P12007 (2014). 104, 106

[147] Z.-C. Yang, A. Hamma, S. M. Giampaolo, E. R. Mucciolo, and C. Chamon, Entanglement complexity in quantum many-body dynamics, thermalization and localization, 2017, arXiv:1703.03420. 108

[148] P. W. Anderson, Phys. Rev. **109**, 1492 (1958). 123

[149] M. A. Nielsen, The fermionic canonical commutation relations and the jordan-wigner transform, 2005. 130

[150] W.-T. Xu and G.-M. Zhang, Phys. Rev. B **95**, 195122 (2017). 131

[151] E. Cobanera and G. Ortiz, Phys. Rev. A **89**, 012328 (2014). 132